Terahertz Spectroscopy of Charge-Carrier Transport in Metal-Halide Perovskites and Narrow-Gap Semiconductors



Chelsea Qiushi Xia

St Edmund Hall

University of Oxford

A thesis submitted for the degree of

Doctor of Philosophy

Trinity 2020

Acknowledgements

This thesis is made possible thanks to the help of a great number of people. Firstly, I would like to thank my supervisor Prof. Michael Johnston for his continuous support, both academically and emotionally, which has helped me to get through the entire four years of my postgraduate journey and guided me into the field of terahertz spectroscopy where I have found my passion in research. Your enthusiasm and dedication in science have always inspired me and reflected what a real scientist is like. I would also like to thank Prof. Laura Herz whom I admire as a role model for being a woman in physics. Thank you so much for your help, advice and the discussions we had about my projects. Thanks to both of you, our research group has been made a super friendly and welcoming place for scientific collaborations as well as social engagement. Being part of the group has definitely been one of the highlights of my life in Oxford.

I would like to thank all of my colleagues for the help, ideas, discussions and company through out my entire DPhil: Rebecca Milot, Jessica Boland, Adam Wright, Chris Davies, Jay Patel, Timothy Crothers, Juliane Borchert, Juliane Gong, Kun Peng, Sabrina Sterzl, Djamshid Damry, Hannah Eggimann, Kimberley Savill, Alex Knight, Leonardo Buizza, Kilian Lohmann, Aleksander Ulatowski, Mathias Rothmann, Silvia Motti, Lavina Snoek, James Ball, Laura Martínez-Maestro, Robert Oliver, Elisabeth Duijnstee, Michael Trimpl, Qianqian Lin, Elizabeth Parrott and Waqaas Rehman. In particular, I thank Rebecca Milot and Jessica Boland for their mentoring when I first joined the group, from which I learned a great deal of knowledge in terahertz spectroscopy and was able to make progress in my research smoothly. I thank Adam Wright and Chris Davies for being my labmates during those periods of doing helium/magnet experiments, which was very time-consuming and I am very grateful for their help with the experiments and staying late with me in the lab. I thank everyone for being supportive and keen on organizing social events, which brought so much fun to my life outside the lab. All of those tea breaks, pub lunches, punting, croqueting and house parties have helped me to maintain a good work-life balance and made my Oxford experience ever more special.

I also thank my collaborators for their hard work and support, without which it would not have been possible to achieve what has been put into this thesis. I thank Qianqian Lin, who is also an alumnus of our group, for providing me with the delicate single crystal samples multiple times.

I thank Dr. Samuel Poncé and Prof. Marina Filip for all of their efforts in conducting the theoretical work. I thank Dr. James Lloyd-Hughes for his mentoring in my InSb project.

Last but not least, I would like to thank my family and friends for their unfailing support and encouragement, especially my parents for their love, care and financial support, so that I could focus on my DPhil study and enjoy my time here. I thank my friends both in Oxford and overseas who have kept me company so that I never felt lonely while being away from home. Special thanks to Juliane Gong, Jian Huang, Kilian Lohmann, Jacqueline Tan, Chenzi Xu, Abe Ng, Andi Wang and my flatmates Lauren Bandy, Jess Renzella, Tatjana Schulze, Rob Smith and Mike Joseph, from whom I have learned a lot about life. The time we spent together would always be remembered.

Abstract

Organic-inorganic metal-halide perovskites and narrow-gap semiconductors have been studied extensively over the last few decades. Their peculiar optoelectronic properties make them ideal candidates for future photovoltaic applications and ultrafast electronic devices. Specifically, knowledge of the charge-carrier transport and electronic band structure is key to understanding the fundamental principles that underpin their optoelectronic behaviors, and hence to improve the performance of devices based on them.

Terahertz spectroscopy provides an ideal pathway to probe the optoelectronic properties of these semiconductor materials not only because of its non-contact nature which avoids damaging the sample and removes the complications arising from metallic contacts, but also due to its ability to measure the charge-carrier dynamics on an ultrafast (sub-picosecond) timescale. The versatility of terahertz spectroscopy allows a large phase space of optoelectronic parameters to be probed, such as charge-carrier mobility, carrier diffusion length, and photoconductivity.

A comparative study on the prototypical metal-halide perovskite $MAPbI_3$ as both single crystals and polycrystalline films suggests that Fröhlich scattering is the dominant mechanism limiting charge-carrier mobility, which arises from the electron-phonon coupling effect. Further investigations of the phonon modes in $MAPbI_3$ show a phonon-hardening effect under photo-excitation, which is attributed to the increase in dielectric screening due to photo-induced electron doping. In addition, grain-boundary scattering is shown to further reduce mobility in polycrystalline films at cryogenic temperature. By taking into account the effect of photon reabsorption, the wide range of values for charge recombination parameters and charge diffusion lengths reported previously is reconciled. The benign grain boundaries observed in polycrystalline films offer great promise for future high-performance devices.

Time-resolved magneto-terahertz spectroscopy is utilized to investigate the cyclotron effective mass of a narrow-gap semiconductor InSb. A significant reduction of effective mass observed in the first 50 ps after photoexcitation indicates a fast hot-electron cooling process. Meanwhile, the increase in effective mass with increasing carrier density agrees with the non-parabolic conduction band predicted by the *ab initio* calculations of the quasiparticle band structure based on the Kane model.

This thesis, which combines a thorough experimental study utilizing terahertz spectroscopy with a complementary theoretical study based on first-principles calculations, helps to uncover a complete picture of the fundamental optoelectronic properties of metal-halide perovskites and narrow-gap semiconductors.

List of Publications

- **Chelsea Q. Xia**, Jiali Peng, Samuel Poncé, Jay B. Patel, Aleksander M. Ulatowski, Adam D. Wright, Rebecca L. Milot, Hans Kraus, Qianqian Lin, Feliciano Giustino, Laura M. Herz, Michael B. Johnston, *Phonon hardening observed in $MAPbI_3$ single crystal and thin film perovskites* (in preparation, 2020)

- **Chelsea Q. Xia**, Maurizio Monti, Jessica L. Boland, Laura M. Herz, James Lloyd-Hughes, Marina R. Filip, Michael B. Johnston, *Time-resolved cyclotron resonance in InSb* (in preparation, 2020)

- **Chelsea Q. Xia**, Jiali Peng, Samuel Poncé, Jay B. Patel, Adam D. Wright, Timothy W. Crothers, Mathias Uller Rothmann, Juliane Borchert, Rebecca L. Milot, Hans Kraus, Qianqian Lin, Feliciano Giustino, Laura M. Herz, Michael B. Johnston, *Limits to electrical mobility in perovskite semiconductors*, Nature Communications (under review, 2020)

- Jiali Peng, **Chelsea Q. Xia**, Yalun Xu, Ruiming Li, Lihao Cui, Jack K. Clegg, Laura M. Herz, Michael B. Johnston, Qianqian Lin, *Crystallization of $CsPbBr_3$ single crystals in water for X-ray detection*, Nature Communications (under review, 2020)

- Robert D. J. Oliver, Yen-Hung Lin, Alexander J. Horn, **Chelsea Q. Xia**, Jonathan H. Warby, Michael B. Johnston, Alexandra J. Ramadan, Henry J. Snaith, *Thermally stable passivation toward high efficiency inverted perovskite solar cells*, ACS Energy Letters, **5**, 3336–3343 (2020)

- Kilian B. Lohmann, Jay B. Patel, Mathias Uller Rothmann, **Chelsea Q. Xia**, Robert D. J. Oliver, Laura M. Herz, Henry J. Snaith, Michael B. Johnston, *Control over crystal size in vapor deposited metal-halide perovskite films*, ACS Energy Letters, **5**, 710–717 (2020)

- Jay B. Patel, Adam D. Wright, Kilian B. Lohmann, Kun Peng, **Chelsea Q. Xia**, James M. Ball, Nakita K. Noel, Timothy W. Crothers, Jenny Wong-Leung, Henry J. Snaith, Laura M. Herz, Michael B. Johnston, *Light absorption and recycling in hybrid metal halide perovskite photovoltaic devices*, Advanced Energy Materials, **10**, 1903653 (2020)

- Christopher L. Davies, Juliane Borchert, **Chelsea Q. Xia**, Rebecca L. Milot, Hans Kraus, Michael B. Johnston, Laura M. Herz, *Impact of the organic cation on the optoelectronic properties of formamidinium lead triiodide*, Journal of Physical Chemistry Letters, **9**, 4502–4511 (2018)

- Christopher L. Davies, Jay B. Patel, **Chelsea Q. Xia**, Laura M. Herz, Michael B. Johnston, *Temperature-dependent refractive index of quartz at terahertz frequencies*, Journal of Infrared, Millimeter and Terahertz Waves, **39**, 1236–1248 (2018)

List of Abbreviations

BBO ····· β-barium borate

BTE ····· Boltzmann transport equation

CCD ····· Charge-coupled device

DFT ····· Density-functional theory

DFPT ····· Density-functional perturbation theory

DOS ····· Density of states

EOS ····· Electro-optic sampling

FTIR ····· Fourier-transform infrared (spectroscopy)

FWHM ····· Full width at half maximum

KK ····· Kramers-Kronig (transformation)

LO ····· Longitudinal-optical (phonon)

LST ····· Lyddane-Sachs-Teller (relation)

MA ····· Methylammonium

MHP ····· Metal-halide perovskite

OPTPS ····· Optical-pump-terahertz-probe spectroscopy

PCE ····· Power conversion efficiency

PL ····· Photoluminescence

PLQE ····· Photoluminescence quantum efficiency

SEM ····· Scanning electron microscopy

SNR ····· Signal-to-noise ratio

STE ····· Spintronic terahertz emitter

TA ····· Transverse-acoustic (phonon)

TFA ····· Thin-film approximation

THz ····· Terahertz (10^{12} Hz)

THz-TDS ····· Terahertz time-domain spectroscopy

TO ····· Transverse-optical (phonon)

TRPL ····· Time-resolved photoluminescence

VDF ····· Variational dielectric function

XRD ····· X-ray diffraction

Contents

1 Introduction **1**

1.1 Metal-Halide Perovskites . . . 3

1.1.1 Background . . . 3

1.1.2 Growth . . . 5

1.1.3 Applications and Challenges . . . 7

1.2 Narrow-Gap Semiconductors . . . 9

1.2.1 Background . . . 9

1.2.2 Defects Formed in Fabrication . . . 10

1.2.3 Applications . . . 11

1.3 Thesis Overview . . . 12

2 Fundamental Principles and Previous Work **14**

2.1 Charge-Carrier Transport in Perovskites . . . 14

2.1.1 Charge-Carrier Dynamics and Photon Reabsorption . . . 14

2.1.2 First-Principles Calculations of Electrical Mobilities . . . 17

2.1.3 Grain-Boundary Scattering in Polycrystalline Films . . . 20

2.1.4 Lattice Vibrations in Perovskites . . . 22

2.2 Electronic Band Structure and Charge-Carrier Relaxation of InSb . . . 24

2.2.1 Non-Parabolic Conduction Band . . . 24

2.2.2 Hot Carrier Relaxation Mechanism . . . 28

3 Experimental Techniques **31**

3.1 Terahertz Spectroscopy . . . 31

3.1.1 THz Time-Domain Spectroscopy (THz-TDS) and Optical-Pump-THz-Probe Spectroscopy (OPTPS) . . . 32

3.1.1.1 THz Generation . . . 36

3.1.1.2 Electro-Optic Sampling . . . 38

3.1.2 Polarization-Resolved Magneto-THz Spectroscopy . . . 42

3.1.3 Data Analysis of THz Spectroscopy 45
3.1.3.1 Charge-Carrier Mobility 45
3.1.3.2 Conductivity of $MAPbI_3$ Thin Films 57
3.1.3.3 Reflectivity of $MAPbI_3$ Single Crystals 59

4 Limits to Electrical Mobility in $MAPbI_3$ Single Crystals and Polycrystalline Thin Films 62
4.1 Introduction 62
4.2 Sample Fabrication 65
4.2.1 $MAPbI_3$ Single Crystal Growth 65
4.2.2 $MAPbI_3$ Thin Film Growth 66
4.3 Experimental and Computational Methods 67
4.3.1 Optical-Pump-THz-Probe Spectroscopy (OPTPS) 67
4.3.2 Thermometry and Temperature-Dependent PL Spectroscopy . 68
4.3.3 Computational Method 75
4.4 Results and Discussions 76
4.4.1 Electrical Mobility and Charge-Carrier Dynamics at Room Temperature 76
4.4.2 Temperature-Dependence of Electrical Mobility 82
4.4.3 Grain-Boundary Scattering in $MAPbI_3$ Thin Films 84
4.4.4 Significance of Photon Reabsorption and Its Effect on Charge-Carrier Dynamics and Diffusion Length 86
4.5 Summary 97

5 Phonon Hardening Observed in $MAPbI_3$ Single-Crystal and Thin-Film Perovskites 98
5.1 Introduction 98
5.2 Methods 100
5.3 Results and Discussions 101
5.3.1 Phonon Modes Observed at THz Frequencies 101
5.3.2 Phonon Hardening Arising from Photo-Excitation 105
5.3.3 Theoretical Investigations of Phonon Hardening 111
5.4 Summary 115

6 Time-Resolved Cyclotron Resonance in InSb 116
6.1 Introduction 116
6.2 Experimental and Computational Methods 120

6.2.1 Sample Fabrication and Specifications 120
6.2.2 Magneto-THz Spectroscopy 120
6.2.3 Computational Setup 121
6.3 Results and Discussions 123
6.3.1 Cyclotron Resonance in Photo-Excited InSb 123
6.3.2 Magnetic-Field Dependence of Electron Effective Mass 127
6.3.3 Hot Electron Cooling in InSb 129
6.3.4 Quasiparticle Band Structure Calculation 133
6.3.5 Non-Parabolic Conduction Band Probed by Quasi-Fermi Level 135
6.4 Summary 142

7 Conclusions and Outlook **143**

Bibliography **148**

Chapter 1

Introduction

The study of semiconductors whose electrical conductivity lies between that of metals and insulators can date back to the early 19th century, when Michael Faraday discovered that the electrical conductivity of silver sulphide increases with temperature [1], which is opposite to the temperature dependence of conductivity of metals. Now we understand that this is because the number of mobile charge carriers in semiconductors increases with temperature, which overcomes the reduction of electrical mobility arising from lattice vibration scattering; whereas in metals, the number of mobile charge carriers is essentially constant and the increase in temperature tends to reduce the electrical mobility of charge carriers. This novel feature of semiconductors has attracted intensive interest ever since then. In 1873, Willoughby Smith discovered photoconductivity in selenium, a change of conductivity under light [2], which showed that semiconductors are able to convert light to electricity without the need of heat and pioneered the photovoltaic applications of semiconductors. In 1883, Charles Fritts constructed the first photovoltaic cell using selenium [3], although the power conversion efficiency (PCE) of light to electricity was only less than 1% and not improved for many years. In addition, Fritts also observed rectification in semiconductors, which was systematically studied by Carl Ferdinand Braun [4]. This

discovery of rectification phenomenon underpinned the development of electronic devices in the 20th century. Thanks to the application of germanium in rectifier diodes, much deeper understanding of the physics of semiconductors was gained, giving rise to the invention of transistors [5].

Meanwhile, the development of quantum theory helped explain the behavior of semiconductors, leading to the development of the band theory of solids proposed by Alan Wilson in 1931 [6]. Ever since then, investigations of the band structure of semiconductors have played an important role in describing the fundamental electronic properties of semiconductors. With the development of material science and quantum theory, the field of semiconductors has expanded significantly and various novel band structure features have been observed. For instance, narrow-gap semiconductors such as InSb are found to have extremely high electrical mobility [7], which makes them preferable for making ultrafast electronic devices. On top of that, the non-parabolicity of the conduction band which gives rise to some anomalous behavior such as nonlinear response to external magnetic field [8–10], has attracted even more research interests regarding the relevant electromagnetic properties.

On the other hand, the photovoltaic application of semiconductors is also considered as a great alternative to the traditional energy resources such as fossil fuels, due to its sustainability and renewability. While in the past few decades, solar cells made by conventional semiconductors including silicon and GaAs have almost reached the saturation point of energy conversion efficiency, a newly emerging material, metal-halide perovskites (MHPs), are found to be a promising candidate for future photovoltaic applications, thanks to their tunable bandgap and ease of fabrication [11, 12].

In this thesis, two types of novel semiconductors — MHPs and narrow-gap semiconductors — are studied in the hope to achieve a more thorough understanding of their optoelectronic properties and hence contribute to the development of future photovoltaic and electronic applications.

1.1 Metal-Halide Perovskites

1.1.1 Background

Perovskites, whose general chemical form is expressed as ABX_3, were originally discovered as the mineral $CaTiO_3$ by a German scientist, Gustav Rose, who took a trip to Russia in 1839 and gave the name "perovskite" in honor of the Russian mineralogist Lev von Perovski [13]. Ever since then, studies on perovskites with various chemical compositions have never ceased. The first synthetic halide perovskite based on cesium and lead was prepared in 1892 by Wells *et al.* [14] in which photoconductivity was observed later by Møller [15]. It was not until 1978, almost a hundred years later, that the first organic-inorganic halide perovskite was developed by Weber [16], in which the cesium cation was replaced by a methylammonium (abbreviated as MA or $CH_3NH_3^+$) cation. In the last two decades, halide perovskites have attracted intensive interest in photovoltaic applications such as light-emitting devices and nonlinear optical crystals for optoelectronics. In particular, solar cells based on MHPs have been investigated extensively and achieved rapidly increasing solar-to-electrical PCE over the last decade. As shown in Figure 1.1, whilst the PCE of solar cells made with conventional inorganic semiconductors such as GaAs and silicon has almost reached a saturation point, the PCE of perovskite solar cells continues to increase from 3.8% to 25.2%, and the perovskite-silicon tandem solar cells have reached an even higher PCE of over 29% [17].

Figure 1.2 shows the lattice structure of perovskite where A is either an organic or inorganic cation such as MA or Cs, B is a metal cation such as lead (Pb) or tin (Sn) and X is a halide anion. The metal and halide ions form corner-sharing octahedral structures with the organic cation located in between, which resembles a pseudo-cubic structure and can change with temperature due to the disordering of the organic cations or tilting of the metal-halide framework [18–21].

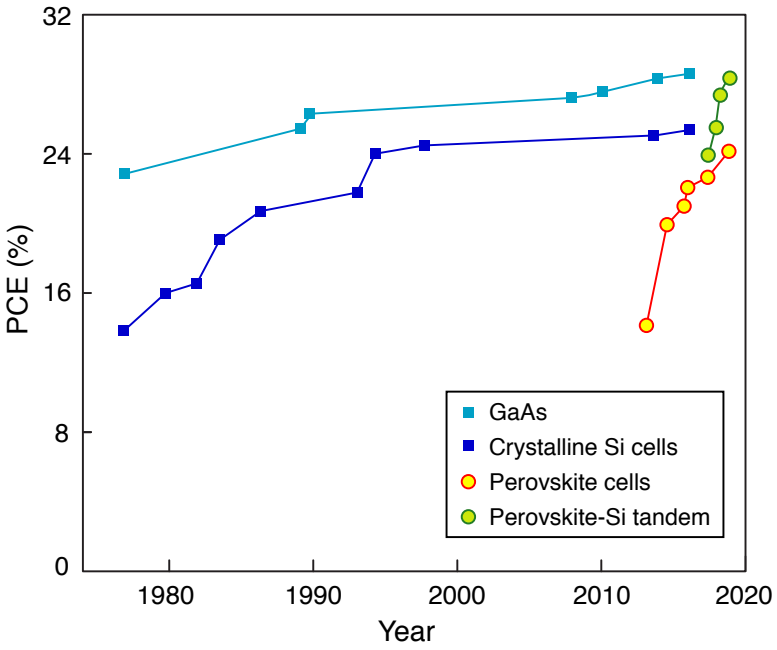

Figure 1.1: Development in PCE of solar cells based on silicon, GaAs and MHPs. Data adapted from Ref. 17.

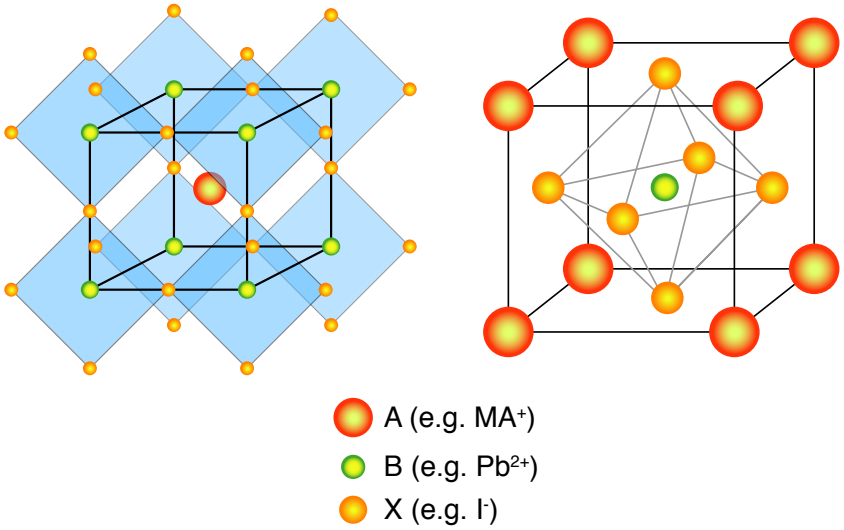

Figure 1.2: Lattice structure of perovskite. The schematic diagram on the left shows the cubic-phase structure of perovskite, whilst the schematic diagram on the right demonstrates the octahedral structure of the BX_6 framework within one unit cell with the organic cations located at the corners.

1.1.2 Growth

There are various fabrication routes to form perovskite thin films such as: (i) one-step process; (ii) two-step process; (iii) vapor-assisted process; and (iv) thermal evaporation process, which can lead to different types and concentrations of impurities as well as vastly different grain sizes within perovskite thin films. This may result in significant differences in their optoelectronic properties such as charge-carrier mobility and diffusion length, which are important limiting factors to the performance of solar cells. This section discusses the fabrication processes of those four major methods as well as their advantages and disadvantages.

One-Step Method

The solution-based spin-coating method is a commonly used one-step method for perovskite thin-film fabrication, where a perovskite precursor solution is prepared with organic halide (e.g. MAI, methylammonium iodide) and inorganic halide (e.g. PbI_2). The precursors are dissolved in gamma-butyrolactone (GBL), dimethylformamide (DMF) or dimethyl sulfoxide (DMSO), which is then spin-coated on a substrate and annealed in a temperature range of 100–150 °C to form pure-phase perovskite film [22]. Furthermore, this solution-based method can also be utilized to make perovskite single crystals via inverse temperature crystallization [23, 24]. In addition, other one-step methods have also been developed to fabricate perovskite layers for solar cells, such as air-blading technique [25], spray coating [26] and inkjet printing [27]. Although those one-step methods have the advantages of easy fabrication and low cost, it is hard to achieve a good control of the perovskite surface morphology, which can affect the perovskite solar cell performance significantly.

Two-Step Method

Similar to the one-step spin-coating method, the two-step method is also solution-processed but without the need to prepare a complete precursor solution. Instead, the PbI_2 layer is coated on the substrate first, after which the PbI_2-coated substrate is dipped into, or spin-coated with, MAI solution. After proper baking, the perovskite film will be formed. This method is able to adjust the parameters in each step separately, which can help improve the morphology of the perovskite film. However, since the spin-coating process in the second step is generally performed at low temperature for a relatively short period of time, the perovskite layer might not be fully formed [28]. The partial dissolving of perovskite may also lead to a rough surface with pinholes [29].

Vapor-Assisted Method

The vapor-assisted method is essentially a modification of the two-step solution method, whose first step also involves preparing a PbI_2-covered substrate. In the second step, instead of dipping the substrate into MAI solution to form perovskite phase, MAI powder is vaporized at low vacuum and deposited on the PbI_2 layer after annealing. This method solves the problem of partial dissolving of perovskite in the second step, which gives rise to large grain size on a micrometer scale and high PCE up to 16.48% [30].

Thermal Vapor Deposition

Among all the typical perovskite fabrication techniques, thermal vapor deposition has the advantage of making uniform perovskite films on a large scale with precise control of the film thickness. In particular, thermal coevaporation [31, 32] which deposits the percursor compounds MAI and PbI_2 simultaneously onto a rotating substrate to ensure uniform perovskite formation has the advantage of not requiring any annealing

step compared to the sequential evaporation method. As a result, a larger range of substrate types can be used for the perovskite film deposition. A recent study on single junction photovoltaic devices prepared by the thermal coevaporation method has reported a PCE value of 19.2% [33], which suggests that this method is an ideal tool for making uniform and high-quality perovskite films for future photovoltaic applications. In this thesis, $MAPbI_3$ polycrystalline films are vapor-deposited by the same method described in Ref. 33, whose optoelectronic properties are investigated and compared with that of $MAPbI_3$ single crystals prepared by the solution-processed method [24].

1.1.3 Applications and Challenges

Compared to organic semiconductors, MHPs exhibit excellent optoelectronic properties such as long charge-carrier diffusion length [34, 35] and high charge-carrier mobility [36–38], which makes them promising for future photovoltaic applications. Various studies have been performed to investigate the performance of planar heterojunction architectures where a perovskite layer is sandwiched between an n-type electron collection layer and a p-type hole collection layer. The PCE measured from the current-density-voltage (J-V) curve has been reported to reach above 19% [39], which suggests that perovskite is ideal for making efficient solar cells in replacement of conventional inorganic semiconductors. Moreover, because of its high absorption coefficient and broad absorption spectrum [40], perovskite is not only an ideal light absorber but also a great light emitter. Since the dominant charge-carrier recombination mechanism in MHPs is bimolecular recombination [41] which is a radiative process, strong photoluminescence (PL) emission is expected. Because the bandgap of MHPs can be easily tuned via compositional substitution in the A-, B- or X-site, MHPs can be made into color-tunable light emitters for lighting and optical communication applications [42]. In addition, since MHPs exhibit narrow emission spectrum

and high photoluminescence quantum efficiency (PLQE), they can also be used for fabricating lasers [43], although higher quality of crystallinity is more crucial in this case to achieve high performance.

Despite the remarkable advantages of MHPs for future photovoltaic applications, there still remain a few problems to overcome. One of the main challenges is to improve the stability of MHPs under realistic atmospheric conditions in the presence of moisture, oxygen and heat [44], which is crucial for commercial applications. While the perovskite might not be rapidly oxidized in dry air [45], exposure to moisture and heat can lead to significant degradation [46,47]. The most straightforward way to solve this problem is to make thorough encapsulation of the perovskite solar-cell devices to prevent the ingress of oxygen and moisture. For instance it has been reported that one effective way is to attach a glass or metal plate to the solar cell by using a slow-permeation epoxy-type sealant [48,49], which is able to prevent both water vapor and oxygen ingress, although photo-induced changes in the polymer morphologies might lead to some degradation as well [50].

Since the most commonly studied MHPs are lead-based (e.g. $MAPbI_3$), toxicity is another big challenge for making the halide perovskite photovoltaic devices commercially viable. While some research has shown that lead-free alternatives such as Sn-based perovskites [51, 52] have narrower bandgaps and higher electrical mobilities than $MAPbI_3$, their poorer stabilities are yet to be improved.

Nevertheless, the excellent optoelectronic properties presented by MHPs and their low-cost fabrication routines still give them great potential in future photovoltaic applications. Further investigations of the charge-carrier transport mechanism in those materials, which is the main focus of this thesis, will help to evaluate the photovoltaic performance of MHPs from a more fundamental perspective and contribute to the commercialization of perovskite-based solar-cell devices.

1.2 Narrow-Gap Semiconductors

1.2.1 Background

Narrow-gap semiconductors whose bandgaps are of the order of magnitude of 0.1 eV, much smaller than that of classical semiconductors such as silicon (1.1 eV), are considered useful for generating and detecting infrared radiation. For instance, their radiation region lying between 5 and 20 μm which covers the atmospheric window (8–14 μm) makes them appropriate for inter-atmospheric communications [53]. Moreover, it has been shown both experimentally and theoretically that narrow-gap semiconductors exhibit small electron effective mass, high electrical mobility, and high thermal conductivity, which makes them ideal for making high-speed electronic devices [54, 55] and thermal image detectors [56]. In addition, theoretical studies have also been performed on narrow-gap semiconductors particularly in terms of the band structure. Calculations based on the Kane model [57] have shown that non-parabolic conduction band is expected in those narrow-gap semiconductors, which has been experimentally proved for some III-V semiconductors such as InSb and GaAs [8–10].

The narrow bandgap also implies high intrinsic charge-carrier density in those materials, which will affect the charge-carrier dynamics significantly. Unlike the MHPs, whose dominant charge-carrier recombination is radiative bimolecular recombination, narrow-gap semiconductors can have dominant Auger recombination depending on the carrier density. Apart from that, the small bandgap energy which is close to some elementary excitations such as phonons opens up another recombination channel via single particles [53]. Furthermore, because of the small bandgap, charge carriers can be easily excited to high energy states in the conduction band, which gives rise to a large population of hot carriers. Investigations of the hot-carrier cooling mechanism will contribute to uncovering a complete picture of the charge-carrier dynamics in those narrow-gap semiconductors.

1.2.2 Defects Formed in Fabrication

One important aspect to consider when investigating the optoelectronic properties of narrow-gap semiconductors is their intrinsic defect properties, which can significantly affect their dopability and hence device performance. For instance, it has been reported that GaSb shows acceptor-like (p-type) defects even though it is fabricated nominally undoped [58], and the acceptor concentration varies with growth conditions. In contrast, InSb can be made either n-doped or p-doped easily, which exhibits a fundamental difference in the native defects from GaSb. According to the hybrid density-functional theory (DFT), from which the defect formation energy is calculated [59], GaSb is p-type when grown in Sb-poor condition, since the dominant defect is negatively charged. In contrast, under Sb-rich condition, due to the presence of both positively-charged and negatively-charged defects, self-compensation between the defects leads to an intrinsic nature. In the case of InSb, there is no self-compensating effect and the negatively-charged defect present in the Sb-poor condition gives rise to p-type InSb, whereas the positively-charged defect arising in the Sb-rich condition results in n-type InSb.

Since the bandgap energy of narrow-gap semiconductors is on the order of magnitude of only 0.1 eV, deep defect state which is ~ 0.1 eV away from the band edge can lie somewhere in the band continuum instead of the bandgap. As a result, shallow defect states caused by long-range Coulomb potential and deep defect states caused by short-range atomic-like potential may coexist in narrow-gap semiconductors, which determines the conductivity and charge-carrier lifetimes [60]. Therefore, defect states of narrow-gap semiconductors, either shallow or deep, play an important role in determining the device performance and great care needs to be taken when investigating extrinsically doped samples.

1.2.3 Applications

Due to their intense infrared radiation, narrow-gap semiconductors have been widely used in infrared optical devices such as infrared detectors as well as infrared lasers. In particular, one of the most studied III-V narrow-gap semiconductors, InSb, has been found to be appropriate for making infrared photodiode-type detectors, since its bandgap energy at room temperature (0.17 eV, 7.3 μm) matches the infrared radiation emitted by the human body (3–25 μm) [61]. Moreover, because it is easy to change the doping concentration, a p-i-n photodiode based on InSb can be optimized to achieve a high photoelectric current, which makes it a practical infrared detector. Meanwhile, the high electrical mobility observed in InSb has been utilized in high-speed transistors which can operate at room temperature [62].

Another increasingly attractive field is to use InSb for fabricating quantum wells, due to its small effective mass which can enhance the quantum confinement. Various studies have been performed on InSb-based quantum wells to investigate the opto-electronic properties such as light-emitting properites [63–65] and spin-orbit interactions [66]. High-frequency single-photon emitters may be realized by InSb quantum wells in the wavelength range of 3–5 μm, which can be utilized in quantum communications.

1.3 Thesis Overview

The primary goal of this thesis is to investigate the charge-carrier dynamics of MHPs and narrow-gap semiconductors, using the technique of terahertz (THz) spectroscopy, based on which their optoelectronic properties may be optimized to achieve high-performance photovoltaic and electronic devices. In **Chapter 2**, the fundamental principles underpinning the charge-carrier transport in perovskite and narrow-gap semiconductors are presented, including the charge-carrier dynamics model and the lattice vibrational modes of MHPs, as well as the electronic band structure and the implication of non-parabolicity of narrow-gap semiconductors. Some significant works performed previously are also reviewed as a guideline for future research. In **Chapter 3**, detailed descriptions of the experimental techniques are provided, including the terahertz time-domain (THz-TDS) spectroscopy and optical-pump-terahertz-probe spectroscopy (OPTPS), which are used for measuring the conductivity, electrical mobility and charge-carrier dynamics of the material. In addition, the magneto-THz spectroscopy, which is an extension of the common THz technique with an external magnetic field applied, is utilized to investigate the cyclotron resonance phenomenon and probe the non-parabolic conduction band of narrow-gap semiconductors.

In **Chapter 4**, the temperature dependence of electrical mobility of the prototypical MHP $MAPbI_3$ is examined in the form of single crystals and polycrystalline thin films using OPTPS. First-principles calculations in conjunction with Boltzmann transport theory are performed to obtain the theoretical values of mobility as a function of temperature, which suggests that the major limiting factor of MHPs' mobility is polar optical phonon scattering, while grain-boundary scattering also plays a vital part in the case of polycrystalline films. In order to gain a better understanding of the role of phonon modes in $MAPbI_3$, **Chapter 5** is dedicated to the investigation of optical phonons in $MAPbI_3$ single crystals and thin films. Stronger electron-phonon coupling effect is observed in the single crystal, which is consistent with the results

presented in Chapter 4 that the electrical mobility of $MAPbI_3$ single crystal is only moderately higher than that of $MAPbI_3$ thin film. Moreover, a blueshift of phonon frequency is observed under photo-excitation. First-principles calculations suggest such effect arises from the increase in dielectric screening due to photo-induced charge carriers.

Chapter 6 examines the optoelectronic properties of InSb, a typical narrow-gap semiconductor, from a slightly different perspective — magneto-THz spectroscopy is utilized to investigate the behavior of cyclotron resonance, from which the electron effective mass of InSb is extracted. A non-parabolic conduction band is confirmed by the increases of effective mass with charge-carrier density, which agrees well with *ab initio* quasiparticle band structure calculations. Moreover, a large population of hot carriers is observed at early time after photo-excitation with a fast cooling rate. The time-resolved magneto-THz spectroscopy is shown to be an ideal tool for investigating the cooling mechanism of hot carriers, thanks to its ability to probe the carrier effective mass on an ultrafast timescale with a precise control of the photo-excitation delay time.

Finally, the knowledge gained from the investigation of the optoelectronic properties of MHPs and narrow-gap semiconductors is summarized in **Chapter 7**, with an outlook of further investigations and future applications. Specifically, the benign grain boundary condition observed in $MAPbI_3$ polycrystalline thin films is promising for upscaling of perovskite-based solar cells and lighting panels; and the fast response of hot carriers presented in InSb might promote further applications of narrow-gap semiconductors in the field of high-speed electronic devices and thermal detectors.

Chapter 2

Fundamental Principles and Previous Work

2.1 Charge-Carrier Transport in Perovskites

2.1.1 Charge-Carrier Dynamics and Photon Reabsorption

In MHP semiconductors, such as $MAPbI_3$, free electrons can be generated via photo-excitation by an above-bandgap ultrafast laser pulse which will decay at a later time via charge-recombination process. Usually, this charge-carrier recombination mechanism is described by the rate equation [67],

$$\frac{\partial n}{\partial t} = G - k_1 n - k_2 n^2 - k_3 n^3, \tag{2.1}$$

where n is the charge-carrier density generated by photo-excitation, k_1 is the monomolecular recombination rate, which is Shockley-Read-Hall trap-mediated; k_2 is the radiative bimolecular recombination rate; and k_3 is the Auger recombination rate which involves a third charged particle. G is the charge-carrier generation rate due to photo-excitation. Figure 2.1 illustrates these three recombination processes,

where the red and blue circles represent an electron and a hole respectively. In monomolecular recombination (Figure 2.1(a)), the photo-excited electron in the conduction band (CB) falls into a trap state within the bandgap which is caused by extrinsic doping or defect. The trapped electron may fall to the valence band (VB) later on, completing the two-step recombination process. In bimolecular recombination (Figure 2.1(b)), the electron in the CB recombines with a hole in the VB, followed by emission of a photon, which is therefore considered as a radiative process. In Auger recombination (Figure 2.1(c)), the excess energy released by the recombination between an electron and a hole is transferred to another electron in the CB and excites it to a higher energy state, which is a non-radiative process.

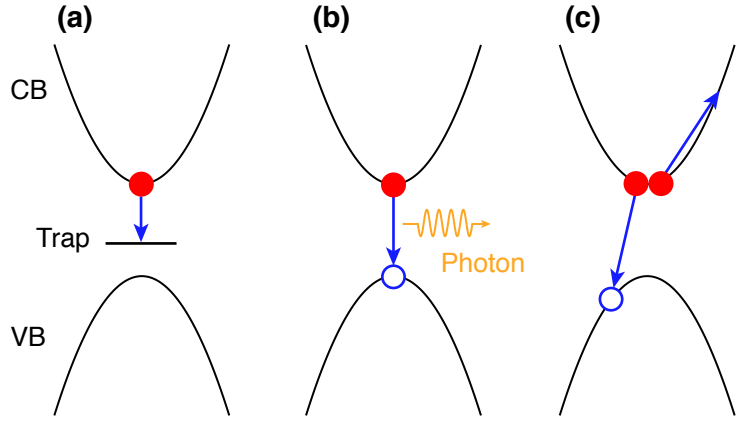

Figure 2.1: Schematics of (a) monomolecular recombination, (b) bimolecular recombination and (c) Auger recombination. The solid red circles and hollow blue circles represent electrons and holes respectively.

As opposed to the charge-carrier recombination process which annihilates electron-hole pairs, there are also some counterpart processes that can create electron-hole pairs. One example is impact ionization which can be regarded as the opposite process to Auger recombination. When an electron with sufficiently large excess kinetic energy drops from a high energy state to a low energy state within the CB, the released excess energy may be transferred to an electron in the VB and excite that electron to the CB, resulting in an electron-hole pair. Generally, a high electric field is required for

the electron to gain sufficient kinetic energy to induce impact ionization, following which an avalanche multiplication of electrons can happen [68]. As more electrons are generated in the CB, they continue to gain energy from the electric field and create more electron-hole pairs via band-to-band transitions. This phenomenon has been widely observed in narrow-gap semiconductors such as InSb [69] and InAs [70]. In contrast, in the case of MHPs, due to their relatively lower electrical mobility and larger energy bandgap, the effect of impact ionization is negligible, and so is Auger recombination at usual charge-carrier concentrations.

Apart from impact ionization, electrons can also be regenerated via photon reabsorption, which is a critical process in MHPs, since the dominant recombination mechanism is the radiative bimolecular recombination. As the photons emitted by bimolecular recombination propagate through the material, they can be reabsorbed before exiting the material, giving rise to more electron-hole pairs, which can delay the recombination process. Therefore, it is crucial to take into account the effect of photon reabsorption when analysing the charge-carrier dynamics of perovskite semiconductors. It has been recently reported that the difference in thickness of $MAPbI_3$ thin films can mask the intrinsic recombination rate due to the effect of photon reabsorption [71]. As the film thickness increases, the photons are more likely to get reabsorbed, which results in lower "apparent" bimolecular recombination rate, whereas the intrinsic recombination rate should be independent of the sample thickness. Therefore, in order to extract the intrinsic charge-carrier recombination rate, Equation (2.1) is modified to

$$\frac{\partial n}{\partial t} = D\frac{\partial^2 n}{\partial z^2} + G' - k_1 n - k_2 n^2 - k_3 n^3, \tag{2.2}$$

where D is the diffusion coefficient and z is the distance along which the charge carriers propagate in the material. Here, the charge-carrier generation rate G' not

only includes the charge carriers generated by initial photo-excitation, but also those generated by photon reabsorption after radiative bimolecular recombination [71]. The diffusion coefficient can be determined from the electrical mobility μ of the charge carriers and is expressed as

$$D = \frac{\mu k_{\mathrm{B}} T}{e}, \tag{2.3}$$

where k_{B} is the Boltzmann constant and T is temperature. Consequently, the charge-carrier diffusion length L_{D} can be calculated according to

$$L_{\mathrm{D}} = \sqrt{\frac{D}{R(n)}}, \tag{2.4}$$

where $R(n) = n^2 k_3 + n k_2 + k_1$ represents the total recombination rate. The diffusion length is a useful parameter to evaluate the optoelectronic performance of photovoltaic devices, as it shows directly how far the charge carriers can travel before they recombine. It is usually estimated under simulated 1 sun illumination ($1\,\mathrm{kWcm^{-2}}$ AM1.5-filtered) which is the normal operating condition of perovskite solar cells.

2.1.2 First-Principles Calculations of Electrical Mobilities

One important aspect to assess the electronic performance of a semiconductor device is the electrical mobility μ which is defined as the drift velocity v_{d} attained by a charge per unit of applied electric field E, i.e. $\mu = v_{\mathrm{d}}/E$. There are various scattering mechanisms that can affect the charge-carrier transport as the carriers travel through the solids. In the case of crystals, Bloch first proposed a quantum-mechanical description of electron scattering which is due to lattice vibrations [72], namely electron-phonon interaction. The key scattering mechanism includes: (1) acoustic-phonon scattering which arises from deformation potential [73, 74]; (2) polar-optical phonon scattering (or Fröhlich coupling) which is induced by longitudinal-optical (LO) phonons in polar crystals [75]; (3) optical deformation potential scattering which exists in non-polar

crystals [76] and (4) piezoelectric scattering due to lattice distortion [77].

Extensive studies of the first-principles calculations of charge-carrier transport in metals and semiconductors have been performed based on the density-functional perturbation theory (DFPT) [78, 79]. In the case of metal-halide perovskites, the Boltzmann transport equation (BTE) approach is utilized in conjunction with the self-energy relaxation approximation, which derives the LO-phonon-limited mobility of electrons and holes in $MAPbI_3$ as a function of temperature. The derivation starts from one of the Kadanoff-Baym equations [80], which is an equation of motion based on the Green's function in quantum theory. It can be solved computationally with a few approximations, including the neglect of the screening of the external potential and the difference between the internal instantaneous electron self-energy and the mean-field potential [81]. Further approximations by neglecting the off-diagonal matrix elements of the Green's function and self-energy leads to the simplified Boltzmann equation for time-independent electric fields in the frequency domain (ω),

$$e\mathbf{E}\cdot\frac{1}{\hbar}\frac{\partial f_{n\mathbf{k}}}{\partial \mathbf{k}} = \int \frac{d\omega}{2\pi}[f^{<}_{n\mathbf{k}}(\omega)\Gamma^{>}_{n\mathbf{k}}(\omega) - f^{>}_{n\mathbf{k}}(\omega)\Gamma^{<}_{n\mathbf{k}}(\omega)], \tag{2.5}$$

where e is the elementary charge; $f^{<}_{n\mathbf{k}}$ and $f^{>}_{n\mathbf{k}}$ represent the diagonal matrix elements of the lesser and greater Green's function respectively; $\Gamma^{<}_{n\mathbf{k}}$ and $\Gamma^{>}_{n\mathbf{k}}$ represent the matrix elements of the lesser and greater self-energy respectively. According to the definition of $f^{<,>}_{n\mathbf{k}}$ given in Ref. 81, the occupation number $f_{n\mathbf{k}}$ shown on the left-hand side of Equation (2.5) represents the fractional number of electrons in a state of band n and momentum $\mathbf{k}$, and is expressed as

$$f_{n\mathbf{k}} = \int \frac{d\omega}{2\pi} f^{<}_{n\mathbf{k}}(\omega). \tag{2.6}$$

In the specific case of lattice scattering which is used for modelling the electron-phonon interaction in $MAPbI_3$ perovskite, the greater and lesser counterparts of the

self-energy are approximated as the diagonal matrix elements of the Fan-Migdal self-energy [82]. With further approximations, namely Born-Oppenheimer approximation, frequency-independent approximation of the electron-phonon matrix elements and the unperturbed Hamiltonian approximation of the electronic Green's function, the BTE is expressed as [81]

$$-ev^{\beta}_{n\mathbf{k}}\frac{\partial f^0_{n\mathbf{k}}}{\partial \varepsilon_{n\mathbf{k}}} = \sum_m \int \frac{d^3q}{\Omega_{\mathrm{BZ}}}[\tau^{-1}_{m\mathbf{k}+\mathbf{q}\to n\mathbf{k}}\partial_{E\beta} f_{m\mathbf{k}+\mathbf{q}} - \tau^{-1}_{n\mathbf{k}\to m\mathbf{k}+\mathbf{q}}\partial_{E\beta} f_{n\mathbf{k}}], \tag{2.7}$$

where the partial decay rate τ^{-1} is defined as

$$\begin{aligned}\tau^{-1}_{n\mathbf{k}\to m\mathbf{k}+\mathbf{q}} = &\sum_v \frac{2\pi}{\hbar}|g_{mn\nu}(\mathbf{k},\mathbf{q})|^2 \\ &\times [(n_{\mathbf{q}\nu}+1-f^0_{m\mathbf{k}+\mathbf{q}})\delta(\Delta\varepsilon^{nm}_{\mathbf{k},\mathbf{q}}-\hbar\omega_{\mathbf{q}\nu}) \\ &+ (n_{\mathbf{q}\nu}+f^0_{m\mathbf{k}+\mathbf{q}})\delta(\Delta\varepsilon^{nm}_{\mathbf{k},\mathbf{q}}+\hbar\omega_{\mathbf{q}\nu})].\end{aligned} \tag{2.8}$$

The equilibrium occupancy $f^0_{n\mathbf{k}}$ in the absence of electric field is given by the Fermi-Dirac distribution which is calculated at the band energies and defined as $f^0_{n\mathbf{k}} = 1/\{\exp[(\varepsilon_{n\mathbf{k}}-\mu_{\mathrm{F}})/k_{\mathrm{B}}T]+1\}$ where μ_{F} denotes the chemical potential. From the solution to Equation (2.7), the linear response coefficient $\partial_{E\beta} f_{n\mathbf{k}}$ is obtained, which is short for $(\partial f_{n\mathbf{k}}/\partial E_\beta)|_{\mathbf{E}=\mathbf{0}}$ and used for calculating the conductivity tensor $\sigma_{\alpha\beta}$,

$$\sigma_{\alpha\beta} = \left.\frac{\partial J_{\mathrm{M},\alpha}}{\partial E_\beta}\right|_{\mathbf{E}=\mathbf{0}} = \frac{-e}{V_{\mathrm{uc}}}\sum_n \int \frac{d^3k}{\Omega_{BZ}} v^{\alpha}_{n\mathbf{k}}\partial_{E\beta} f_{n\mathbf{k}}, \tag{2.9}$$

where J_{M} is the macroscopic average of the current density; V_{uc} and Ω_{BZ} represent the volumes of the unit cell and the first Brillouin zone respectively; and $v_{n\mathbf{k}}$ is the drift velocity. The indices α and β run over three Cartesian directions.

In the case of semiconductors, since the carrier density can be significantly affected by external factors such as doping density, temperature and applied electric field, the

carrier drift mobility is introduced to describe the intrinsic electronic property,

$$\mu^{\mathrm{d}}_{\alpha\beta} = \left|\frac{\sigma_{\alpha\beta}}{en_{\mathrm{e}}}\right|, \tag{2.10}$$

where the electron density n_{e} is defined as

$$n_{\mathrm{e}} = \frac{1}{V_{\mathrm{uc}}} \sum_{n\in\mathrm{CB}} \int \frac{d^3k}{\Omega_{\mathrm{BZ}}} [f^0_{n\mathbf{k}}(\mu_{\mathrm{F}}, T) - f^0_{n\mathbf{k}}(\varepsilon_{\mathrm{F}}, 0)]. \tag{2.11}$$

As a result, this *ab initio* calculation based on BTE is able to predict reasonable phonon-limited mobility values and demonstrate a power-law temperature dependence of mobility across different lattice phases including orthorhombic, tetragonal and cubic phases [83]. While previous experimental work shows similar temperature-dependence of mobility, due to the inaccurate measurement of the sample temperature, there still exists some discrepancy between experiment and theory. As will be discussed in more details in Chapter 4, with the help of the PL-facilitated THz spectroscopy, a good agreement in $MAPbI_3$ single crystal's mobility between experiment and theory is finally achieved.

2.1.3 Grain-Boundary Scattering in Polycrystalline Films

It should be noted that the first-principles calculations based on the BTE place an upper limit of the electrical mobility of $MAPbI_3$ perovskite, since only electron-phonon interactions are considered, whereas in practice, impurities and defects present in the perovskite samples can suppress the mobility. Apart from that, the presence of grain boundaries in polycrystalline films is another important limiting factor of the electrical mobility, especially when the charge-carrier mean free path is larger than the grain size. In order to incorporate the effect of grain-boundary scattering on carrier mobility in polycrystalline films, the model of Mayadas and Shatzkes (MS) [84] is implemented where the mean free path of charge carriers is limited by the extent of

grain boundaries. The MS model is an extension of the Boltzmann transport theory which includes the transmission and reflection of the conduction band electrons at grain boundaries. The resultant resistivity of a polycrystalline film is expressed as [84, 85]

$$\rho_{\mathrm{MS}} = \rho_0 \left[1 - \frac{3}{2}\alpha + 3\alpha^2 - 3\alpha^3 \ln\left(1 + \frac{1}{\alpha}\right)\right]^{-1}, \tag{2.12}$$

where ρ_0 is the bulk resistivity of the material, $\alpha = (\lambda/g)R/(1-R)$ with λ and g representing the mean free path and the grain size respectively. R is the probability of the electrons getting reflected at the grain boundaries, which is in the range between zero and one and usually approximated as 0.5 [85, 86]. Since the resistivity is defined as the reciprocal of conductivity $\sigma = ne\mu$, the electrical mobility of the polycrystalline thin film can be written as

$$\mu_{\mathrm{film}} = \mu_{\mathrm{phonon}} \left[1 - \frac{3}{2}\alpha + 3\alpha^2 - 3\alpha^3 \ln\left(1 + \frac{1}{\alpha}\right)\right], \tag{2.13}$$

where μ_{phonon} is the bulk mobility of a single crystal, which is predicted by the *ab initio* calculations and phonon-limited only. To obtain the expression for the temperature dependence of mobility, the electron mean free path is computed *ab initio* by direction-averaging the mean free path weighted by a transport occupation:

$$\lambda_{\mathrm{transport}} = \frac{\sum_{\alpha,n\mathbf{k}} w_{\mathbf{k}} f_{n\mathbf{k}}(1 - f_{n\mathbf{k}}) |\mathbf{v}^{\alpha}_{n\mathbf{k}}| \tau_{n\mathbf{k}}}{3 \sum_{n\mathbf{k}} w_{\mathbf{k}} f_{n\mathbf{k}}(1 - f_{n\mathbf{k}})}, \tag{2.14}$$

where $w_{\mathbf{k}}$ is the $\mathbf{k}$-point weight, $f_{n\mathbf{k}}$ is the Fermi-Dirac occupation function defined by Equation (2.6), $\mathbf{v}_{n\mathbf{k}}$ is the electron velocity and $\tau_{n\mathbf{k}}$ is the electron-phonon lifetime for a state of band n and momentum $\mathbf{k}$. Combining Equations (2.13) and (2.14), the mobility of the polycrystalline thin film can be computed as a function of temperature with the grain size g being the only changing parameter. Therefore, given the experimental data of the temperature-dependent mobility of a polycrystalline film,

the actual grain size can be determined from the best-fit theoretical mobility curve which is computed at a specific value of g.

2.1.4 Lattice Vibrations in Perovskites

Optical phonons which arise from lattice vibrations play a vital role in limiting the electrical mobility of perovskites via electron-phonon coupling. Theoretical studies based on DFT have shown that the dominant mechanism that limits the perovskite mobility is the LO-phonon scattering (Frölich interaction) which comes from the Pb–I bond fluctuations [83]. In this section, phonon modes observed in theoretical calculations and experiments will be discussed and by comparison, certain lattice vibrational modes will be assigned.

The commonly used computational tool for investigating lattice vibrations in solids is QUANTUM ESPRESSO, an integrated suite of computer codes which is able to perform electronic-structure calculations based on DFT and DFPT [87]. Generally, the phonon modes of $MAPbI_3$ are calculated in the *Pnma* orthorhombic phase, which has been resolved by X-ray diffraction measurements [88]. A recent study comparing the phonon modes predicted from computational analysis and obtained from experimental infrared absorption spectra shows that there are three major vibrational modes in $MAPbI_3$: (i) the internal vibrations of the MA cations; (ii) the cation librations and (iii) the internal vibrations of the PbI_3 framework [89]. In the THz frequency regime, the dominant modes are found to be the stretching and bending vibrations of the PbI_3 framework with frequencies lower than $140\,cm^{-1}$. Specifically, two Pb–I stretching modes are identified at 22 and $30\,cm^{-1}$, which is just within the detection range of the THz spectroscopy measurement performed in this thesis. In contrast, the stretching, rocking and bending modes of MA cations locate at much higher frequencies ranging from 800 to $3100\,cm^{-1}$, which can be measured by Fourier-transform infrared spectroscopy (FTIR).

In addition, as a polar solid, splitting between the LO and transverse optical (TO) phonons is expected in $MAPbI_3$. Calculations of the non-analytic part of the dynamical matrix [90] suggest that the distance between most normal LO and TO modes is less than $10\,cm^{-1}$, with an exception occurring in the PbI_3 framework whose LO-TO splitting is over $50\,cm^{-1}$ [89]. Meanwhile, the LO-TO splitting can be expressed by the Lyddane-Sachs-Teller (LST) relationship [91],

$$\frac{\omega_{LO}^2}{\omega_{TO}^2} = \frac{\varepsilon_{stat}}{\varepsilon_\infty}, \tag{2.15}$$

where ε_{stat} and ε_∞ represent the static (low-frequency) dielectric constant and high-frequency dielectric constant of the material. In the THz spectroscopy measurements, since the incident THz pulse is a transverse wave, TO phonons are excited and their frequencies can be extracted directly from the conductivity spectrum, whereas the frequencies of LO phonons are calculated using Equation (2.15). More details of the characterization of phonon modes in $MAPbI_3$ based on the experimental conductivity spectrum will be given in Chapter 3.

Due to the close relationship between phonon modes and charge-carrier transport in MHPs, various studies have been performed to elucidate the mechanism of lattice fluctuations and the effects on electronic properties. A recent DFT study reveals that the reorientation of the organic cation MA can distort the inorganic halide octahedra, which may change the bandgap of $MAPbI_3$ from direct to indirect and reduce the charge-carrier recombination rates, giving rise to longer carrier lifetimes [92]. Meanwhile, the structural change of the inorganic PbI_6 cage can also be induced by photo-excitation [93], in which case the absorption of photons may lead to electron migration from the I^- site to the Pb^{2+} site. As a result, the Pb–I bond is strengthened and the phonon modes shift to higher frequency. In addition, light-induced weakening of the hydrogen bond in MHPs can cause reordering of the organic cations, which will

significantly affect the piezoelectric response [94]. In the presence of photo-induced charge carriers, the polarization of the dipoles in perovskite is enhanced, which also contributes to the strong increase of piezoelectricity in $MAPbI_3$ [95].

In order to gain a deeper understanding of the phonon modes in MHPs, one major focus of this thesis is to conduct a comparative study between $MAPbI_3$ single crystals and thin films utilizing THz spectroscopy technique as well as *ab initio* computational methods. As will be shown in the following chapters, the consistency between the experimental and theoretical results gives a clear indication of a strong electron-phonon coupling effect in MHPs. Meanwhile, photo-induced charge carriers tend to cause phonon hardening at THz frequencies due to the increase in dielectric screening.

2.2 Electronic Band Structure and Charge-Carrier Relaxation of InSb

2.2.1 Non-Parabolic Conduction Band

InSb, a member of the III-V compound semiconductors, has been extensively studied over the last few decades due to its peculiar optoelectronic properties such as extremely small energy bandgap and ultrafast electrical mobility. In particular, it has been proved both theoretically and experimentally that its conduction band exhibits a non-parabolic feature, which may underlie various unique electronic behaviors such as the quantization of absorption coefficient under magnetic field [96, 97]. The non-parabolicity of the conduction band of InSb was originally derived by Kane, based on $\mathbf{k}\cdot\mathbf{p}$ perturbation theory [98]. In the Kane model, the Bloch theorem is applied to the Schrödinger equation which describes the motion of an electron as follows [99],

$$\mathcal{H}\psi_n(\mathbf{r}) = \left(\frac{\mathbf{p}^2}{2m} + V(\mathbf{r})\right)\psi_n(\mathbf{r}) = E_n\psi_n(\mathbf{r}), \tag{2.16}$$

where $\mathcal{H}$, $\psi_n(\mathbf{r})$ and E_n represent the Hamiltonian, the wave function and the energy of an electron, respectively, with n denoting the band index and $\mathbf{r}$ denoting the position. $\mathbf{p} = -i\hbar\nabla$ is the operator of momentum and m is the mass of the electron. $V(\mathbf{r})$ is the potential experienced by the electron which can be due to the presence of an electric field. By substituting the solution $\psi_{n\mathbf{k}} = \exp(i\mathbf{k}\cdot\mathbf{r})u_{n\mathbf{k}}(\mathbf{r})$ into Equation (2.16), the following equation is obtained,

$$\left(\frac{p^2}{2m} + \frac{\hbar\mathbf{k}\cdot\mathbf{p}}{m} + \frac{\hbar^2k^2}{2m} + V(\mathbf{r})\right)u_{n\mathbf{k}}(\mathbf{r}) = \varepsilon_n(\mathbf{k})u_{n\mathbf{k}}(\mathbf{r}), \tag{2.17}$$

where $u_{n\mathbf{k}}(\mathbf{r})$ is the periodic potential of the lattice and $\varepsilon_n(\mathbf{k})$ is the eigenenergy of the electron. The perturbation terms, $\hbar(\mathbf{k}\cdot\mathbf{p})/m$ and $\hbar^2k^2/(2m)$, can be treated by either degenerate or nondegenerate perturbation theory. The advantage of this method is that only a few input parameters are required for the calculation, which can be determined experimentally. Defining the interband matrix element of $\mathbf{k}\cdot\mathbf{p}$ interaction as $P(\mathbf{k}) = -i\langle S|\frac{\hbar}{m}\mathbf{k}\cdot\mathbf{p}|\psi_n\rangle$ where S is the spin operator, the effective mass m^* of narrow-gap semiconductors such as InSb can be written as [100]

$$\frac{m_\mathrm{e}}{m^*} = 1 + \frac{2m_\mathrm{e}P^2}{E_\mathrm{g}}, \tag{2.18}$$

where m_e is the inertial mass of a free electron and E_g is the forbidden energy bandgap. Since E_g is usually smaller than 2 eV for narrow-gap semiconductors (for instance $E_\mathrm{g} = 0.17\,\mathrm{eV}$ for InSb at room temperature), $2m_\mathrm{e}P^2/E_\mathrm{g} \gg 1$ and Equation (2.18) is simplified as

$$\frac{m^*}{m_\mathrm{e}} \approx \frac{E_\mathrm{g}}{2m_\mathrm{e}P^2} \ll 1, \tag{2.19}$$

which confirms that the effective mass in the Kane model is always smaller than the inertial mass of a free electron. Meanwhile, the small bandgap also gives rise to strong interaction between conduction and valence bands, which results in a non-parabolic

conduction band dispersion relation ε_c,

$$\varepsilon_c(1+\alpha\varepsilon_c) = \frac{k^2}{2m_0^*}, \tag{2.20}$$

where $\alpha = (1-m^*/m_0^*)^2/E_g$ is defined as the non-parabolicity constant [57] which has the dimension of an inverse energy. m_0^* is the effective mass at the conduction band minimum where $\alpha = 0$ and hence the conduction band is approximately parabolic near the conduction band minimum. Away from the conduction band minimum, however, the effective mass is no longer constant, but changes with energy as

$$m^*(\varepsilon_c) = m_0^*(1+2\alpha\varepsilon_c). \tag{2.21}$$

The density of states (DOS) of a non-parabolic conduction band is written as

$$g(\varepsilon_c) = \frac{1}{2\pi^2}\left(\frac{2m_0^*}{\hbar^2}\right)^{3/2}(1+2\alpha\varepsilon_c)\sqrt{\varepsilon_c(1+\alpha\varepsilon_c)}, \tag{2.22}$$

which is used for calculating the charge-carrier density based on the Fermi-Dirac distribution $f(\varepsilon_c;\mu_F)$,

$$N(\mu_F) = \int_0^\infty g(\varepsilon_c)f(\varepsilon_c;\mu_F)d\varepsilon_c. \tag{2.23}$$

Experimentally, it is hard to distinguish the electrons at different energy levels, which means what is actually being measured is an average of the effective mass over the entire electron population in the conduction band, which is equivalent to

$$m^*_{\text{mean}}(\mu_F;T) = \frac{\int_0^\infty m^*(\varepsilon_c)g(\varepsilon_c)f(\varepsilon_c;\mu_{F,T})d\varepsilon_c}{\int_0^\infty g(\varepsilon_c)f(\varepsilon_c;\mu_{F,T})d\varepsilon_c}. \tag{2.24}$$

In order to verify the non-parabolicity of InSb, various cyclotron resonance measurements have been performed at frequencies from infrared to microwave [8, 101]. The key indication of the non-parabolicity of conduction band is that the electron

effective mass changes with carrier density or magnetic field strength. Among most of the cyclotron resonance experiments, InSb samples under investigation are usually extrinsically doped (either n-type or p-type). When an external magnetic field is applied, the charge carriers in the doped InSb sample undergo cyclotron motion and certain frequency components of the incident light will get absorbed so that the electrons are excited to higher Landau levels. The frequency at which the cyclotron resonance occurs is determined by the electron effective mass and the applied magnetic field,

$$\omega_{\mathrm{c}} = \frac{eB}{m^*}, \tag{2.25}$$

where ω_{c} is the so-called cyclotron resonance frequency, e is the elementary charge and B is the magnetic field strength. As the carrier density increases, the electrons start to occupy higher energy states in the conduction band and due to the non-parabolic effect on the effective mass given by Equation (2.21), the effective mass increases with carrier density. On the other hand, the electron effective mass is also found to increase with magnetic field [9,10], due to the nonlinear dependence of Landau levels on magnetic field [102]. As the magnetic field increases, the spacing between Landau levels increases as well, which causes the electrons to reach a flatter region of the conduction band and hence exhibit larger effective mass.

Although the non-parabolic band structure of n-type InSb has been extensively investigated over the last few decades, few studies have been performed on intrinsic InSb where the impurity scattering is negligible. Therefore, in this thesis, the electron effective mass is measured in an intrinsic (undoped) InSb sample by injecting electrons into the conduction band via photo-excitation, from which the electron effective mass is probed as a function of photo-excitation fluence to quantify the non-parabolicity of InSb. Since the carrier density in the conduction band is simply controlled by the photo-excitation fluence, the change of effective mass can be investigated within one sample, which helps to obtain more consistent results.

2.2.2 Hot Carrier Relaxation Mechanism

Due to the extremely small energy bandgap of InSb, hot charge carriers are generated in the conduction band when excess kinetic energy is gained from photo-excitation. For instance, it was reported that under an excitation pulse of 4.1 μm (0.3 eV), the temperature of thermal distribution of electrons in InSb after 1.7 ps was $\sim$ 370 K when the sample was held at 10 K [103]. The excessive hot carriers present in the conduction band of InSb make it crucial to take into account the effect of thermalization when analyzing the charge-carrier dynamics and transport behavior of InSb. In particular, in the magneto-THz spectroscopy measurement of the intrinsic InSb sample where charge carriers are generated by an ultrafast laser pulse with photon energy at 1.55 eV, a large number of hot electrons are injected into the conduction band, which gives rise to a wide range of measurable cyclotron resonance frequencies. Neglecting the thermal distribution of hot electrons at early photo-excitation times can lead to inaccurate determination of the non-parabolicity of the conduction band.

In the last few decades, intensive studies have been performed on InSb in terms of its hot-carrier cooling mechanism. According to the magnetoresistance measurement performed on n-type InSb by Stradling and Wood [104], when the electron temperature is in excess of 20 K, LO phonon scattering dominates the hot-electron cooling process. In contrast, when the electron temperature is between 10–20 K, the emission of two transverse-acoustic (TA) phonons at the band edge becomes dominant, since the thermal energy of the electrons is below the LO phonon emission threshold. Moreover, when the electron temperature drops below 10 K, relaxation by a single acoustic phonon via deformation and piezoelectric potential scattering becomes dominant. On the other hand, Martin and Mead proposed a two-phonon process which involves the emission of a TO phonon and the absorption of a TA phonon at electron temperature between 12–34 K based on the electrical conductivity measurement [105]. Furthermore, a model involving two electron temperatures was proposed by Shimo-

mae *et al.* [106] where the electron distribution is approximated by the Maxwellian distribution:

$$f(\varepsilon) = \exp(-\varepsilon/k_{\mathrm{B}}T_{\mathrm{e}}), \quad \text{for} \quad \varepsilon \leq \hbar\omega_{\mathrm{LO}} - \varepsilon_{\mathrm{I}}, \tag{2.26}$$

$$f(\varepsilon) = \exp(-\varepsilon/k_{\mathrm{B}}T_{\mathrm{L}}), \quad \text{for} \quad \varepsilon > \hbar\omega_{\mathrm{LO}} - \varepsilon_{\mathrm{I}}, \tag{2.27}$$

where ε is the electron energy and ε_{I} is the impurity energy which determines the LO phonon emission threshold as $(\hbar\omega_{\mathrm{LO}} - \varepsilon_{\mathrm{I}})$. T_{e} and T_{L} represent the electron temperature and lattice temperature respectively. When the electron energy is above the LO phonon emission threshold, the electron temperature is approximated as the lattice temperature, which results in the electron distribution given by Equation (2.27).

Some theoretical work has also shown that the non-parabolicity of the conduction band has a remarkable cooling effect on the hot carriers, due to its enhancement of the carrier scattering rate in particular for high-energy free electrons [107]. Under the consideration of non-parabolic conduction band, the electron distribution function is found to be stable and normalizable [108]. Apart from that, if the energy of the incident electromagnetic wave is smaller than the energy bandgap, intraband free-electron absorption can be assisted by interactions with a third particle, such as optical or acoustic phonons or impurities, which results in a heated electron system. When the hot electrons cool down again, which is accompanied by the emission of LO phonons, the thermal optical phonon distribution will be disturbed and affect the absorption coefficient in turn [109]. By taking into account the effect of the non-parabolic conduction band, the computed absorption coefficients for III-V semiconductors including InSb, InAs and GaAs are shown to be in better agreement with the experimental results than those computed from the parabolic models.

Moreover, the effects of the non-parabolicity of the conduction band on the density of states and the scattering probability need to be considered when calculating the energy loss rate of hot electrons. As reported by Kahlert and Bauer [110], the com-

puted energy loss rates based on the Kane model agree well with other experimental results, which suggests that at $T_e < 12\,K$, the deformation-potential and piezoelectric scattering are the dominant scattering mechanisms, whereas at $T_e > 24\,K$, LO phonon scattering becomes dominant. However, in the intermediate temperature range (12–24 K), a two-phonon-scattering process was proposed to account for the difference between the experiment and the theory.

In this thesis, the hot-electron cooling process of InSb is investigated via time-resolved magneto-THz spectroscopy, which not only allows the electron effective mass of the intrinsic InSb sample to be measured as a function of electron density, but also enables the hot-electron dynamics to be investigated on an ultrafast timescale. Cyclotron resonance can be measured at a few picoseconds to hundreds of picoseconds after photo-excitation, from which the evolution of hot electrons is compared to that obtained using *ab initio* calculations based on *GW* approximations.

Chapter 3

Experimental Techniques

3.1 Terahertz Spectroscopy

Terahertz waves lie in the wavelength range between 3 mm and 0.03 mm, corresponding to 0.1 THz and 10 THz. THz spectroscopy is an ideal non-contact and non-invasive method to probe materials' optoelectronic properties, which is advantageous as the influence of metallic contacts is removed and the high frequency electric field of THz probe avoids the complications associated with ion migration, which occurs on a much longer timescale. Using THz spectroscopy, charge-carrier mobility, photoconductivity and cyclotron resonance can be measured with great accuracy and with sub-picosecond temporal resolution, which enables some ultrafast electronic processes such as hot-carrier cooling and charge-carrier recombination to be investigated in more detail. Here, three major THz spectroscopy techniques including THz time-domain spectroscopy, optical-pump-THz-probe spectroscopy and magneto-THz spectroscopy are utilized to investigate the charge-carrier dynamics and electronic band structure of some semiconductor materials.

3.1.1 THz Time-Domain Spectroscopy (THz-TDS) and Optical-Pump-THz-Probe Spectroscopy (OPTPS)

THz time-domain spectroscopy (THz-TDS) is a useful method to measure semiconductor materials' conductivity, from which the dielectric function can be extracted. Moreover, in the case of MHPs, since various phonon modes are present in the THz range [89, 111], THz-TDS is also used for identifying certain phonon modes. In Figure 3.1, a schematic of the THz spectroscopy setup used for the studies presented in this thesis is illustrated. An ultrafast laser beam with 4 W average power, 35 fs pulse width, 5 kHz repetition rate and 800 nm central wavelength is split into three paths, which are denoted as "THz beam", "gate beam" and "pump beam" respectively. The THz beam is generated by inverse spin Hall effect utilizing a THz spintronic emitter [112, 113]. The gate beam is used for probing the THz pulse in time domain via the electro-optic sampling technique. The THz signal is detected by a 0.2 mm-thick (110) ZnTe crystal in conjunction with a quarter-wave plate, a Wollaston prism and a pair of balanced photodiodes.

Optical-Pump-THz-Probe spectroscopy (OPTPS) is an extension of THz-TDS with an extra pump beam which is used for photo-exciting the semiconductor material and generating charge carriers in the conduction band. Depending on the bandgap of the material, the pump beam which is originally at 800 nm can also be converted to 400 nm using a β-barium borate (BBO) crystal. For instance, since the perovskite $MAPbI_3$ has a bandgap around 780 nm according to its PL and absorption spectra, a pump beam at 400 nm is applied; whereas in the case of the intrinsic InSb sample whose bandgap is only 0.17 eV (7300 nm) at room temperature, the pump beam is kept at 800 nm.

When the pump beam and THz (probe) beam overlap simultaneously and spatially on the semiconductor sample, charge carriers will be generated upon photo-excitation. By varying the time delay between the pump and THz beams, the change of THz

transmission is measured as a function of time, from which the charge-carrier dynamics and mobility can be determined (details of the data analysis methods will be given in Section 3.1.3). On the other hand, the photoconductivity spectrum can be measured at a certain time (e.g. 0, 5 or 200 ps) after photo-excitation by fixing the time delay between the pump peam and the THz beam.

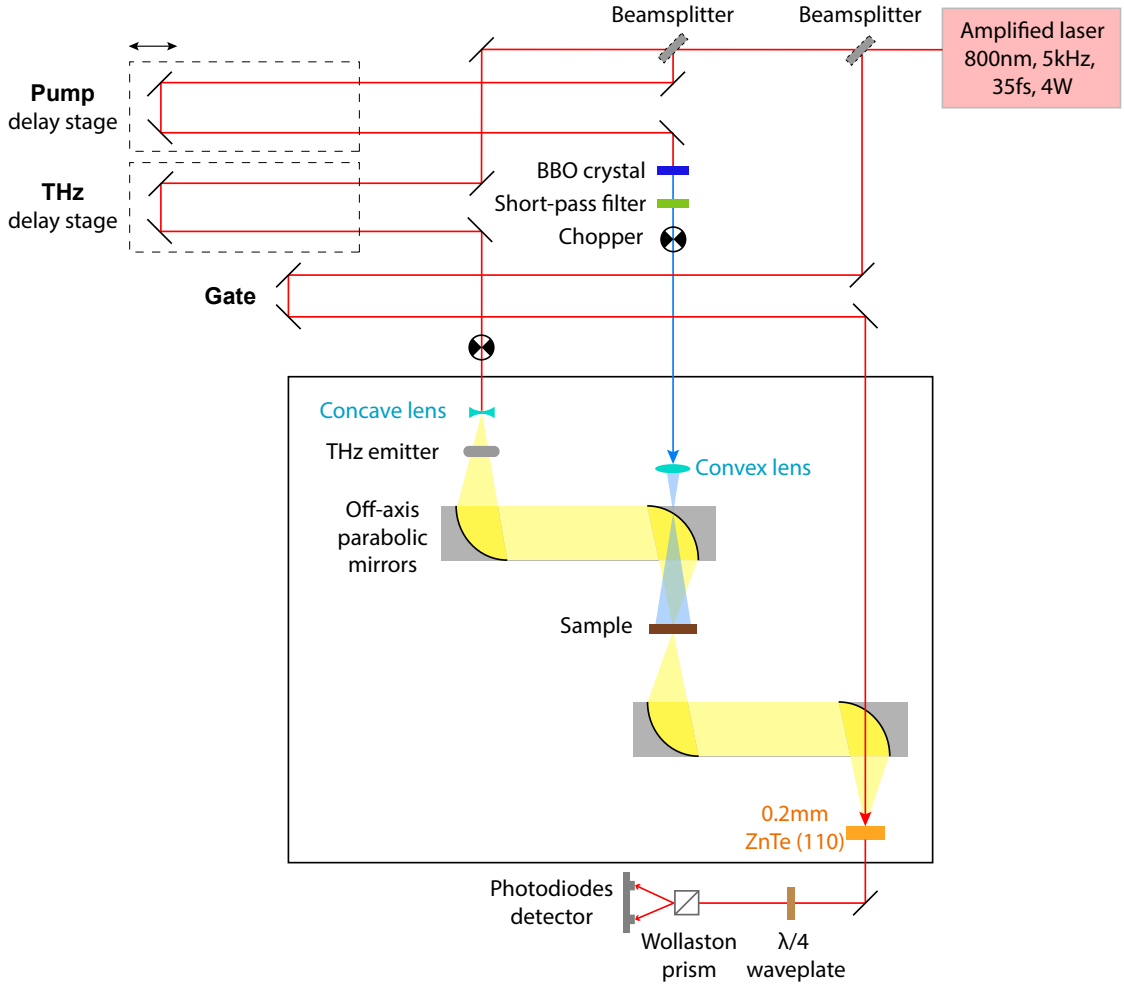

Figure 3.1: A schematic diagram of the THz spectroscopy setup in transmission geometry. The amplified laser pulse is split into three paths, THz beam, pump beam and gate beam. The THz pulse is generated by a THz spintronic emitter and detected via electro-optic sampling. The THz delay stage is used for changing the time delay between the THz beam and the gate beam in the THz-TDS, from which a time-domain trace of the transmitted THz pulse is obtained. The pump delay stage is used for changing the photo-excitation delay time in the OPTPS.

THz-TDS and OPTPS are widely used on thin film samples, since the THz pulse can propagate through without being absorbed too much by the sample. However, in some other cases where the sample is much thicker, such as $MAPbI_3$ single crystal, the transmission of THz is too weak to be detected. Alternatively, the reflection of THz signal from the sample surface is measured and the charge-carrier dynamics and photoconductivity of the sample are investigated based on the reflectivity spectrum. Figure 3.2 shows the schematic of the THz spectroscopy setup which includes both transmission and reflection detection modes. In addition to the original THz spectroscopy setup shown in Figure 3.1, another gate beam is introduced to probe the THz pulse in reflection. Likewise, the reflected THz pulse from the sample surface is directed to another set of (110) ZnTe crystal, quartz-wave plate, Wollaston prism and a pair of photodiodes. Apart from that, the PL spectrum emitted from the sample under photo-excitation is collected by a fibre-coupled spectrometer (Horiba Scientific, iHR320) and detected by a CCD (Horiba Scientific, Si Symphony II). The THz-TDS and OPTPS are also compatible with temperature-dependent measurements where the sample is mounted on a cold-finger cryostat to change the temperature. As will be discussed in more detail later, the simultaneously measured temperature-dependent PL spectrum of the sample can be also used for determining the sample temperature accurately.

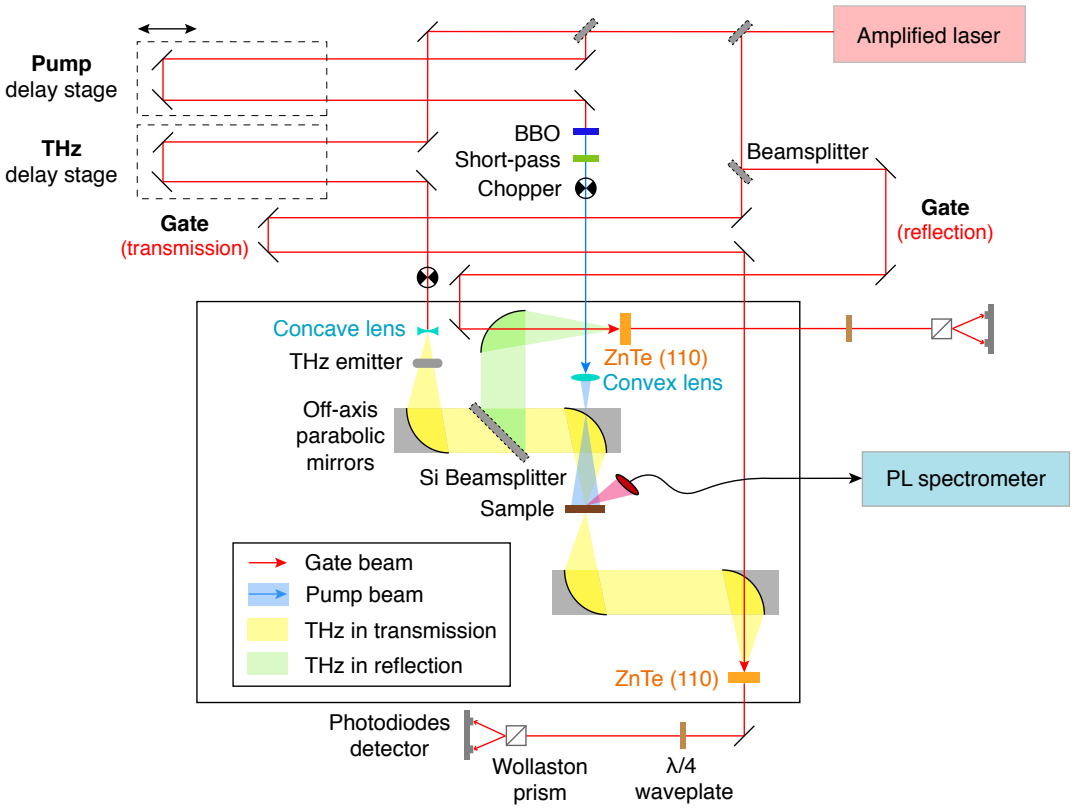

Figure 3.2: A schematic of the THz spectroscopy setup with an extra reflection detection mode. The reflected THz pulse from the sample surface is redirected by a silicon beam spitter onto another 0.2 mm-thick (110) ZnTe detection crystal. The PL signal scattered from the sample surface is collected by a fibre-coupled spectrometer.

3.1.1.1 THz Generation

As mentioned in the preivous section, the THz pulse is generated by a spintronic THz emitter (STE) which is based on the inverse spin Hall effect [112]. This is a process of turning spin current into electric current. As demonstrated in Figure 3.3, the STE consists of three thin layers with one ferromagnetic (FM) layer sandwiched between two non-magnetic (NM) layers. The FM layer is made of $Co_{40}Fe_{40}B_{20}$ which is 1.8 nm thick and the two NM layers are Pt (NM1) and W (NM2), respectively, both of which are 2 nm thick. The STE is deposited on a 2 mm-thick sapphire substrate. The STE is placed between two bar magnets so that the magnetic field is parallel to the surface of the STE. Under the magnetic field, the majority of the electrons inside the FM layer have their spins aligned with the magnetic field and when a femtosecond laser pulse is incident on the STE, these electrons will be driven into the NM layers on both sides, generating a spin current j_s. The two NM layers are chosen to have opposite spin Hall angles, therefore, the electrons will be deflected in the same direction, generating a net electric current perpendicular to the magnetic field inside the NM layers, which is denoted as j_c. Furthermore, due to the spin-orbit coupling effect, the electric current eventually propagates in the direction of the femtosecond pump laser. The resulting THz radiation is polarized in a direction perpendicular to the magnetic field and parallel to the STE surface.

STE is an ideal THz emitter due to its ultrabroad bandwidth and high signal-to-noise ratio (SNR) [113]. As shown in Figure 3.4(b), compared to ZnTe crystal, THz radiation generated by STE has a much wider bandwidth, which is more than twice the bandwidth of ZnTe. The smoother curve of the THz signal generated by STE shown in Figure 3.4(a) also suggests that STE has a better SNR than ZnTe.

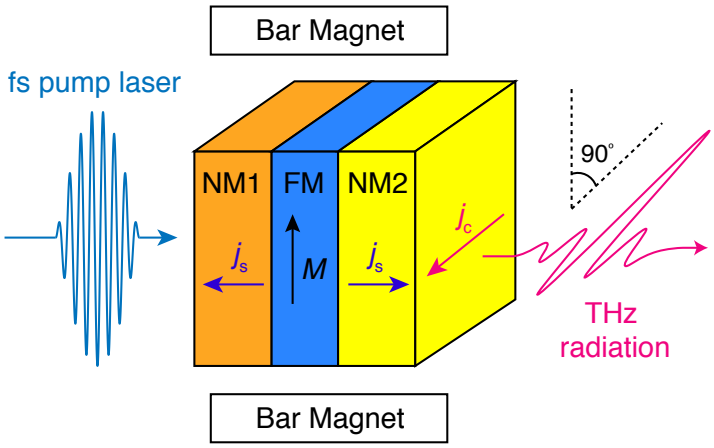

Figure 3.3: Schematic of STE and inverse spin Hall effect. M represents the direction of the applied magnetic field, j_s represents the spin current direction which is driven by the femtosecond laser pulse into the NM layers. j_c is the electric current arising from inverse spin Hall effect. The resulting THz radiation is polarized in the direction of j_c (perpendicular to M) and propagating in the same direction as the femtosecond pump laser.

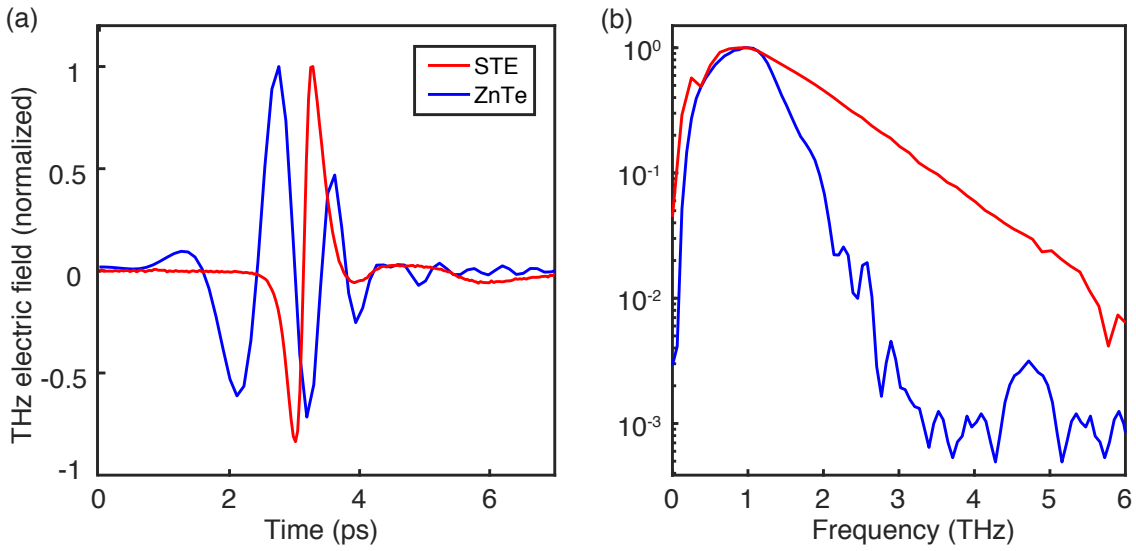

Figure 3.4: Comparison of THz emission from STE (red curves) and ZnTe (blue curves). (a) Normalized THz electrical field generated by STE and ZnTe. (b) THz spectra converted from the time domain via Fourier transform.

However, in some circumstances, it is hard to implement the STE. Specifically, in the magneto-THz spectroscopy used in this thesis, since a strong external magnetic field is applied to perform the cyclotron resonance measurement, the THz radiation generated by the STE can be hugely affected, making the emitted THz signal unreliable. Instead, a 2 mm-thick (110) ZnTe crystal is used for generating THz radiation based on the optical rectification effect. In this THz-generation process, the crystal has to have a large second-order nonlinear susceptibility, implying the lack of inversion symmetry. As a consequence, difference frequency generation is the dominant process under the illumination of a high-power laser pulse. The resulting radiation frequency $\omega_1 - \omega_2$ is in the THz frequency range [114]. The frequencies ω_1 and ω_2 can be any two frequency components of the ultrafast (35 fs) incident laser beam whose central wavelength is at 800 nm. One shortcoming of optical rectification, however, is that the THz bandwidth is narrower than that generated by the STE, which places a limit on the range of observable cyclotron resonance frequencies.

Apart from those two mechanisms, there are some other techniques to generate THz radiation [115], such as generation by photoconductivity and air plasma generation, which are outside the scope of this thesis.

3.1.1.2 Electro-Optic Sampling

To detect the generated THz signal, electro-optic sampling (EOS) technique is applied to measure the THz electric field as a function of time. In the THz spectroscopy setup, a 0.2 mm-thick (110) ZnTe crystal is used as the detection crystal, after which the gate beam passes through a quarter-wave plate and a Wollaston prism. The gate beam is then split into horizontally and vertically polarized laser beams and detected by a pair of balanced photodiodes. In the absence of THz pulse, the gate beam is tuned to be circularly polarized by rotating the quarter-wave plate. When the THz pulse is incident onto the ZnTe detection crystal, due to birefringent effect, a difference in

the amplitude between the horizontally and vertically polarized components of the gate beam is induced. This gives rise to a non-zero voltage measured by the pair of photodiodes, which is denoted as ΔPD and proportional to the THz electric field,

$$\Delta\text{PD} \propto \Delta\phi_{\text{gate}} \propto E_{\text{THz},x}, \tag{3.1}$$

where $\Delta\phi_{\text{gate}}$ is the phase change of the gate beam induced by the THz pulse when propagating through the detection crystal. Here, the THz pulse generated by the STE is approximately polarized along x-direction, therefore, the phase change is proportional to the x-component of the THz electric field $E_{\text{THz},x}$. By measuring the change of photodiode voltage ΔPD, the profile of the THz electric field can be recovered in the time domain. Furthermore, upon Fourier transform, the THz pulse measured in the time domain is converted to a THz spectrum in the frequency domain.

Using EOS, the electric field strength of the THz pulse can also be measured. Since the THz pulse is polarized along the x-direction and propagates in the z-direction, the birefringence of the ZnTe detection crystal is expressed as [116]

$$n_{x'} - n_{y'} = \frac{1}{2} n_o^3 r_{41} E_{\text{THz},x} \tan\theta, \tag{3.2}$$

where $n_o = 2.85$ is the ordinary index of ZnTe at 800 nm and $r_{41} = 4 \times 10^{-12}\,\text{mV}^{-1}$ is the electro-optic coefficient of ZnTe associated with $E_{\text{THz},x}$. θ is the angle between the old coordinate xy and the new coordinate $x'y'$ after phase modulation due to the presence of $E_{\text{THz},x}$, which is illustrated in Figure 3.5. $n_{x'}$ and $n_{y'}$ are the refractive indices of the ZnTe crystal along x'- and y'-directions respectively.

In the ZnTe crystal, since $n_o = n_e$ where n_e is the extraordinary index of ZnTe, $\theta = \pi/4$ and the phase change is expressed as [116]

$$\Delta\phi_{\text{gate}} = \frac{\pi d}{\lambda} n_o^3 r_{41} E_{\text{THz},x}, \tag{3.3}$$

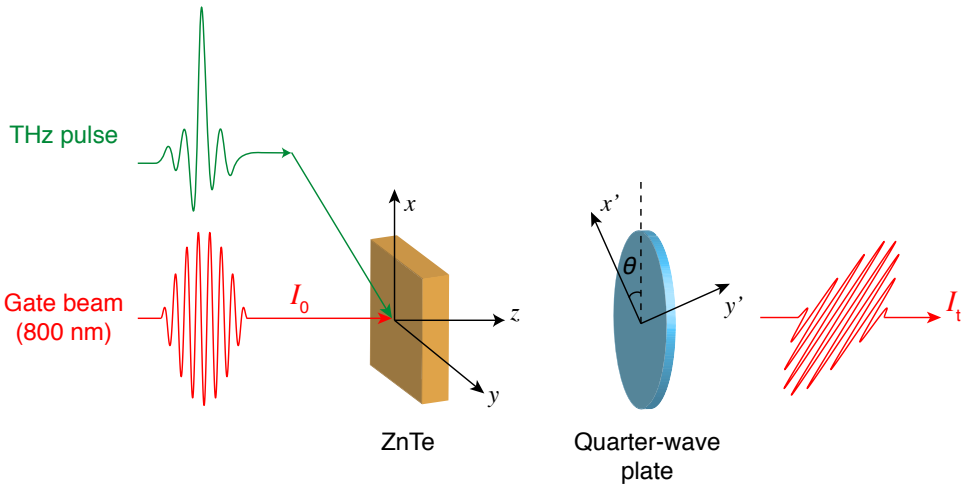

Figure 3.5: Illustration of the electro-optic amplitude modulation. The phase change of the gate beam $\Delta\phi_{\text{gate}}$ arises from the combination of the ZnTe crystal and the quarter-wave plate.

where $d = 1\,\text{mm}$ is the thickness of the ZnTe crystal and $\lambda = 800\,\text{nm}$. Under the combination of one ZnTe crystal and one quarter-wave plate, the intensity of the transmitted gate beam, I_t, is modulated according to

$$\frac{I_\text{t}}{I_0} = \frac{1}{2}[1 + \sin(\Delta\phi_{\text{gate}})], \tag{3.4}$$

where I_0 is the initial intensity of the gate beam without the THz modulation. Since $\Delta\phi_{\text{gate},x} \ll 1$, Equation (3.4) can be simplified to

$$\frac{I_\text{t}}{I_0} \approx \frac{1}{2}(1 + \Delta\phi_{\text{gate}}). \tag{3.5}$$

Experimentally, the change of transmissivity ΔI_t can be measured as the change in voltage detected by the photodiodes,

$$\frac{\Delta I_\text{t}}{I_0} = \frac{I_{\text{t}1} - I_{\text{t}0}}{I_0} = \frac{\Delta V}{V_{\text{max}}}, \tag{3.6}$$

where $I_{\text{t}1}$ and $I_{\text{t}0}$ represent the intensity of transmitted gate beam with and without

THz modulation, respectively. ΔV is the difference in voltage between the two photodiodes due to the THz modulation and $V_{\max}$ is the voltage detected by one of the photodiodes when there is no THz modulation. Combining Equations (3.3)–(3.6), the value of $E_{\mathrm{THz},x}$ is extracted according to

$$E_{\mathrm{THz},x} = \frac{2\lambda}{\pi d n_o^3 r_{41}} \frac{\Delta V}{V_{\max}}. \tag{3.7}$$

EOS can be further utilized to perform polarization-resolved measurement, which measures the THz signal in horizontal and vertical polarizations separately. In theory, this can be done by rotating the (110) ZnTe crystal by 90° to maximize the THz signal in the x- and y-directions, respectively. However, in practice, since the detection efficiency of THz also depends on the angle between the THz beam and the gate beam [117], it will require rotating the gate beam polarization correspondingly. In addition, rotating the detection crystal may also cause the THz beam and the gate beam to focus at slightly different spots. Hence, it is critical to have precise alignment to avoid such change of focusing position. Because of those complications, van der Valk *et al.* suggested another EOS scheme which utilizes an optically isotropic crystal for detection [118, 119]. In the magneto-THz spectroscopy, this technique is implemented to resolve the transmitted THz signal in orthogonal polarizations by using a (111) ZnTe crystal, which has similar detection efficiency in the $\langle\bar{2}11\rangle$ and $\langle 0\bar{1}1\rangle$ directions. A more detailed description of this polarization-resolved EOS technique is given in the following section (Section 3.1.2).

3.1.2 Polarization-Resolved Magneto-THz Spectroscopy

The previous sections are mainly about the applications of THz-TDS and OPTPS for investigating the materials' optoelectronic properties in the absence of external magnetic field, in which case the polarization of the transmitted/reflected THz pulse remains unchanged. This section will be focusing on the technique of magneto-THz spectroscopy where an external magnetic field is applied.

Under the effect of a magnetic field, the polarization of the transmitted THz pulse can be rotated by a certain angle, which is known as the Faraday effect [120]. A similar effect can also be observed in reflection mode, which is called the Kerr effect [121,122]. Since the incident THz pulse can be regarded as a superposition of right-handed and left-handed circularly polarized light, when there is a magnetic field applied to the surface of the conductive sample, the photo-excited charge carriers will move in a circular orbit, which subsequently changes the refractive indices for the right-handed and left-handed circularly polarized components. Due to this birefringent effect, a phase difference between those two circular polarizations will be induced, as well as a change in absorption coefficients. As a result, the linearly polarized incident THz pulse becomes elliptically polarized after transmission.

Utilizing the polarization-resolved EOS technique reported in Ref. 119, the orthogonal polarization components of the THz pulse can be separated, from which the effect of magnetic field on charge carriers can be investigated in more depth. For instance, the polarization-resolved magneto-THz spectroscopy can help to distinguish between photo-excited electrons and holes in the cyclotron resonance measurement according to the handedness of the transmitted THz pulse.

Figure 3.6 illustrates the experimental setup of the magneto-THz spectroscopy in transmission mode. Similar to the THz setup shown in Figure 3.1, another OPTPS setup is built in transmission mode around a superconducting magnet (Oxford Instruments, Spectromag) which can generate a magnetic field up to 7 T. The magnetic

fieled is generated by a superconducting coil with ultra-high electric current. The pump beam in this setup is brought up to a higher level using a periscope according to the configuration of the superconducting magnet. Here, a (110) ZnTe crystal is used for generating THz radiation. The transmitted THz pulse is detected using EOS with a (111) ZnTe crystal which is an isotropic crystal so that the linear polarizations of the THz light can be resolved in x- and y-directions without the need to rotate the crystal. In addition, the quarter-wave plate is moved to the front of the (111) ZnTe crystal and a half-wave plate is placed before the Wollaston prism.

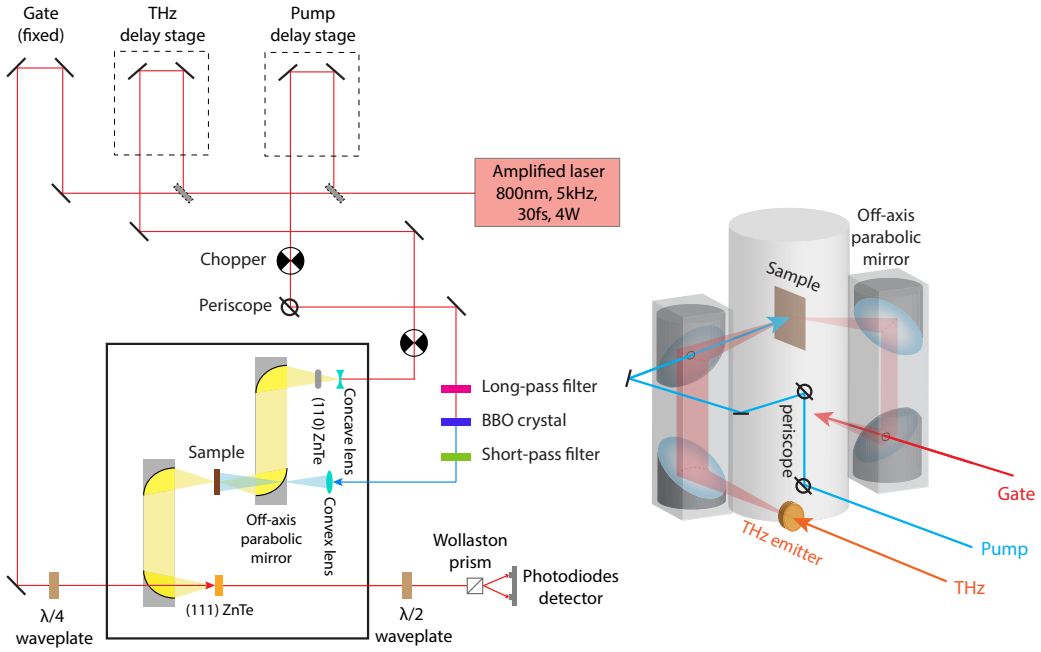

Figure 3.6: A schematic of the polarization-resolved magneto-THz spectroscopy. The THz pulse is generated by a (110) ZnTe crystal and detected by a (111) ZnTe crystal via EOS. The pump beam is brought to a higher level by a periscope due to the configuration of the superconducting magnet, which is illustrated by the cartoon on the right-hand side.

The detection mechanism of this polarization-resolved THz spectroscopy is slightly more complicated than that used in the normal THz-TDS. The voltage difference

ΔPD given in Equation (3.1) is modified to [118, 119]

$$\Delta\text{PD} \propto E_{\bar{2}11}\sin(2\psi - 4\delta) + E_{0\bar{1}1}\cos(2\psi - 4\delta), \tag{3.8}$$

where $E_{\bar{2}11}$ and $E_{0\bar{1}1}$ represent the THz electric field along the $\langle\bar{2}11\rangle$ and $\langle 0\bar{1}1\rangle$ axes of the (111) ZnTe crystal, respectively. ψ is the angle between the quarter-wave plate and the $\langle 0\bar{1}1\rangle$ axis, whereas δ is the angle between the quarter-wave plate and the half-wave plate. The quarter-wave plate is used for selecting a certain linear polarization component of the THz pulse to align with either $\langle\bar{2}11\rangle$ or $\langle 0\bar{1}1\rangle$ axis, and the half-wave plate is rotated correspondingly to measure that selected polarization component. This combinational use of a quarter-wave plate and a half-wave plate is advantageous as the orthogonal polarizations can be measured without the need of rotating the ZnTe crystal or the Wollaston prism. The use of (111) ZnTe crystal gives equal sensitivity in measuring $E_{\text{THz},x}$ and $E_{\text{THz},y}$ but at the cost of a slight decrease in signal strength [119].

Moreover, a recent study of THz detectors based on cross-nanowire networks has shown that the polarization states of THz electric field can be measured simultaneously without cross-talk [123]. This provides an alternative way of performing polarization-resolved magneto-THz spectroscopy measurements.

Magneto-THz spectroscopy may be used to perform cyclotron resonance measurements, from which the effective mass of charge carriers can be extracted according to Equation (2.25). Utilizing the polarization-resolved technique, the electrons and holes can be measured simultaneously even if their cyclotron resonance frequencies may lie in the same THz detection range.

3.1.3 Data Analysis of THz Spectroscopy

THz spectroscopy is a useful tool to extract some important optoelectronic parameters of semiconductor materials, such as charge-carrier mobility, carrier lifetimes and diffusion lengths. In this section, detailed description of the data analysis used in THz spectroscopy will be given, including the derivation of charge-carrier mobility and extraction of conductivity and reflectivity.

3.1.3.1 Charge-Carrier Mobility

The electrical mobility of charge carriers can be extracted from the transient absorption spectrum measured by OPTPS, which is commonly represented by the the change of THz transmission due to photo-excitation. Conventionally, the change of the amplitude of transmitted THz pulse, $\Delta T/T$, is defined as

$$\frac{\Delta T}{T} \equiv \frac{E_{\mathrm{on}} - E_{\mathrm{off}}}{E_{\mathrm{off}}} = \frac{\Delta E_{\mathrm{t}}}{E_{\mathrm{t}}}, \tag{3.9}$$

where the subscripts "on" and "off" stand for the photo-excitation and non-photo-excitation scenarios respectively. The subscript "t" stands for the transmission measurement, which will be replaced with "r" in the reflection measurement. The photo-induced electric field change, ΔE, satisfies the wave equation,

$$\frac{d^2 \Delta E(z)}{dz^2} + k^2 \Delta E(z) = -ik_0 Z_0 \Delta\sigma(z) E(z), \tag{3.10}$$

where $k_0 = \omega/c$ is the wave number of the THz field in vacuum and $k = n_{\mathrm{s}} k_0$ is the wave number inside the sample, with n_{s} denoting the refractive index of the sample at THz frequencies. In the case of $MAPbI_3$, $n_{\mathrm{s}} = \sqrt{\varepsilon_{\mathrm{stat}}} = \sqrt{30}$ which is an average of previously reported values measured in the THz-GHz frequency range [124–126]. $Z_0 = \varepsilon_0^{-1} c^{-1}$ is the vacuum wave impedance and $\Delta\sigma(z)$ is the photoconductivity of

the sample which varies with the depth z following the Beer-Lambert law,

$$\Delta\sigma(z) = \Delta\sigma_{\mathrm{s}} \exp(-i\alpha z), \tag{3.11}$$

where $\Delta\sigma_{\mathrm{s}} = \Delta\sigma(0)$ is the photoconductivity at the front surface of the sample and α is the absorption coefficient of the sample at the photo-excitation wavelength, which can be measured by FTIR. By combining Equations (3.10) and (3.11), the general solution can be expressed in terms of the electrical mobility μ as [127]

$$\begin{aligned}\mu = \frac{n_1 + n_2}{2n_{\mathrm{s}}} \frac{a}{e\Phi_{\mathrm{eff}}} \Bigg[& (1 + r_1 r_2 \exp(2ikL)) \int_0^L \Delta\sigma(z) dz \\ & + r_1 \int_0^L \exp(2ikz)\Delta\sigma(z) dz + r_2 \exp(2ikL) \int_0^L \exp(-2ikz)\Delta\sigma(z) dz \Bigg],\end{aligned} \tag{3.12}$$

where L is the thickness of the sample, n_1 and n_2 are refractive indices of the medium surrounding the sample. In the case of the $MAPbI_3$ thin film sample which is deposited on a quartz substrate, $n_1 = 1$ and $n_2 = 2.13$ [128] for air and quartz respectively. $r_1 = (n_{\mathrm{s}} - n_1)/(n_{\mathrm{s}} + n_1)$ and $r_2 = (n_{\mathrm{s}} - n_2)/(n_{\mathrm{s}} + n_2)$ are the reflection coefficients at the front and back surfaces of the thin film, respectively and $a = [1 - r_1 r_2 \exp(2ikL)]^{-1}$ describes the multiple internal reflections due to Fabry-Perot effect. The effective photon fluence Φ_{eff} is defined as

$$\Phi_{\mathrm{eff}} = \frac{N}{A_{\mathrm{eff}}}, \tag{3.13}$$

where A_{eff} is the effective area between the pump beam and the THz beam which will be defined later. N is the number of charge carriers induced by the pump beam,

$$N = \varphi \frac{\mathcal{E}\lambda}{hc}(1 - R_{\mathrm{pump}})(1 - T_{\mathrm{pump}}), \tag{3.14}$$

with $\mathcal{E}$ being the energy of a pump pulse at wavelength $\lambda = 400\,\text{nm}$. R_{pump} and T_{pump} are the reflectivity and transmissivity of the sample measured at 400 nm using FTIR respectively. $\varphi \leq 1$ is the ratio of free charge-carriers created per photon absorbed, which in the case of $MAPbI_3$ is approximated as unity.

Different from the absolute pump photon fluence which is purely determined by the pump beam, the effective photon fluence, Φ_{eff}, which takes into account the conversion ratio between absorbed photons and induced charge carriers, is also related to the photoconductive part of the sample. This is determined by the overlapping area between the pump beam and the THz beam. Mathematically, Φ_{eff} is calculated as the photo-induced charge density weighted by the THz electric field strength at each pump beam spatial position. Therefore, to calculate this effective "absorption intensity", the following weighting function is used,

$$\frac{N}{A_{\text{eff}}} = \int_0^{2\pi} \int_0^{\infty} \hat{n}_{\text{pump}} g_{\text{THz}} r dr d\theta, \tag{3.15}$$

where $\hat{n}_{\text{pump}}$ is the 2D areal charge density induced by the pump beam, which is proportional to the photon density of a pump pulse by a factor of φ, and g_{THz} is the normalized THz areal spread function. r and θ represent the radial distance and the azimuthal angle in the spherical coordinate system respectively. It is assumed that both $\hat{n}_{\text{pump}}$ and g_{THz} follow a 2D Gaussian distribution function,

$$\hat{n}_{\text{pump}}(r) = \frac{N}{2\pi\sigma_{\text{pump}}^2} \exp\left(-\frac{r^2}{2\sigma_{\text{pump}}^2}\right), \tag{3.16}$$

$$g_{\text{THz}}(r) = \frac{1}{2\pi\sigma_{\text{THz}}^2} \exp\left(-\frac{r^2}{2\sigma_{\text{THz}}^2}\right), \tag{3.17}$$

where σ_{pump} and σ_{THz} are the beam waists of the pump beam and the THz beam, respectively. It can be easily checked that $\int_0^{2\pi} \int_0^{\infty} \hat{n}_{\text{pump}} r dr d\theta = N$ and $\int_0^{2\pi} \int_0^{\infty} g_{\text{THz}} r dr d\theta = 1$. As demonstrated in Figure 3.7, $\hat{n}_{\text{pump}}$ and g_{THz} are

represented by the blue and red curves respectively. The beam waists, σ_{pump} and σ_{THz}, are related to the full width at half maximum (FWHM) according to

$$\sigma_{\text{pump,THz}} = \frac{\text{FWHM}_{\text{pump,THz}}}{2\sqrt{2\ln 2}}. \tag{3.18}$$

Combining Equations (3.15)–(3.17), the expression for the effective area A_{eff} is obtained,

$$A_{\text{eff}} = 2\pi(\sigma^2_{\text{pump}} + \sigma^2_{\text{THz}}). \tag{3.19}$$

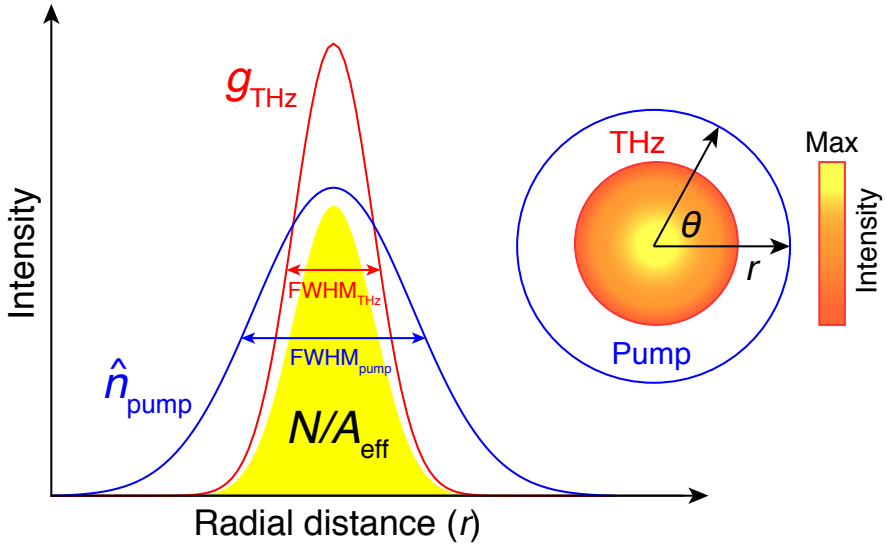

Figure 3.7: 2D Gaussian distributions of the photo-excited charge density, $\hat{n}_{\text{pump}}$, and the normalized THz intensity distribution, g_{THz}, which are represented by the blue and red curves, respectively. The yellow area represents the effective charge-carrier density within the overlapping area between the pump and THz beams, which is the integral shown in Equation (3.15).

According to the thin-film approximation (TFA) where the thickness of the photo-excited layer of the sample, $d = 1/\alpha$, is much smaller than the smallest wavelength in the THz pulse, i.e. $2\omega_{\text{THz}} nd \ll 1$ [129], the unexcited part of the $MAPbI_3$ thin film can be assumed to be the same as the quartz substrate. Therefore, assuming $n_s \approx n_2$

and $r_2 \approx 0$, Equation (3.12) is simplified to

$$\mu = \frac{\Delta S A_{\text{eff}}}{Ne}, \tag{3.20}$$

where ΔS is the sheet conductivity that can be expressed in terms of the change of THz signal $\Delta T/T$,

$$\Delta S = -\varepsilon_0 c(n_1 + n_2)\left(\frac{\Delta T}{T}\right), \tag{3.21}$$

which leads to the final expression for the effective mobility in transmission,

$$\varphi\mu_{\text{T}} = -\varepsilon_0 c(n_1 + n_2)\frac{A_{\text{eff}} hc}{\mathcal{E} e\lambda(1 - R_{\text{pump}})(1 - T_{\text{pump}})}\left(\frac{\Delta T_{\text{pp}}}{T_{\text{pp}}}\right), \tag{3.22}$$

where ε_0 is the permittivity of free space, c is the speed of light and h is the Planck constant. It should be noted that Equation (3.22) is only valid for materials with a flat photoconductivity spectrum (i.e. a short charge-carrier scattering time) such as $MAPbI_3$, which makes it sufficient to probe the charge-carrier decay dynamics at the peak of the THz pulse [130]. Moreover, this expression is slightly different from the conventional one which measures both ΔT and T at the THz pulse peak (T_{peak}) and uses $(\Delta T/T)_{T\text{peak}}$ for calculating the mobility [36–38]. Here the ratio of the peak-to-peak values between ΔT and T is used instead, which is denoted as $\Delta T_{\text{pp}}/T_{\text{pp}}$. This is because as shown in Figure 3.8(a), the peaks of T and ΔT do not overlap exactly with each other, which means if $\Delta T/T$ is taken at T_{peak}, the mobility will be underestimated. Figure 3.8(b) shows the mobility values calculated from $\Delta T_{\text{pp}}/T_{\text{pp}}$ and $(\Delta T/T)_{T\text{peak}}$ to demonstrate that $(\Delta T/T)_{T\text{peak}}$, which doesn't take into account the shift between ΔT and T peaks, underestimates the mobility by 25–40%. Compared with previous mobility measurement taken by Milot *et al.* using $(\Delta T/T)_{T\text{peak}}$ (blue dots) [38], the mobility values measured in this thesis and calculated in the same way using $(\Delta T/T)_{T\text{peak}}$ (green circles) is lower, which is consistent with the fact that the

$MAPbI_3$ film measured in this thesis has a smaller grain size (580 nm) than the other sample (1 μm) used in Ref. 38.

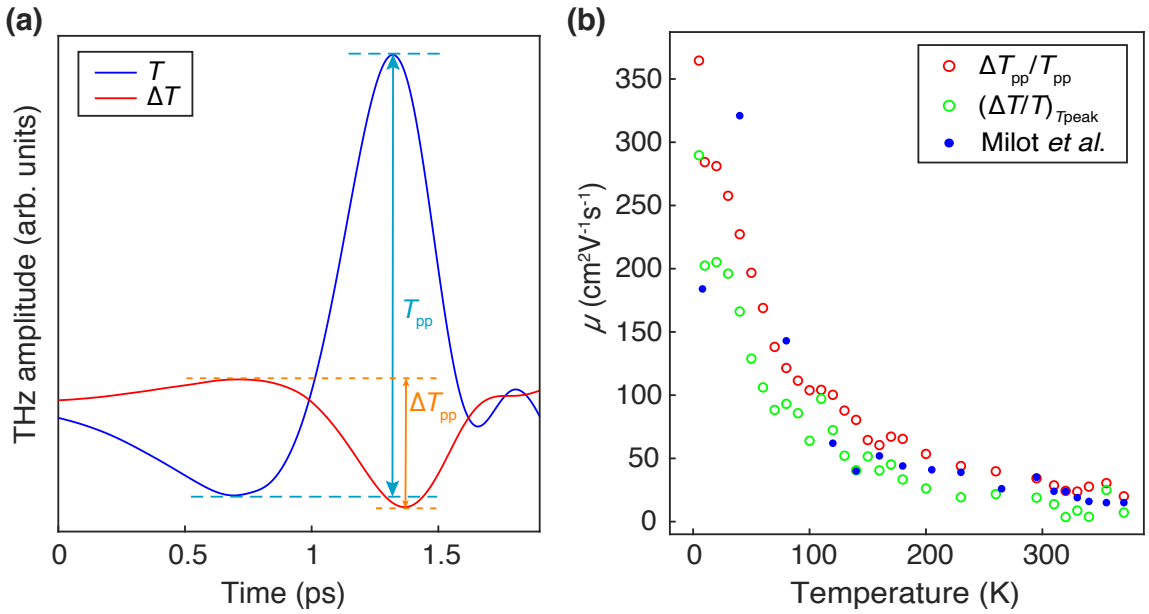

Figure 3.8: (a) Time-domain traces of T and ΔT of the $MAPbI_3$ thin film measured at 5 K, where the blue and red curves represent T and ΔT, respectively. ΔT has been scaled up by a factor of 10 to show the shift between T and ΔT peaks more clearly. (b) Comparison of mobility values calculated using $\Delta T_{pp}/T_{pp}$ and $(\Delta T/T)_{T\text{peak}}$, which are represented by the red and green circles, respectively. The blue dots represent the previously reported mobility values of another $MAPbI_3$ thin film sample [38].

Mobility in Reflection

In the case of reflection, the $\Delta T/T$ in Equation (3.9) is replaced by the reflected THz signal $\Delta R/R$,

$$\frac{\Delta R}{R} \equiv \frac{E_{\text{on}} - E_{\text{off}}}{E_{\text{off}}} = \frac{\Delta E_{\text{r}}}{E_{\text{r}}}. \tag{3.23}$$

The solution to Equation (3.10) is then modified to [131]

$$\begin{aligned}\Delta E_{\text{r}} = -\frac{Z_0 t_1^2 a^2}{2n_1}\Bigg[&\int_0^L \exp(2ikz)\Delta\sigma(z)dz \\ &+ 2r_2\exp(2ikL)\int_0^L \Delta\sigma(z)dz + [r_2\exp(2ikL)]^2\int_0^L \exp(-2ikz)\Delta\sigma(z)dz\Bigg],\end{aligned} \tag{3.24}$$

where $t_1 = 2n_1/(n_{\text{s}} + n_1)$ is the transmission coefficient at the front sample surface. Assuming the incident field E_{inc} is unity, the reflected field E_{r} is given by

$$E_{\text{r}} = 1 - t_1 = \frac{n_1 - n_{\text{s}}}{n_1 + n_{\text{s}}}. \tag{3.25}$$

Combining Equations (3.23)–(3.25) with the application of the Beer-Lambert law, the sheet photoconductivity measured in reflection can be expressed as [129, 131]

$$\Delta S = \frac{\varepsilon_0 c(n_{\text{s}}^2 - n_1^2)}{2a}\left(1 - \frac{2\omega n_{\text{s}}}{\alpha c}i\right)\left(\frac{\Delta R}{R}\right). \tag{3.26}$$

The photoconductivity in reflection is then given by

$$\Delta\sigma(\omega) = \alpha\Delta S = \frac{\varepsilon_0 c\alpha(n_{\text{s}}^2 - n_1^2)}{2a}\left(1 - \frac{2\omega n_{\text{s}}}{\alpha c}i\right)\left(\frac{\Delta R}{R}\right). \tag{3.27}$$

Under the condition of TFA where the second term vanishes, $\Delta\sigma$ becomes linearly proportional to $\Delta R/R$ and the mobility can be expressed as

$$\mu_R = \frac{\varepsilon_0 c(n_{\text{s}}^2 - n_1^2)}{2a}\frac{A_{\text{eff}}}{eN}\left(\frac{\Delta R_{\text{pp}}}{R_{\text{pp}}}\right), \tag{3.28}$$

This equation also applies to the $MAPbI_3$ single crystal, since its photo-excited layer is still thinner than the THz wavelength to satisfy the TFA condition. As illustrated in Figure 3.9(b), since a sapphire substrate is inserted in front of the single crystal to improve the thermal contact, there will be some reflection loss of the pump beam at the air-sapphire and sapphire-crystal interfaces. As a result, the actual intensity of the pump beam at the single crystal surface, I'_{pump}, is less than the initial intensity I_{pump}, which reduces the number of charge carriers given by Equation (3.14),

$$N = f\varphi\frac{\mathcal{E}\lambda}{hc}(1 - R_{\text{pump}})(1 - T_{\text{pump}}), \tag{3.29}$$

where $f < 1$ is the power transmission coefficient which can be calculated according to the Fresnel equation. In the configuration shown in Figure 3.9(b), $f \approx 0.68$.

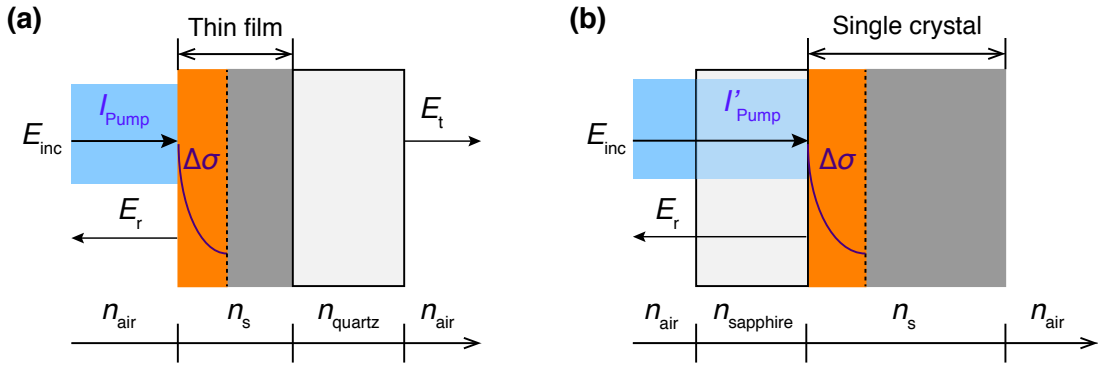

Figure 3.9: Diagrams of the transmission and reflection of THz pulse from (a) a $MAPbI_3$ thin film and (b) a $MAPbI_3$ single crystal. The orange area represents the photo-excited part within the sample where the photoconductivity $\Delta\sigma(z)$ follows the Beer-Lambert law given by Equation (3.11). The grey area represents the rest of the sample which is not photo-excited under the assumption of the TFA. E_{inc}, E_{t} and E_{r} represent the incident, transmitted and reflected THz electric field, respectively. E_{t} in the single crystal is negligible due to the strong absorption of THz signal in the thick crystal. The blue shade represents the pump beam, which undergoes reflection loss in the case of single crystal because of the sapphire substrate at the front.

Finally, the effective mobility measured in reflection is expressed as

$$\varphi\mu_R = \frac{1}{f}\frac{\varepsilon_0 c(n_s^2 - n_1^2)}{2a}\frac{A_{\text{eff}}hc}{\mathcal{E}e\lambda(1-R_{\text{pump}})(1-T_{\text{pump}})}\left(\frac{\Delta R_{\text{pp}}}{R_{\text{pp}}}\right), \tag{3.30}$$

which is only valid for materials with a flat photoconductivity spectrum. $n_1 = n_{\text{air}}$ and $f = 1$ for the $MAPbI_3$ thin film on quartz and $n_1 = n_{\text{sapphire}}$ for the single crystal with a sapphire disc at the front. Previous discussion has shown that the shift between T and ΔT peaks requires using $\Delta T_{\text{pp}}/T_{\text{pp}}$ instead of $(\Delta T/T)_{T\text{peak}}$ to calculate the mobility. When it comes to the mobility in reflection measurement, the same principle applies, since both $MAPbI_3$ thin films and single crystals show a shift between R and ΔR peaks as illustrated in Figure 3.10.

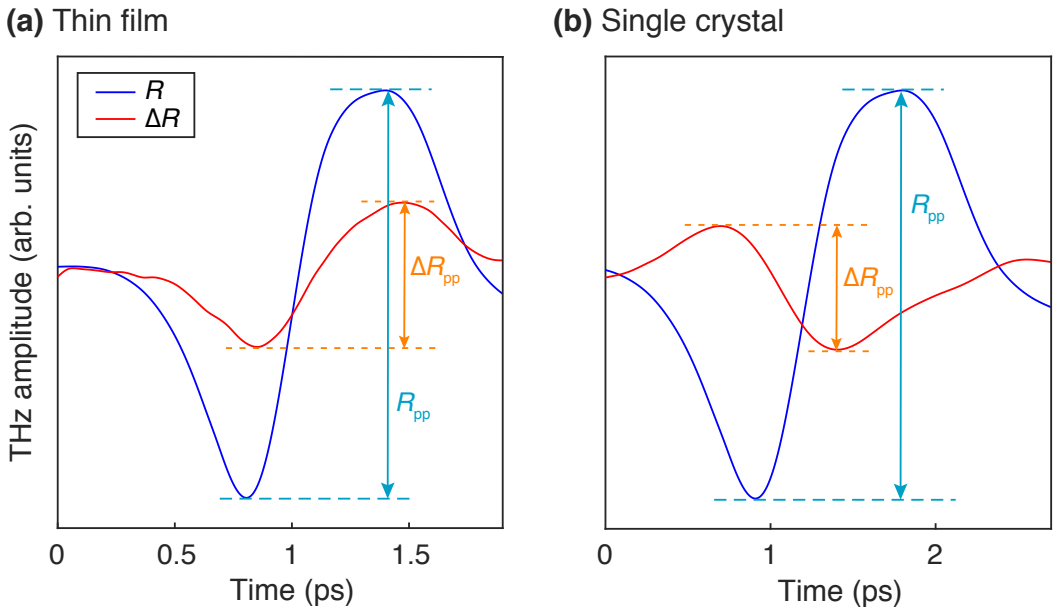

Figure 3.10: Time-domain traces of R and ΔR of (a) a $MAPbI_3$ thin film measured at 5 K and (b) a $MAPbI_3$ single crystal measured at 75 K. The blue and red curves represent the reflected THz signal (R) and the change in THz (ΔR), respectively. ΔR has been scaled up by a factor of 40 to show the shift more clearly.

While the shift in the thin film is small enough that the mobility calculated using $(\Delta R/R)_{R\text{peak}}$ might not deviate so much from the exact value, the much larger shift in the single crystal makes it critical to use $\Delta R_{\text{pp}}/R_{\text{pp}}$ to extract the mobility value.

On top of that, by measuring the traces of THz pulse and change of THz in the time domain, the noise that comes from the fluctuation of the THz peak is reduced, which gives a better SNR.

Figure 3.11(a) compares the mobility value of the $MAPbI_3$ thin film measured in reflection using $\Delta R_{pp}/R_{pp}$ and $(\Delta R/R)_{R\text{peak}}$, which again shows that the new way of extracting mobility overcomes the issue with the shift between R and ΔR. The less scattered data points of $\Delta R_{pp}/R_{pp}$ (red triangles) also indicate a better SNR. More importantly, in the case of the $MAPbI_3$ single crystal, the mobility measured in reflection using $\Delta R_{pp}/R_{pp}$ is significantly improved, as shown in Figure 3.11(b). Moreover, it is observed that ΔR also shifts with temperature, which makes $(\Delta R/R)_{R\text{peak}}$ even less reliable and the temperature-dependence trend represented by the green triangles in Figure 3.11(b) less conclusive.

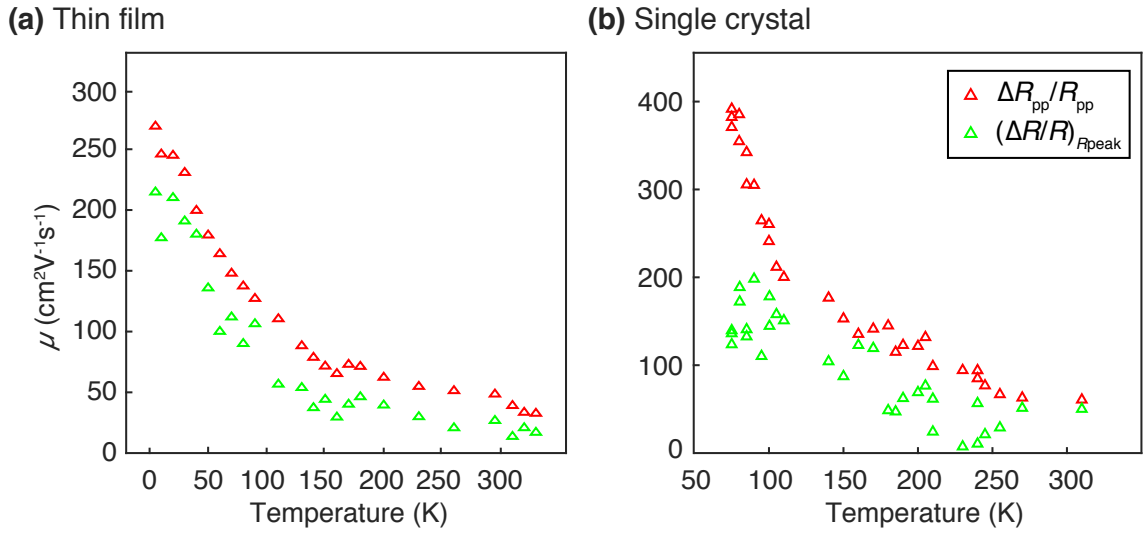

Figure 3.11: Reflection measurement of temperature-dependent mobility of $MAPbI_3$ (a) thin film and (b) single crystal. The red and green triangles represent the mobility values calculated using $\Delta R_{pp}/R_{pp}$ and $(\Delta R/R)_{R\text{peak}}$, respectively.

In Figure 3.12, the mobility of the $MAPbI_3$ thin film measured in transmission and reflection, which are calculated by Equations (3.22) and (3.30) respectively are plotted on top of each other for comparison. The consistency between the transmission and reflection measurements verifies the validity of the mobility measurement of the $MAPbI_3$ single crystal, which can only be done in the reflection mode.

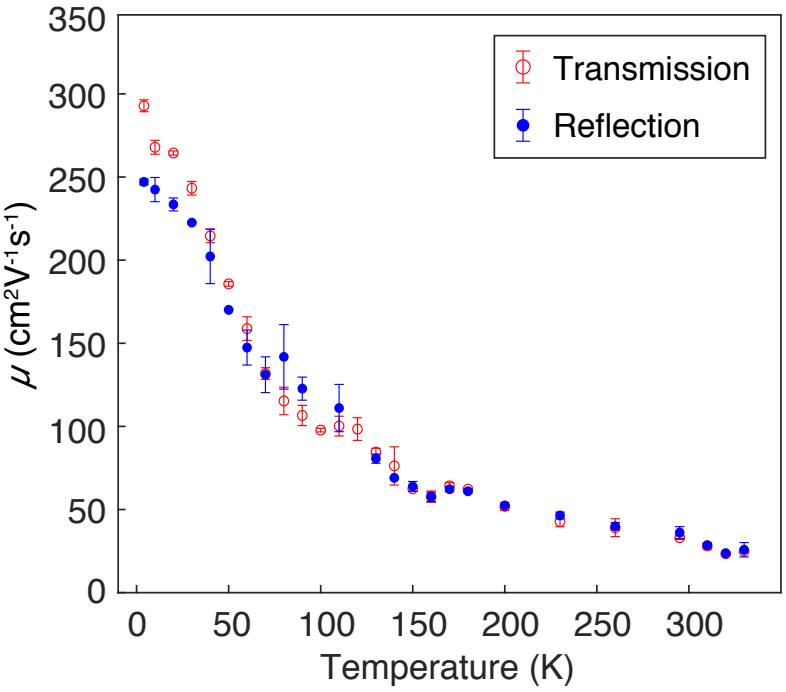

Figure 3.12: Comparison of mobility measurements of the $MAPbI_3$ thin film between transmission and reflection modes, which are represented by the red circles and blue dots respectively.

It should be noted that the calculation of mobility using Equations (3.22) and (3.30) needs to be performed within the low photo-excitation regime where $\Delta T/T$ (or $\Delta R/R$) changes linearly with fluence. As illustrated in Figure 3.13, when the fluence is below $40\,\mu\mathrm{J/cm^2}$, the peak of the transient absorption spectrum, $-\Delta T/T$, increases linearly with fluence and this is the range where the mobility is extracted. Above $40\,\mu\mathrm{J/cm^2}$, the photo-excitation peak starts to saturate and the mobility value extracted in this range will be an underestimation of the true mobility value.

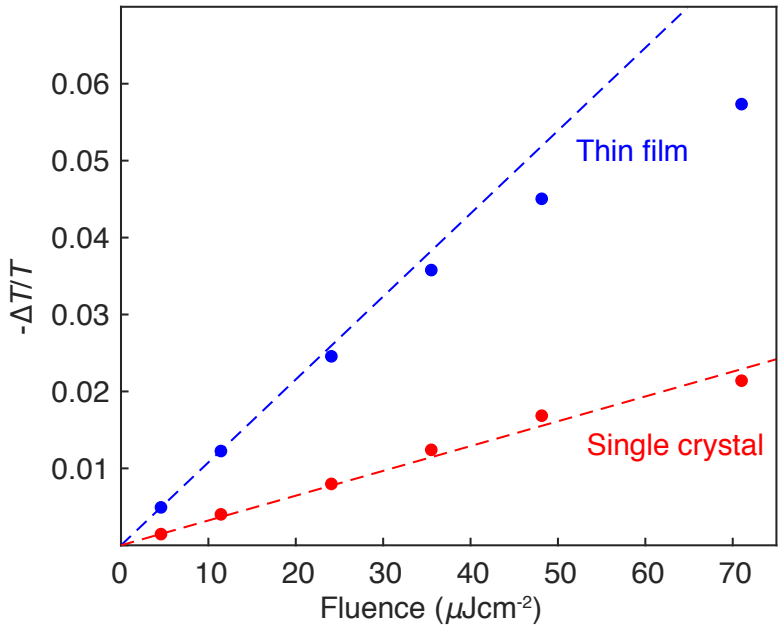

Figure 3.13: Peak of transient absorption spectrum, $-\Delta T/T$, measured at different fluences. The blue and red dots represent the experimental data of the $MAPbI_3$ thin film and single crystal, respectively. The blue and red dash lines represent the corresponding linear fit in the low-fluence regime, where the mobility value is extracted.

3.1.3.2 Conductivity of $MAPbI_3$ Thin Films

Apart from measuring electrical mobility, THz spectroscopy can also help to identify phonon modes of the sample by measuring its dark conductivity spectrum using THz-TDS where no photo-excitation is applied. The transmitted THz spectrum, $T(\omega)$, is used to express the dark conductivity spectrum $\sigma(\omega)$ as [132, 133]

$$\sigma(\omega) = \frac{\varepsilon_0 c(1+\tilde{n}_{\text{sub}})}{d}\left(\frac{1}{T(\omega)} - 1\right), \tag{3.31}$$

where $\tilde{n}_{\text{sub}}$ is the complex refractive index of the substrate, which in the case of the $MAPbI_3$ thin film sample is a z-cut quartz disc and hence $\tilde{n}_{\text{sub}} = 2.13$ [128]. The transmitted THz spectrum through the sample is corrected by $T(\omega) = T_{\text{sample}}(\omega)/T_{\text{reference}}(\omega)$ where $T_{\text{reference}}(\omega)$ is the transmitted THz spectrum through a bare quartz substrate. Figure 3.14 exemplifies a conductivity spectrum of a $MAPbI_3$ thin film sample measured at room temperature. The $MAPbI_3$ thin film shows two prominent phonon modes around 1 THz and 2 THz which are assigned to Pb–I stretching modes [89, 111].

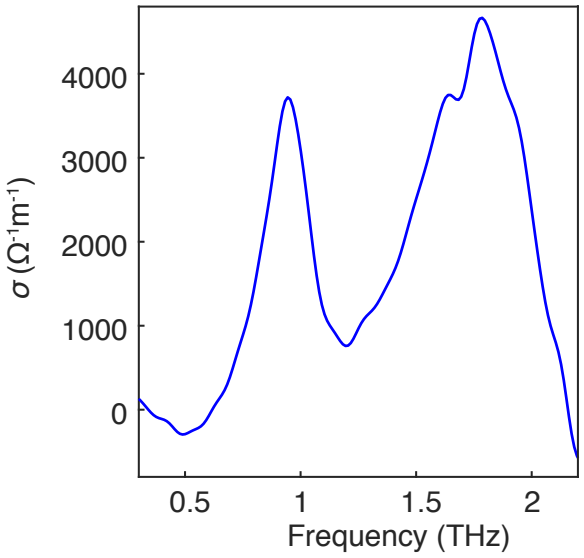

Figure 3.14: Transmitted THz spectra of $MAPbI_3$ thin film deposited on a quartz substrate measured at room temperature without photo-excitation.

Moreover, the complex dielectric function $\varepsilon(\omega) = \varepsilon_1(\omega) + i\varepsilon_2(\omega)$, which may be approximated by the Drude-Lorentz model [134],

$$\varepsilon(\omega) = \varepsilon_\infty + (\varepsilon_{\text{stat}} - \varepsilon_\infty)\frac{\omega_{\text{TO}}^2}{\omega_{\text{TO}}^2 - \omega^2 - i\gamma_{\text{TO}}\omega}, \tag{3.32}$$

can be extracted from the dark conductivity, according to the following equation,

$$\varepsilon(\omega) = \varepsilon_\infty + \frac{i}{\varepsilon_0\omega}\sigma(\omega), \tag{3.33}$$

where ε_∞ is the high-frequency dielectric constant of the sample and $\varepsilon_{\text{stat}}$ is the static (low-frequency) dielectric constant. ω_{TO} is the frequency of TO phonon mode and γ_{TO} is the phonon scattering rate. Combining Equations (3.32) and (3.33), the dielectric function $\varepsilon(\omega)$ can be fitted to the experimentally obtained conductivity spectrum $\sigma(\omega)$, from which $\varepsilon_{\text{stat}}$, ε_∞, ω_{TO} and γ_{TO} can be extracted. In the case of the $MAPbI_3$ perovskite, since multiple phonon modes exist in the THz frequency range [89, 111], Equation (3.32) needs to be modified with multiple Lorentzian oscillators,

$$\varepsilon(\omega) = \varepsilon_\infty + \sum_j^N \frac{\omega_{\text{TO},j}^2}{\omega_{\text{TO},j}^2 - \omega^2 - i\gamma_{\text{TO},j}\omega}. \tag{3.34}$$

On the other hand, when photo-excitation is introduced in OPTPS, the photo-induced charge carriers will reduce the transmission of THz, giving rise to a non-zero $\Delta T = T_{\text{on}} - T_{\text{off}}$ from which the photoconductivity $\Delta\sigma(\omega)$ is derived [135],

$$\Delta\sigma(\omega) = -\frac{\varepsilon_0 c(1+\tilde{n}_{\text{sub}})}{d}\left(\frac{\Delta T}{T_{\text{on}}}\right)\left(\frac{T_{\text{reference}}}{T_{\text{off}}}\right). \tag{3.35}$$

In the case of materials whose photo-induced ΔT is relatively small compared to T_{on}

and T_{off}, Equation (3.35) is often simplified as [36, 136]

$$\Delta\sigma(\omega) = -\frac{\varepsilon_0 c(1+\tilde{n}_{\text{sub}})}{d}\frac{\Delta T}{T_{\text{off}}}. \tag{3.36}$$

However, while Equation (3.36) makes it easier to extract photoconductivity without the need of measuring $T_{\text{reference}}(\omega)$, the neglect of the contribution of phonon modes observed in the dark conductivity spectrum may lead to inaccurate analysis of the photoconductivity. As reported by La-o-vorakiat *et al.* [135] "phonon modulations" observed in the photoconductivity spectrum of perovskite thin films can be removed by using Equation (3.35), which leads to a pure Drude response. In contrast, such "phonon modulations" were often attributed to the electron-phonon coupling effect in earlier studies [36]. Although such electron-phonon coupling effect has been observed in MHPs using other experimental techniques such as temperature-dependent PL spectroscopy [137], misinterpretation of the "phonon modulation" may result in overestimation of the effect of electron-phonon coupling. In order to analyze the phonon behavior properly, in this thesis, Equation (3.35) is used for extracting the photoconductivity spectrum of $MAPbI_3$ thin films.

3.1.3.3 Reflectivity of $MAPbI_3$ Single Crystals

When it comes to a single crystal sample, however, things are more complicated. As the crystal is too thick for THz radiation to transmit through, only the reflectivity spectrum can be measured via THz-TDS in the reflection mode. Therefore, instead of extracting dielectric function from the conductivity spectrum, the reflectivity spectrum, $R(\omega)$, is used for calculating the dielectric function and investigating the behavior of phonon modes in the single crystal. In the reflection THz spectroscopy setup, since the THz pulse is incident normally onto the sample surface,the relationship between the reflectivity $R(\omega)$ and the dielectric function $\varepsilon(\omega)$ is obtained

according to the Fresnel formula,

$$R(\omega) = \left| \frac{R_{\text{crystal}}(\omega)}{R_{\text{mirror}}(\omega)} \right|^2 = \left| \frac{1 - \sqrt{\varepsilon(\omega)}}{1 + \sqrt{\varepsilon(\omega)}} \right|^2, \tag{3.37}$$

where $R_{\text{crystal}}(\omega)$ represents the reflected THz electric field from the $MAPbI_3$ single crystal and $R_{\text{mirror}}(\omega)$ is the reflected THz field from a gold mirror which is used as a reference for calculating reflectivity. In addition, the Kramers-Kronig (KK) transformation is applied due to the dynamical coupling between the real part $\varepsilon_1(\omega)$ and the imaginary part $\varepsilon_2(\omega)$ of the dielectric function. Explicitly, this interdependent relationship is governed by the following equations [138, 139],

$$\varepsilon_1(\omega) = \frac{2}{\pi} \mathcal{P} \int_0^\infty \frac{x \varepsilon_2(x)}{x^2 - \omega^2} dx + 1, \tag{3.38}$$

$$\varepsilon_2(\omega) = -\frac{2\omega}{\pi} \mathcal{P} \int_0^\infty \frac{\varepsilon_1(x)}{x^2 - \omega^2} dx + \frac{4\pi\sigma_{\text{DC}}}{\omega}, \tag{3.39}$$

where σ_{DC} is the DC conductivity and $\mathcal{P}$ is the principal value integral. Combining Equations (3.37)–(3.39), the complex dielectric function can be extracted from the experimentally measured reflectivity spectrum.

Here, the method of variational dielectric functions (VDF) developed by Kuzmenko is utilized [140]. This method consists of two steps: (i) the technique of least square fitting is used for fitting the reflectivity spectrum $R(\omega)$ with as many Lorentzian oscillators as the number of data points, which composes the imaginary part of the dielectric function; (ii) the KK transformation is applied to restore the corresponding real part of the dielectric function. Consequently, the full spectral information of the material is obtained from this KK-constrained variational fitting method. This method has the ability to fit any reflectivity spectrum as long as enough Lorentzian oscillators are included, thanks to the completeness of Drude-Lorentz functions. In fact, any physical dielectric function can be approximated by

a sum of Lorentzian oscillators. Different from the conductivity analysis used for the thin film samples, the VDF method is a numerical method which extracts the dielectric function from the reflectivity spectrum without using any analytical expression. Therefore, there can be indefinitely many flexible parameters, depending on the number of Lorentzian oscillators that are used for fitting the reflectivity spectrum. A software called RefFIT [141] is designed based on those principles, which is used in this thesis for fitting optical spectra. According to the fitted reflectivity spectrum of the $MAPbI_3$ single crystal, the complex refractive index $\tilde{n}(\omega)$ can be obtained which is then used for calculating the absorption coefficient at THz frequencies [142],

$$\alpha(\omega) = \frac{4\pi\kappa(\omega)}{\lambda} = \frac{2\omega\kappa(\omega)}{c}, \tag{3.40}$$

where $\kappa(\omega)$ is the imaginary part of the refractive index $\tilde{n}(\omega) = n(\omega) + i\kappa(\omega)$. With the help of the VDF fitting technique, the reflectivity spectrum of the $MAPbI_3$ single crystal are converted to an absorption spectrum, from which the phonon modes can be identified.

Utilizing THz spectroscopy in transmission and reflection modes enables the key optoelectronic properties of MHPs to be investigated, such as charge-carrier mobilities, charge-carrier dynamics and phonon modes. The application of magneto-THz spectroscopy provides a pathway to measure the electron effective mass in narrow-gap semiconductors, from which the non-parabolicity of their band structures can be quantified.

Chapter 4

Limits to Electrical Mobility in $MAPbI_3$ Single Crystals and Polycrystalline Thin Films

4.1 Introduction

In the last decade, MHP semiconductors have emerged as promising materials for photovoltaic applications [143–146], owing to their ease of large-scale deposition and excellent optoelectronic properties, such as high charge-carrier mobility [36–38], long carrier diffusion length [34, 35, 147] and composition-tunable bandgap [11, 12]. To date the primary application of these materials has been photovoltaics. In particular, single-junction solar cells based on these materials have shown rapid growth in PCE from 3.8% to 25.2%, whereas perovskite-silicon tandem solar cells have reached efficiencies of over 29% [17, 143]. These cutting-edge photovoltaic devices have been exclusively developed on a platform of polycrystalline thin films. While such thin films can be deposited easily and have shown remarkable performance in solar cells, the question remains as to what the upper limit of performance might be for perfectly

crystalline thin-film devices, and whether this transition is required to further expand the applications of MHPs into high-performance electronic devices.

Two important figures of merit for quantifying the intrinsic electrical properties of a semiconductor are charge-carrier mobility and diffusion length. The electrical mobility μ, as defined earlier, is the drift velocity attained by a charge carrier per unit of applied electric field, while the diffusion length L_{D} is the average distance a charge carrier moves between generation and recombination. Despite many measurements of μ and L_{D} in MHPs, no universal agreement on values have been achieved even for the well-studied $MAPbI_3$. The discrepancies may in part be attributed to differences in the purity, stoichiometry and morphology of the samples. For example different fabrication routes of perovskites, such as the one-step spin-coating method with anti-solvent approach [148–151], air-blading technique [25], vapor-assisted deposition [152, 153], all-vacuum sequential deposition [154] and vacuum co-evaporation method [155], can lead to different types and concentrations of impurities as well as vastly different grain sizes within perovskite thin films [150, 153]. However significant discrepancies may also be traced back to different ways of measuring charge-carrier mobilities and lifetimes [156]. This chapter explains that since MHPs are highly luminescent the reabsorption of photons emitted from the sample can lead to a significant overestimate of L_{D} and that effect is particularly strong in measurements on single crystals. Here, the wide range of values for charge recombination parameters and charge diffusion lengths reported previously from MHP single crystals are reconciled, and so are the discrepancies between single crystals and polycrystalline thin films.

Conventionally, μ of a semiconductor is extracted from devices via the Hall effect [35, 157], space-charge limited current [23, 35, 147, 158], time of flight measurements [35] or field effect transistor characterisation [159, 160]. However the strong polarizability of MHPs owing to ion migration [161–163] and the complexity of making suitable contacts to MHPs can complicate the calculation of mobility from the

data acquired via these techniques. An alternative approach is to use a non-contact method to determine the intrinsic electrical mobility of a material, via techniques such as microwave conductivity [164–167] and THz spectroscopy [37, 38, 168]. These techniques use time-varying electric fields travelling in free space or a waveguide cavity to perturb and probe the response of charges in a material. Moreover, THz spectroscopy has the added advantage that conductivity can be observed on a sub-100 fs timescale allowing charge-carrier dynamics to be followed and recombination parameters extracted [67].

Even within the THz spectroscopy regime, the charge-carrier mobility of $MAPbI_3$ thin films at room temperature has been reported to range from 8 to $35\,cm^2V^{-1}s^{-1}$ [36–38, 156]. However, owing to the lack of information about the grain size of those films, it is hard to conduct a systematic comparison between those experimental results and with theoretical models. Therefore, one would expect that the electrical mobility measured from perovskite single crystals would give much closer agreement with theory and between different experimental studies, because of the absence of grain boundaries. Surprisingly however, the mobility of $MAPbI_3$ single crystals has been reported to cover an even wider range (2.5 to $600\,cm^2V^{-1}s^{-1}$) than for thin films [147, 156, 168].

In this work, the electrical properties of the prototypical MHP $MAPbI_3$ single crystals and polycrystalline thin films are studied; and the direct experimental measurements of μ are compared with *ab initio* calculations based on the BTE and *GW* quasiparticle band structures. The measured temperature dependence of the single crystal's mobility shows close agreement with mobility calculated by solving the BTE [81]. A significant difference of the mobility temperature dependence is observed between polycrystalline and single-crystal morphologies, which is attributed to charge-carrier scattering from crystallographic grain boundaries. Indeed, by expanding the BTE theory to include such grain-boundary scattering, all the experimental

data can be replicated. Furthermore, the large variation in reported values of mobility, diffusion length and charge recombination constants for single-crystal MHPs are reconciled by accounting for the significant influence of photon reabsorption. Thus a direct experimental comparison of the electrical properties of single-crystal and polycrystalline MHPs are performed, which has helped to develop a wholistic model that predicts device-specific parameters such as electronic mobility and charge diffusion length of MHPs in a range of morphologies over a wide temperature range. Unlike most conventional semiconductor such as Si and GaAs, it is found that the transition from single crystals to polycrystalline films results in remarkably little degradation to the electrical properties of MHPs, which indicates highly benign grain boundaries in these materials.

4.2 Sample Fabrication

4.2.1 $MAPbI_3$ Single Crystal Growth

The $MAPbI_3$ perovskite single crystals were prepared by Jiali Peng (Wuhan University, China) using the technique of inverse temperature crystallization [23, 24]. A quantity of $1.25\,\mathrm{molL^{-1}}$ $MAPbI_3$ precursor was prepared by adding 461 mg PbI_2 and 159 mg methylammonium iodide (MAI) into 0.8 mL γ-Butyrolactone (GBL), heated at 60 °C for 2 hours with stirring. The precursors were filtered with syringe filters (0.22 μm pore size). The obtained solution was transferred to clean containers, which were kept on a stable hot plate and gradually heated to 120 °C and kept for another 6 hours. Crystals were formed at the bottom of the containers. Finally, the crystals were collected and dried at 60 °C in vacuum oven for 12 hours.

4.2.2 $MAPbI_3$ Thin Film Growth

The $MAPbI_3$ thin films were prepared by Dr. Jay Patel (University of Oxford, UK) and two steps were involved. (1) Cleaning of substrates: z-cut quartz substrates were cleaned with hellmanex solution, followed by a thorough rinse with deionized water. The substrates were then washed with acetone, isopropanol, and ethanol. Thereafter the substrates were plasma etched in O_2 for 10 minutes. (2) Thermal co-evaporation of $MAPbI_3$: the $MAPbI_3$ thin film was fabricated using thermal evaporation as reported previously [33]. In brief, MAI and PbI_2 were placed in separate crucibles, and the substrates were mounted on a rotating substrate holder to ensure that a uniform film was deposited. The temperature of the substrates was kept at 21 °C throughout the deposition. The chamber was evacuated to reach a high vacuum of $\sim 10^{-6}$ mbar, before heating the PbI_2 and the MAI. The substrates were then exposed to the vapor. The rates of both the MAI and PbI_2 were monitored using a quartz crystal microbalance. The thickness of the perovskite thin film was set by controlling the exposure time of the substrates to the vapor.

In order to estimate the grain size of the $MAPbI_3$ thin film, a top-down scanning electron microscope (SEM) image was taken over an area of $9\,\mu m \times 8\,\mu m$ and shown in Figure 4.1(a). An imaging processing program (ImageJ [169]) was used for analyzing the lateral size of each grain within this area and a histogram showing the distribution of grain sizes is presented in Figure 4.1(b), from which the grain size is found to be $(580 \pm 212)\,nm$. However, since some sub-grain features might be hidden in the SEM measurement [170], this value might be an overestimate of the true grain size. Alternatively, the grain size can also be extracted from X-ray diffraction (XRD) measurement which is shown in Figure 4.1(c), according to Scherrer equation [171],

$$g = \frac{K\lambda_{\text{source}}}{\beta \cos\theta}, \tag{4.1}$$

where $K \approx 0.94$ is the shape constant [172], $\lambda_{\text{source}} = 0.154\,\text{nm}$ is the wavelength of the X-ray source, β is the FWHM of each diffraction peak and θ is the Bragg angle. The resultant grain size averaged over the three diffraction peaks (110), (220) and (330) is $(31 \pm 10)\,\text{nm}$. In contrast to the SEM measurement, XRD measurement places a lower bound of the grain size, since the XRD peaks might be broadened further due to strain effect. Therefore, combining the results obtained from the SEM and XRD measurements, the grain size of the $MAPbI_3$ thin film is determined to be within the range 31–580 nm.

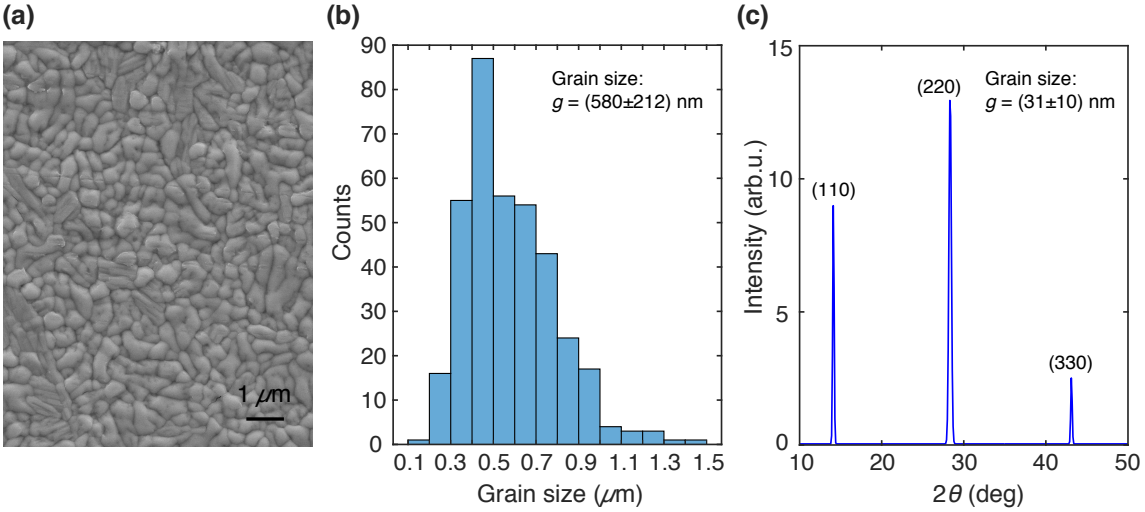

Figure 4.1: (a) An SEM image of the $MAPbI_3$ thin film measured in an area of $9\,\mu\text{m} \times 8\,\mu\text{m}$, which was taken by Dr. Mathias Uller Rothmann (University of Oxford, UK). (b) Histogram of the distribution of grain sizes at the surface of the thin film. (c) XRD spectrum of the thin film taken by Dr. Jay Patel.

4.3 Experimental and Computational Methods

4.3.1 Optical-Pump-THz-Probe Spectroscopy (OPTPS)

OPTPS was utilized to measure the photoconductivity and the electrical mobility of $MAPbI_3$ thin films and single crystals. The THz pulse was generated by an STE via the inverse spin Hall effect [112, 113]. An amplified ultrafast (35 fs) laser beam with

an average power of 4 W and central wavelength of 800 nm was split into three arms: a probe (THz) beam, a gate beam and a pump beam. The THz pulse was detected by a 0.1mm-thick (110) ZnTe crystal together with a Wollaston prism and a pair of balanced photodiodes via electro-optic sampling. The pump beam was converted from 800 nm to 400 nm by a BBO crystal to photo-excite the $MAPbI_3$ thin films and single crystals. Under photo-excitation, the photoinjected charge carriers gave rise to a reduction of the THz intensity, which is known as photoconductivity and used for extracting the electrical mobility (see Section 3.1.3.1 for more details). Whilst the photoconductivity of $MAPbI_3$ thin film was measured in transmission mode, the photoconductivity of the single crystal was measured in reflection mode instead since little THz signal can transmit through the thick crystal. All measurements were repeated three times at each temperature, from which the uncertainty was determined by the standard deviation. Since the single crystal was measured in reflection mode, which has a lower SNR than the transmission measurement of the thin film, measurements of the single crystal, which will be discussed Section 4.4.2, show larger uncertainties.

4.3.2 Thermometry and Temperature-Dependent PL Spectroscopy

The very low thermal conductivity of $MAPbI_3$ which has been reported to be below $0.5\,W(mK)^{-1}$ [173–175] and hundreds of times smaller than that of conventional semiconductors such as GaAs [176], means that extreme care must be taken when making temperature-dependent measurements, especially when the samples are exposed to localized heating, such as laser excitation. For the $MAPbI_3$ thin film which was deposited on a quartz substrate, the issue of low thermal conductivity of the film is neglected due to its close contact with the quartz substrate which has a high thermal conductivity over a wide temperature range. Unfortunately for the cm-sized $MAPbI_3$

single crystal, the low thermal conductivity makes the experiments extremely challenging, and great care needs to be taken to ensure that the recorded temperature is actually the lattice temperature at the position where the mobility measurements are made. Therefore, a PL-corrected THz technique was developed to measure the mobility of the $MAPbI_3$ single crystal with accurate temperature determination and are described as below.

Firstly, to improve the thermal contact between the single crystal and the cold-finger cryostat (Oxford Instruments, MicrostatHe), which was used to change the crystal temperature in the OPTPS measurement, a sapphire substrate was inserted at the front of the single crystal, so that the heat generated by the pump beam could be dissipated more efficiently, which enabled the crystal to cool down to 75 K and a clear phase transition in its PL spectrum could be observed at 160 K. In the meantime, to determine the crystal temperature more accurately, the PL spectrum was measured at different temperatures using both the cold-finger and gas-exchange cryostats. In the gas-exchange-cryostat setup (Oxford Instruments, OptistatCF2) which is separate from the OPTPS setup, since the crystal is immersed in helium gas, there is no thermal contact issue and the temperature registered by the sensor in the gas-exchange cryostat is the true temperature of the crystal. Therefore, the PL spectrum taken by the gas-exchange cryostat was used as a reference to correct the temperature measured by the cold-finger cryostat. In the cold-finger-cryostat setup, the PL spectrum was generated from excitation by the pump beam (400 nm, 35 fs) used in the OPTPS setup and collected by a fibre-coupled spectrometer (Horiba Scientific, iHR320) and detected by a CCD (Horiba Scientific, Si Symphony II). In the gas-exchange-cryostat setup, the PL spectrum was generated from excitation by a picosecond pulsed diode laser (PicoHarp, LDH-D-C-405M) at central wavelength of 398 nm with the signal subsequently collected and coupled into a different spectrometer (Princeton Instruments, SP-2558), and detected by an iCCD (Princeton

Instruments, PI-MAX4).

Figures 4.2–4.4 show the PL spectra of the $MAPbI_3$ single crystal and thin film measured at temperatures ranging from 5 K to 295 K, where each PL spectrum is fitted with a 2-Gaussian distribution function to extract the central wavelengths P1 and P2, which is plotted in Figure 4.5 as a function of temperature.

Since P1 and P2 converge to the same wavelength above 160 K and P1 is more prominent in the cold-finger cryostat measurement of the single crystal (see Figure 4.3), P1 is taken as the reference PL peak for correcting the single crystal's temperature. As shown in Figure 4.6(a), before temperature correction, P1 of the single crystal measured by the cold-finger cryostat (pink triangle) deviates from the gas-exchange measurement, whereas the thin-film measurement shows a good agreement due to its good thermal contact with the cold-finger cryostat. In Figure 4.6(b), the cold-finger cryostat temperature is matched with the gas-exchange measurement, from which the single crystal's real temperature accurately are determined. One might have noticed that the relative intensity of P1 and P2 is slightly different between the gas-exchange measurement (Figure 4.2) and the cold-finger measurement (Figure 4.3) of the single crystal at 140 K and 150 K. This is attributed to the different excitation fluence between these two sets of measurements, which differs by two orders of magnitude. In addition, the extra sapphire substrate in the cold-finger cryostat configuration may also affect the photon reabsorption and emission in the $MAPbI_3$ single crystal, which results in different intensity ratios between P1 and P2. Nevertheless, the more crucial feature in the PL spectra measurement is the peak positions of P1 and P2, whilst the relative intensity is less informative. As shown in Figure 4.6, the phase shift observed at 160 K is a clear indication of the validity of the cold-finger cryostat measurement and P1 alone suffices to determine the temperature of the $MAPbI_3$ single crystal accurately.

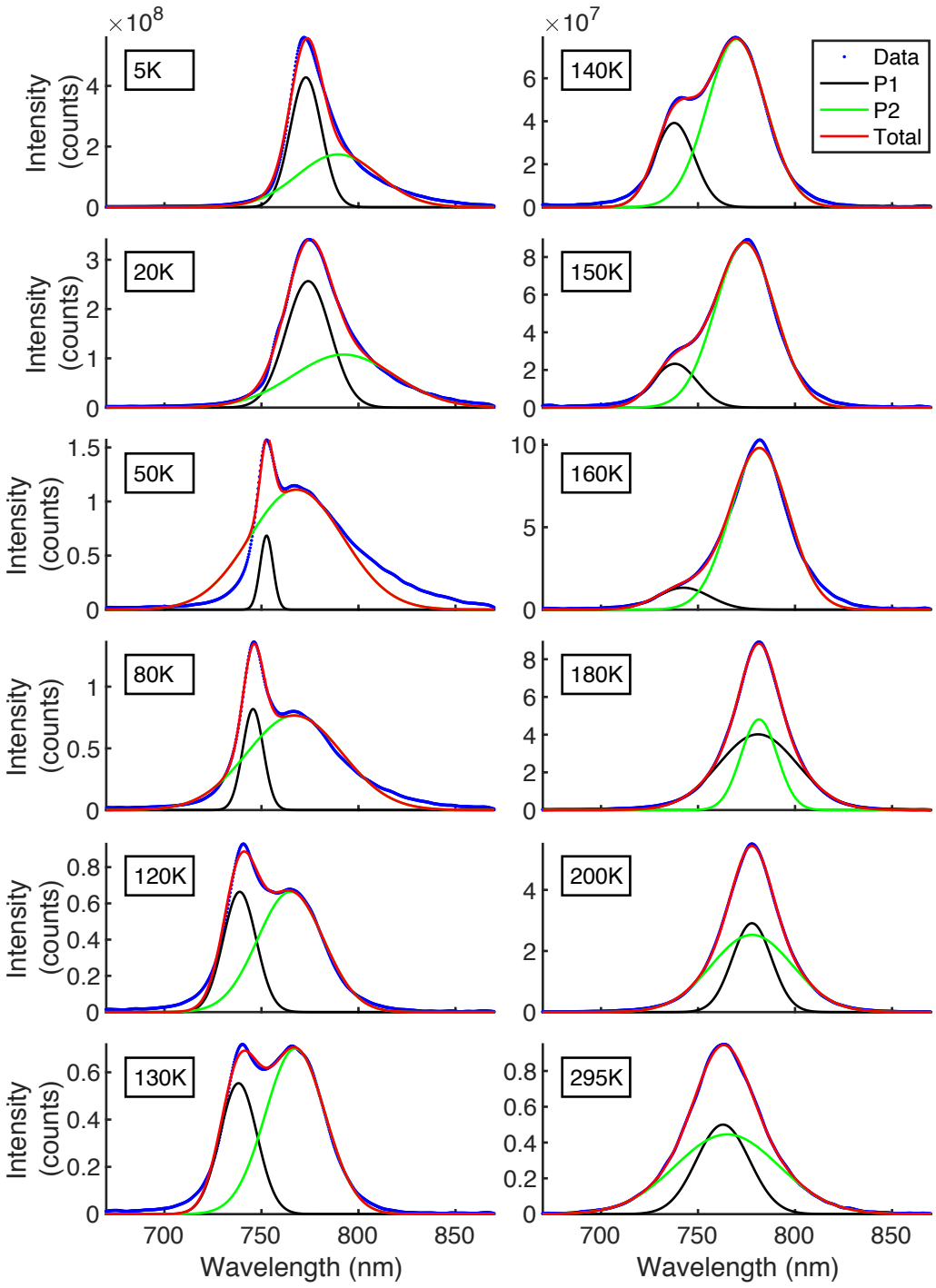

Figure 4.2: PL spectra of the $MAPbI_3$ single crystal measured by the gas-exchange cryostat at different temperatures. The crystal was photo-excited by a pulsed laser at 398 nm with 10 kHz repetition rate and 0.2 $\mu J/cm^2$ fluence. The blue dots represent the PL data, whereas the red curve represents the Gaussian fit which consists of two peaks represented by the black and green curves, respectively.

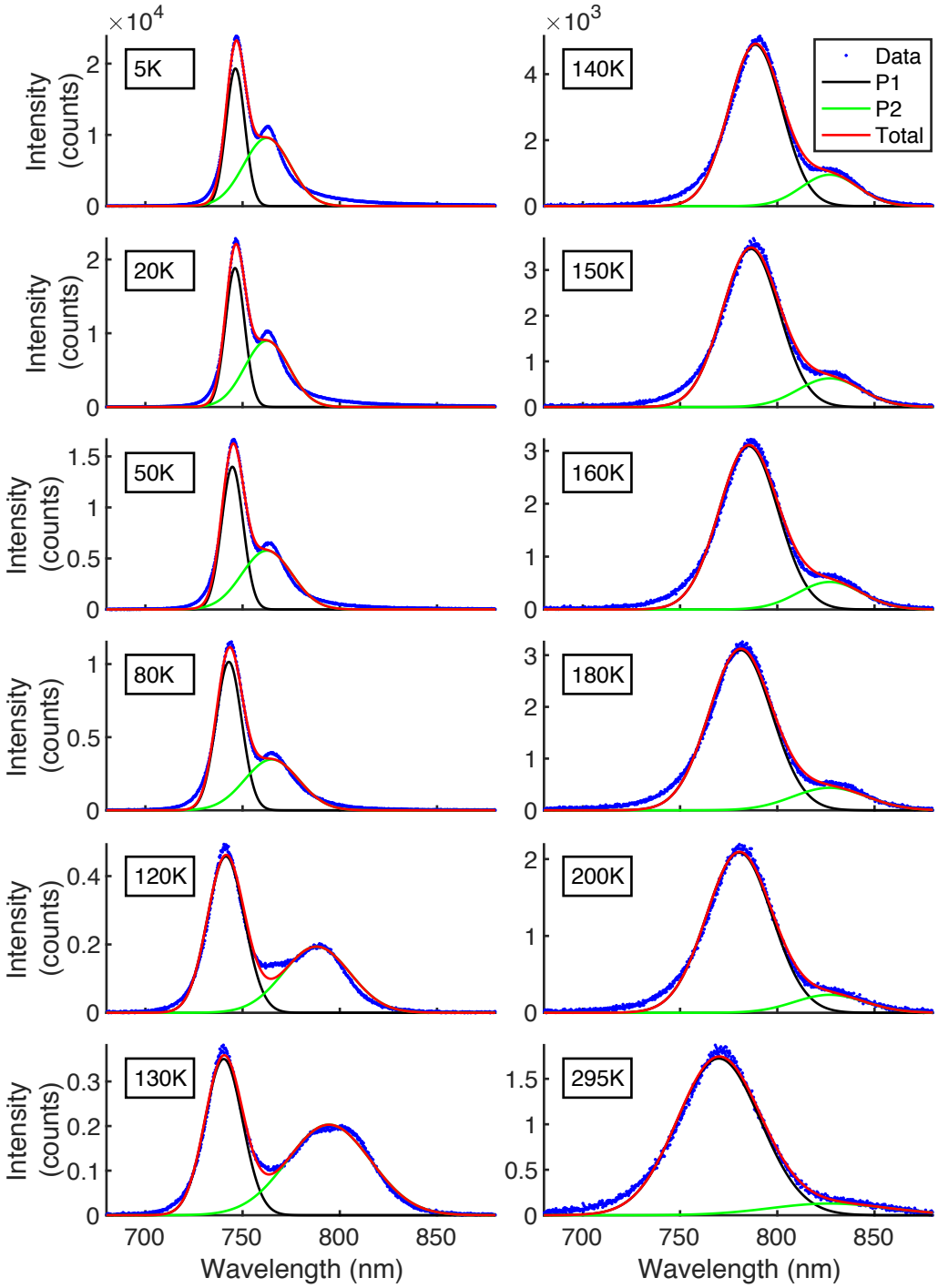

Figure 4.3: PL spectra of the $MAPbI_3$ single crystal measured by the cold-finger cryostat at different temperatures. The crystal was photo-excited by an amplified pulsed laser at 400 nm with 5 kHz repetition rate and 30.8 $\mu J/cm^2$ fluence.

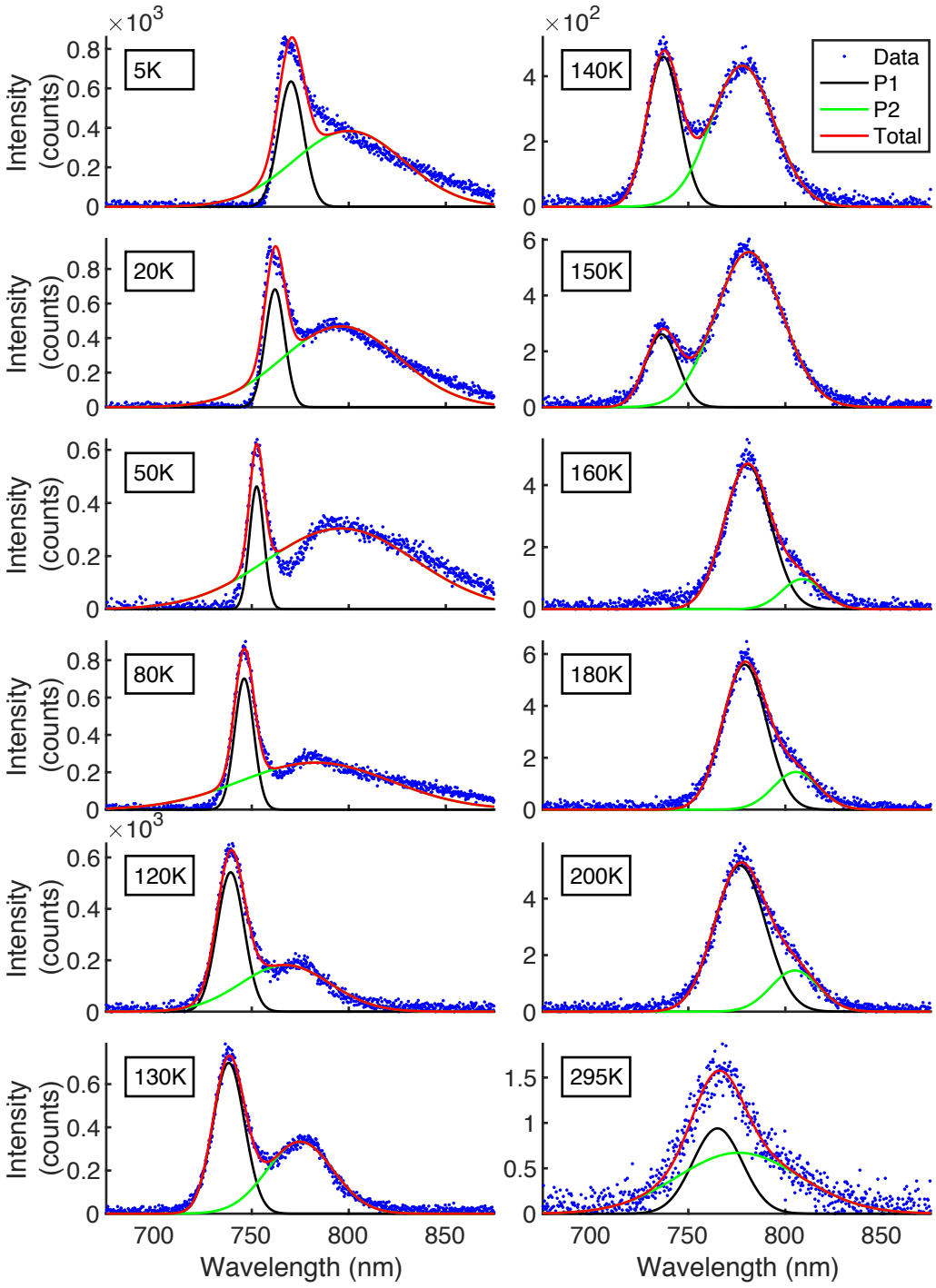

Figure 4.4: PL spectra of the $MAPbI_3$ thin film measured by the cold-finger cryostat at different temperatures. The thin film was photo-excited by an amplified pulsed laser at 400 nm with 5 kHz repetition rate and 30.8 $\mu J/cm^2$ fluence.

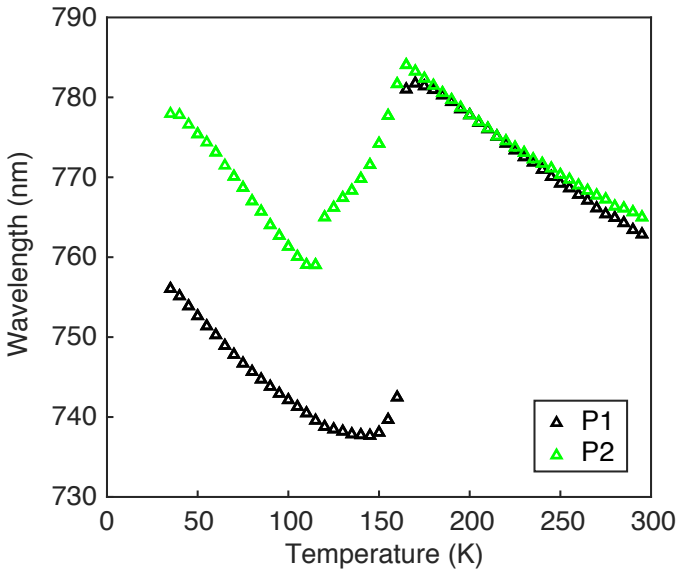

Figure 4.5: Central wavelength of the single crystal's PL spectrum measured by the gas-exchange cryostat as a function of temperature. The black and green triangles represent P1 and P2 respectively.

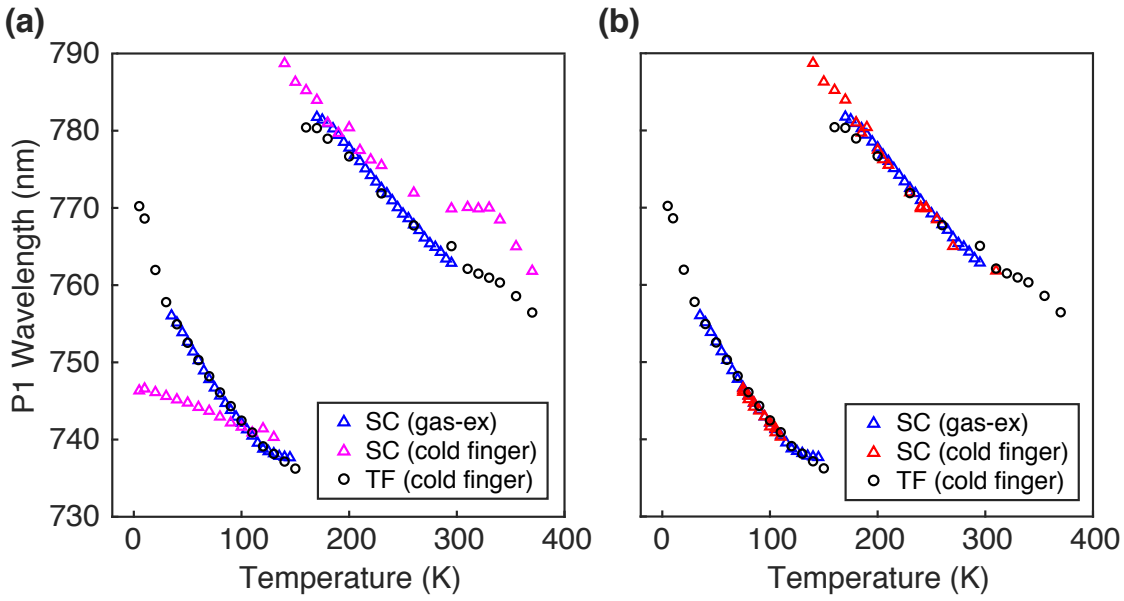

Figure 4.6: Central wavelength P1 of the $MAPbI_3$ single crystal and thin film as a function of temperature (a) before and (b) after temperature correction. The blue triangles represent the single crystal data obtained by the gas-exchange cryostat and the black circles represent the thin-film data obtained by the cold-finger cryostat. The pink and red triangles represent the cold-finger cryostat measurements of the single crystal before and after temperature correction respectively.

4.3.3 Computational Method

To obtain the theoretical values of the $MAPbI_3$ perovskite's mobility, DFT calculations were performed by Dr. Samuel Poncé (University of Oxford, UK) using pseudopotentials and planewaves, as implemented in the QUANTUM ESPRESSO package [177], as well as the local density approximation (LDA) with norm-conserving pseudopotentials from the PseudoDojo repository [178]. Fully relativistic pseudopotentials were used which includes the effect of spin-orbit coupling and semicore electrons in the case of Pb. A plane-wave kinetic energy cutoff of 100 Ry was used along with the following orthorhombic lattice parameters: $a = 8.836$ Å, $b = 12.581$ Å, and $c = 8.555$ Å [88]. Phonons were calculated using DFPT [79, 90] with a 4×4×4 **k**-point grid and a 2×2×2 **q**-point grid. The DFT band structures were corrected via the quasiparticle *GW* method, using the Yambo code [179]. A higher plane-wave kinetic energy cutoff of 150 Ry was employed, with the exchange self-energy and the polarizability evaluated using cutoffs of 80 Ry and 6 Ry respectively. The summations over empty states were performed using 1000 bands for the calculation of the polarization and the Green's function. The frequency-dependence of the screened Coulomb interaction was described via the Godby-Needs plasmon-pole model [180], using a plasmon-pole energy of 18.8 eV. Since the DFT gap of MHPs is very small due to spin-orbit coupling [41], the *GW* approximation was extended by including self-consistency on the eigenvalues. Self-consistency was applied by using the strategy of Ref. 83 which includes a wavevector-dependent scissor so as to obtain accurate effective masses. The Brillouin zone was sampled via a 4×4×4 unshifted grid, and the termination scheme of Ref. 181 was employed to accelerate the convergence with respect to the number of empty states. The electron-phonon matrix elements and scattering rates were calculated using the EPW code [182], in conjunction with the wannier90 library [183].

4.4 Results and Discussions

4.4.1 Electrical Mobility and Charge-Carrier Dynamics at Room Temperature

To determine the fundamental upper limit to the mobility of $MAPbI_3$ and hence answer the questions of the influence of grain boundaries and what might be the upper performance limit of perfectly crystalline thin film devices, the electronic properties of single crystal samples are studied and compared directly to those of high-performance polycrystalline thin films. A photograph of one of the crystals is shown in Figure 4.7(a) showing large (10 mm×10 mm) optically flat facets. An SEM image of the (100) facet is displayed in Figure 4.7(b) and reveals some evidence of shallow pitting on a sub-micrometer length-scale. High-quality $MAPbI_3$ polycrystalline thin films grown on quartz substrates using vapor co-deposition are also investigated. It is important to study thin films that are representative of those used in high-efficiency devices, thus the same deposition parameters utilized to produce single-junction solar cells with over 19% PCE (details are given in Section 4.2.2) [33] are used in this study. One of the highly reproducible 600 nm-thick films used in this study is shown in Figure 4.7(d) and featured an optically flat surface, as is typical of vapor-co-deposited films. The SEM image displayed in Figure 4.7(e) reveals a dense assembly of grains, while a more detailed analysis of the size distribution is presented in Figure 4.1 giving a mean length-scale of ~ 580 nm. It should be stressed that this value represents an upper limit of grain size as internal misorientation and strain are not revealed by SEM analysis [170], and smaller crystals may also be present below the observed surface. This suggests that the grain size obtained from the SEM measurement places an upper limit of the real grain size of polycrystalline thin films. Another method to assess crystal size is to examine Scherrer broadening in XRD peaks resulting from the finite size of the small crystallites. As expected, the XRD peaks measured from

the thin film (Figure 4.7(f)) are significantly broadened compared with those of the single crystal (Figure 4.7(c)), with the Scherrer equation returning a crystallite size for the $MAPbI_3$ thin film of $\sim 31\,\text{nm}$. This value represents a lower limit of crystal size as the contributions of strain and disorder to broadening an XRD peak width are not included in the Scherrer equation [184]. Thus the true lateral extent of crystals in the polycrystalline thin films is expected to be $\sim 100\,\text{nm}$ and within the bounds 31–580 nm.

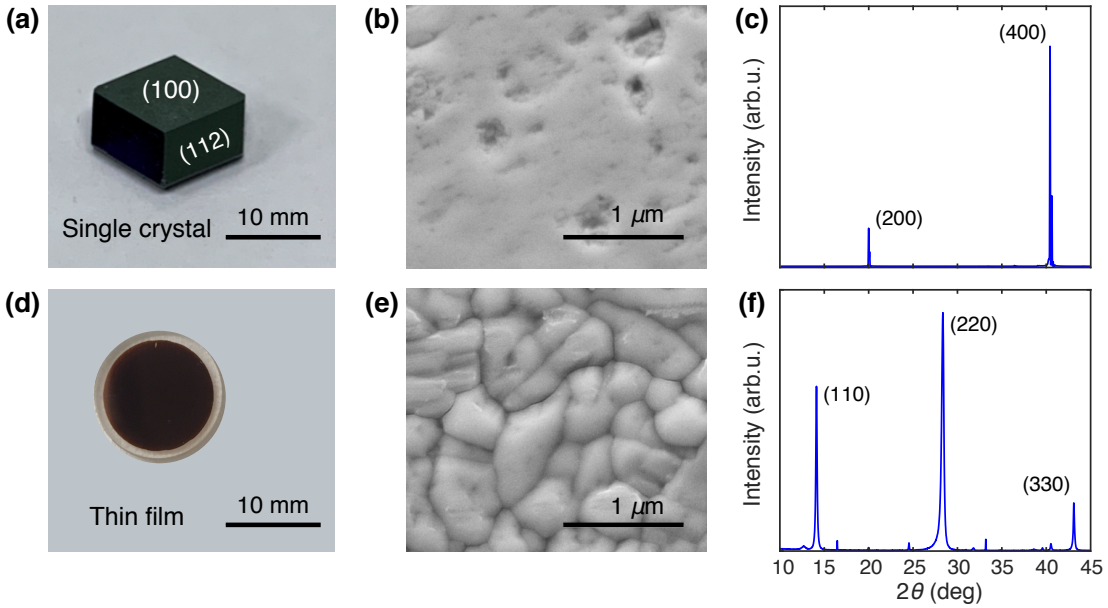

Figure 4.7: Photographs of $MAPbI_3$ (a) single crystal and (d) thin film grown on a quartz substrate. SEM images of (b) the single crystal's (100) facet and (e) the thin film's plane-surface, which were taken by Dr. Mathias Uller Rothmann. XRD data of (c) the single crystal's (100) facet (taken by Jiali Peng) and (f) the thin film (taken by Dr. Jay Patel). The indices such as (200) and (110) represent the typical lattice planes observed in $MAPbI_3$ assigned according to previously reported XRD pattern in tetragonal phase [88].

The electrical mobility and charge recombination dynamics of thin-film and single-crystal samples are recorded using the technique of OPTPS. The samples are photo-excited by short (35 fs) pulses of blue light (photon energy 3.1 eV, central wavelength 400 nm) and photoconductivity-probed with a sub-picosecond THz pulse. Figures 4.8(a) and (b) show the room-temperature photoconductivity of the thin-film

and single-crystal $MAPbI_3$ respectively, as a function of time after photo-excitation by laser pulses with fluences ranging from 4.5 to 71 $\mu J/cm^2$. The combined electron and hole mobility, $\mu_e + \mu_h$, at room temperature is found to be $(33 \pm 2)\,cm^2V^{-1}s^{-1}$ for the thin film and $(59 \pm 3)\,cm^2V^{-1}s^{-1}$ for the single crystal by examining photoconductivity immediately after photo-excitation at low excitation fluence. While the electrical mobility of the thin film is almost half that of the single-crystal $MAPbI_3$ sample, it does not show the three order-of-magnitude drop in mobility seen between single-crystal and polycrystalline GaAs [185, 186], indicating that grain boundaries may be more benign in MHPs.

Figures 4.8(a) and (b) show the photoconductivity dynamics of the polycrystalline and single-crystal $MAPbI_3$ respectively. Observation of such decays in photoconductivity after pulsed photo-excitation allow important material parameters for device modelling to be extracted such as charge recombination constants (Shockley-Read-Hall, bimolecular and Auger). These parameters also allow the diffusion length L_D of charge carriers in the material to be determined for any charge-carrier density in the semiconductor [67]. The decay of photoconductivity for the thin-film $MAPbI_3$ is shown in Figure 4.8(a) and is seen to depend strongly on the photo-excitation fluence, i.e. the density of photoinjected electron-hole pairs. This phenomenon has been observed previously and rate equations are used to extract recombination parameters [36, 38, 71].

In contrast to the thin-film data, the decay of photoconductivity seen in Figure 4.8(b) for the single crystal appears quite different, despite the excitation conditions being identical. Such behavior in single crystals has been observed before, and is attributed to significantly higher values of charge carrier lifetime, long diffusion lengths [35, 147] and hence potentially much better device performance. However, here it is shown that the fundamental recombination parameters underlying these decay curves are remarkably similar between thin films and single crystals despite the

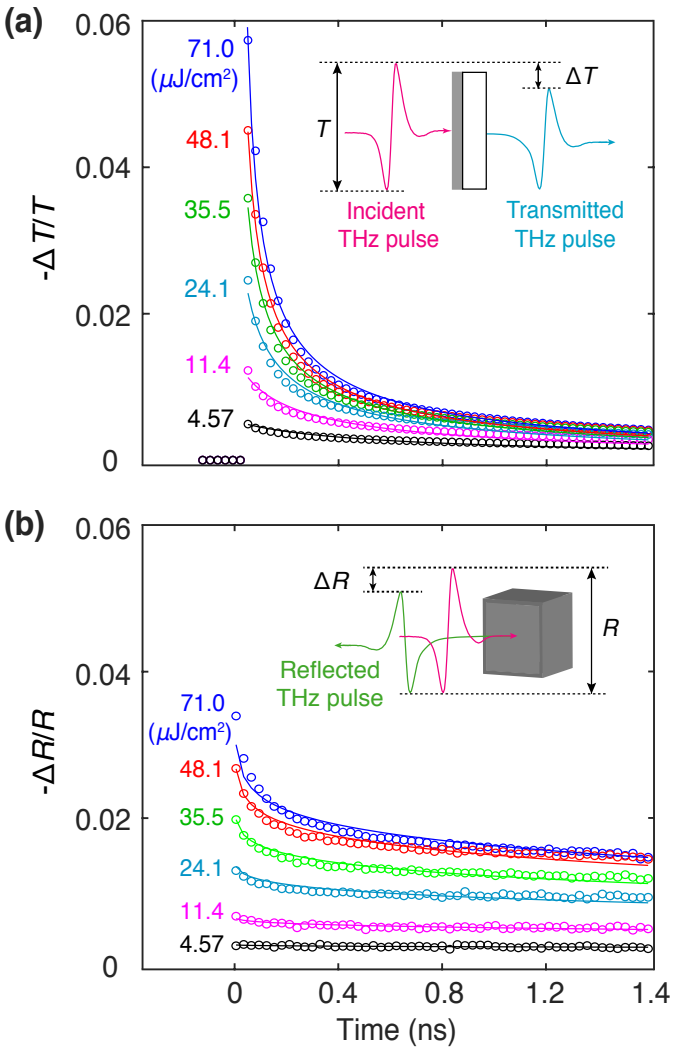

Figure 4.8: Photoconductivity decay dynamics at room temperature of the $MAPbI_3$ (a) thin film measured in transmission and (b) single crystal measured in reflection. The insets illustrate the experiment geometry with the photo-excitation and probing THz pulses incident normally on the sample surface. The theoretical fits (colored lines) based on the photon-reabsorption model were done by Dr. Timothy Crothers (University of Oxford, UK).

large differences between the data in Figure 4.8(a) and (b). Indeed the extended decay curves seen in Figure 4.8(b) arise from photon reabsorption. That is photons emitted as a result of bimolecular recombination of electrons and holes are reabsorbed, and produce new electron-hole pairs, rather than the photons escaping the semiconductor.

Using the photon-reabsorption approach developed by Crothers *et al.* [71] the thin-

film and single-crystal data shown in Figure 4.8 are modelled with Equation (2.2). The circles in Figures 4.8(a) and 4.8(b) represent experimental data while the solid curves are global fits to Equation (2.2). Full details of the model and all fitting parameters will be discussed in Section 4.4.4. The photoconductivity dynamics over the time and fluence range of the experiments presented in Figure 4.8 are expected to be dominated by bimolecular (radiative) recombination, and the large contrast in photoconductivity decay between the single-crystal and thin-film data at first sight indicates a large difference in their radiative recombination. However, on applying the full rate-equation model given by Equation (2.2), it is clear that the slower photoconductivity decay of the thick single crystal arises primarily from photon reabsorption, with the underlying bimolecular recombination being remarkably similar to that of the thin film. The extracted bimolecular recombination constant of the single crystal is $k_{2,\mathrm{crystal}} = 8.7 \times 10^{-10}\,\mathrm{cm^3 s^{-1}}$ which is of the same order of magnitude as that of the thin film ($k_{2,\mathrm{film}} = 2.6 \times 10^{-10}\,\mathrm{cm^3 s^{-1}}$). The physical origin of the small drop in the bimolecular recombination constant in the thin film compared with the single crystal is likely to be associated with a small degree of electron-hole separation at grain boundaries in the thin films. Thus the bimolecular recombination in single-crystal $MAPbI_3$ is shown to be consistent with the thin-film value measured in this study and also with previously reported values of other $MAPbI_3$ thin films [38, 71].

One of the most dramatic differences between thin-film and single-crystal $MAPbI_3$ has been the much larger charge-carrier diffusion lengths L_D observed for thick single crystals under 1 sun illumination conditions ($1\,\mathrm{kWcm^{-2}}$ AM1.5-filtered). Indeed, when photon reabsorption is neglected in the analysis of the photoconductivity data (see Section 4.4.4 for more details), a large increase from $L_{\mathrm{D,film}} = 1\,\mu\mathrm{m}$ for thin-film to $L_{\mathrm{D,crystal}} = 5.3\,\mu\mathrm{m}$ for single-crystal $MAPbI_3$ is observed. However this represents a significant overestimate of the true diffusion length. Analyzing the same data but in this case including the effects of photon reabsorption, it is found that the increase in

diffusion length from thin film to single crystal is less significant ($L_{\mathrm{D,film}} = 1\,\mu\mathrm{m}$ and $L_{\mathrm{D,crystal}} = 5\,\mu\mathrm{m}$). Therefore, large performance increases are unlikely to be achieved in moving from polycrystalline to single-crystal devices.

In order to gain a better understanding of fundamental limits to intrinsic electrical mobility and charge-carrier diffusion length in $MAPbI_3$, the *ab initio* BTE [81] is solved in conjuction with the many-body *GW* method and DFPT. The room-temperature electron and hole mobilities for a perfect single-crystal $MAPbI_3$ are calculated to be $\mu_{\mathrm{e}} = 33\,\mathrm{cm^2V^{-1}s^{-1}}$ and $\mu_{\mathrm{h}} = 50\,\mathrm{cm^2V^{-1}s^{-1}}$ respectively, giving a total electrical mobility $\mu = \mu_{\mathrm{e}} + \mu_{\mathrm{h}} = 83\,\mathrm{cm^2V^{-1}s^{-1}}$. This value should represent an upper limit of any measurement on an imperfect real crystal, which will contain impurities, defects and surfaces. Thus the value of mobility measured on the real crystal used in this study, $(59 \pm 3)\,\mathrm{cm^2V^{-1}s^{-1}}$, agrees well with the value calculated using the first-principles technique. It is noted that the computed mobility is lower than previous calculations [124, 137, 187, 188] which neglected the role of multi-phonon Fröhlich coupling as discussed in Ref. 189. This is crucial since at least two sets of modes contribute to the mobility of halide perovskites [83]. Specifically, charge-carrier scattering (and hence mobility) in $MAPbI_3$ is primarily influenced by three LO phonon modes: (i) a Pb–I–Pb bending mode with a 4.3 meV energy, (ii) a dominant Pb–I stretching mode at 14.4 meV that accounts for half of the scattering and (iii) a broad contribution around 21 meV originating from the librational modes of the MA molecules. Thus including multiple phonon modes in calculations of charge-carrier scattering reconciles the overestimate of theoretical mobility in $MAPbI_3$ compared with experimental values.

4.4.2 Temperature-Dependence of Electrical Mobility

To test the validity of the multiple-phonon-mode BTE model, the measured and calculated values for the electrical mobility of $MAPbI_3$ are compared over a wide temperature range. Figure 4.9(a) displays the measured electrical mobility of single-crystal $MAPbI_3$ (red circles) over a temperature range 75–310 K in comparison to the multi-phonon-mode BTE calculations (orange line). As temperature is lowered, mobility increases which is consistent with reduced occupancy of phonon modes, and hence reduced electron-phonon Fröhlich coupling.

Experimental mobility data are often fitted with a temperature power law relation to help determine the physical origin of scattering [124, 156]. However, simple power law models of LO-phonon coupling assume only one LO phonon branch and simplified dispersion relations, which are clearly not applicable for $MAPbI_3$ which has many atoms in its primitive unit cell basis, and hence a dense phonon spectrum. Thus the only way to properly account for the temperature dependence of electrical mobility in MHPs is to consider the occupancy and Fröhlich coupling of all significant phonon modes as a function of temperature, as what has been done with the BTE model.

The temperature dependence of electron and hole mobilities calculated by solving the BTE for a pure $MAPbI_3$ crystal without any impurities is shown in Figure 4.9(c), while the combined electron and hole mobility (orange line) is compared with the experimental mobility data (red circles) in Figure 4.9(a). It is expected that the calculated mobility will represent an upper limit for the mobility of any real crystal, owing to the presence of impurities in real crystals. Indeed the experimental single crystal data (red circles) agrees well with the shape of the theoretical data and is bounded by it. The overestimate is somewhat higher at lower temperatures, where ionized impurity scattering, which is not included in the BTE calculations, becomes more significant.

In contrast, the values of experimental mobility are significantly lower for the

polycrystalline thin film (blue circles in Figure 4.9(a)) compared with the single crystal and importantly the discrepancy becomes larger at lower temperature. It is hypothesized that this difference is related to the presence of grain boundaries in the polycrystalline thin films, which is tested by modelling grain-boundary scattering within the BTE framework, as will be discussed in the following section.

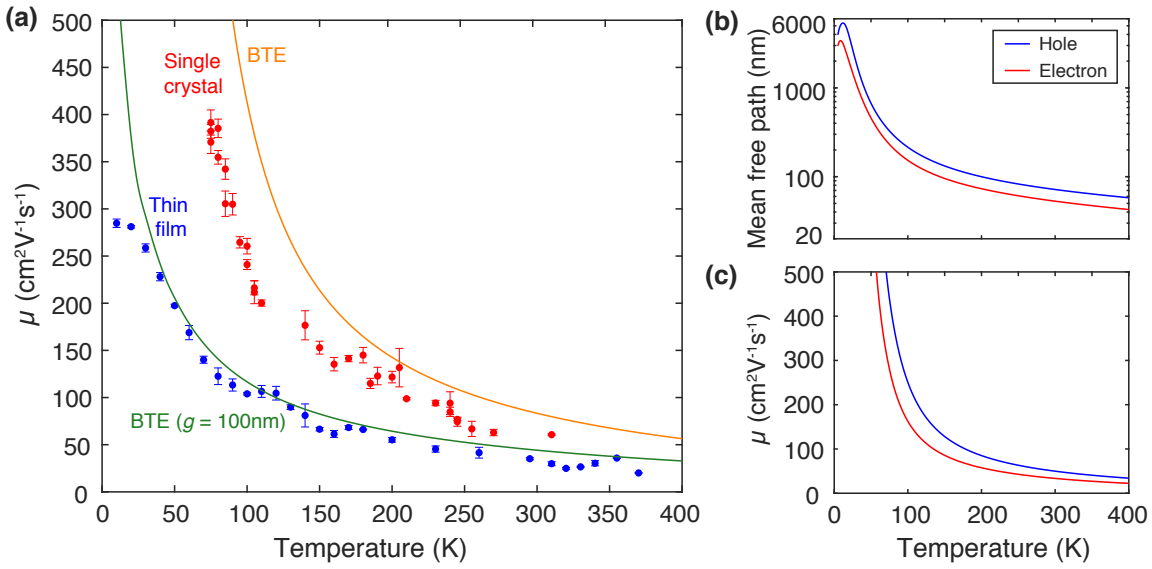

Figure 4.9: (a) Charge-carrier mobility plotted as function of temperature, where the blue and red circles represent the experimental data of thin film and single crystal respectively. The orange line represents the *ab initio* BTE calculation of intrinsic phonon-limited mobility where all the phonon modes are included, whilst the green line represents the BTE calculation including grain-boundary scattering as well with the crystal size set to $g = 100\,\text{nm}$. (b) Mean free path and (c) intrinsic mobility for the single crystal orthorombic phase of $MAPbI_3$. The carrier mobility is obtained by solving the BTE (without grain-boundary scattering) in the self-energy relaxation time approximation. Theoretical calculations (colored lines) performed by Dr. Samuel Poncé.

4.4.3 Grain-Boundary Scattering in $MAPbI_3$ Thin Films

To gain insight into the influence of grain boundaries on the electrical mobility of polycrystalline $MAPbI_3$, the model of Mayadas and Shatzkes [84] is implemented where the mean free path of charge carriers is limited by the extent of grain boundaries. The model is an extension of the Boltzmann transport theory to include reflection of the charge carriers at the grain boundaries of polycrystalline thin films, which is described in more details in Section 2.1.3. The green line in Figure 4.9(a) shows the *ab initio* calculated μ_{film}, with crystal grain size g as the only free parameter. A grain size $g = 100\,\text{nm}$, which as discussed earlier is reasonable for the thin-film samples, is found to be in excellent agreement with experimental mobility data for temperatures above 30 K. Below 30 K exciton formation, which is not included in the theoretical model, is expected to dominate and is consistent with the reduced experimental mobility at low temperatures. The effect of increasing and reducing grain size on mobility is displayed in Figure 4.10 with mobility being most sensitive to grain size at temperatures below 200 K. Thus the BTE theory, when corrected for grain-boundary scattering, provides an excellent prediction of electrical mobility in $MAPbI_3$ for polycrystalline and single-crystal morphologies over a wide temperature range. In other words, as the grain size increases, the mobility increases as well, since the charge carriers get scattered off the grain boundaries less frequently within the distance of their mean free path. Ultimately, if the grain size is large enough (greater than the charge-carrier mean free path), the grain-boundary-limited mobility will approach the mobility predicted by the BTE (red curve), which represents the mobility of a pure $MAPbI_3$ single crystal.

On the other hand, while the grain-boundary scattering model successfully predicts the electrical mobility of $MAPbI_3$ polycrystalline thin films as a function of temperature, it is possible that some defects or impurities can also affect the temperature-dependent trend of the mobility. Further investigations about the effect of defect scat-

tering may help to understand the limitations to $MAPbI_3$ perovskite charge-carrier mobility more thoroughly.

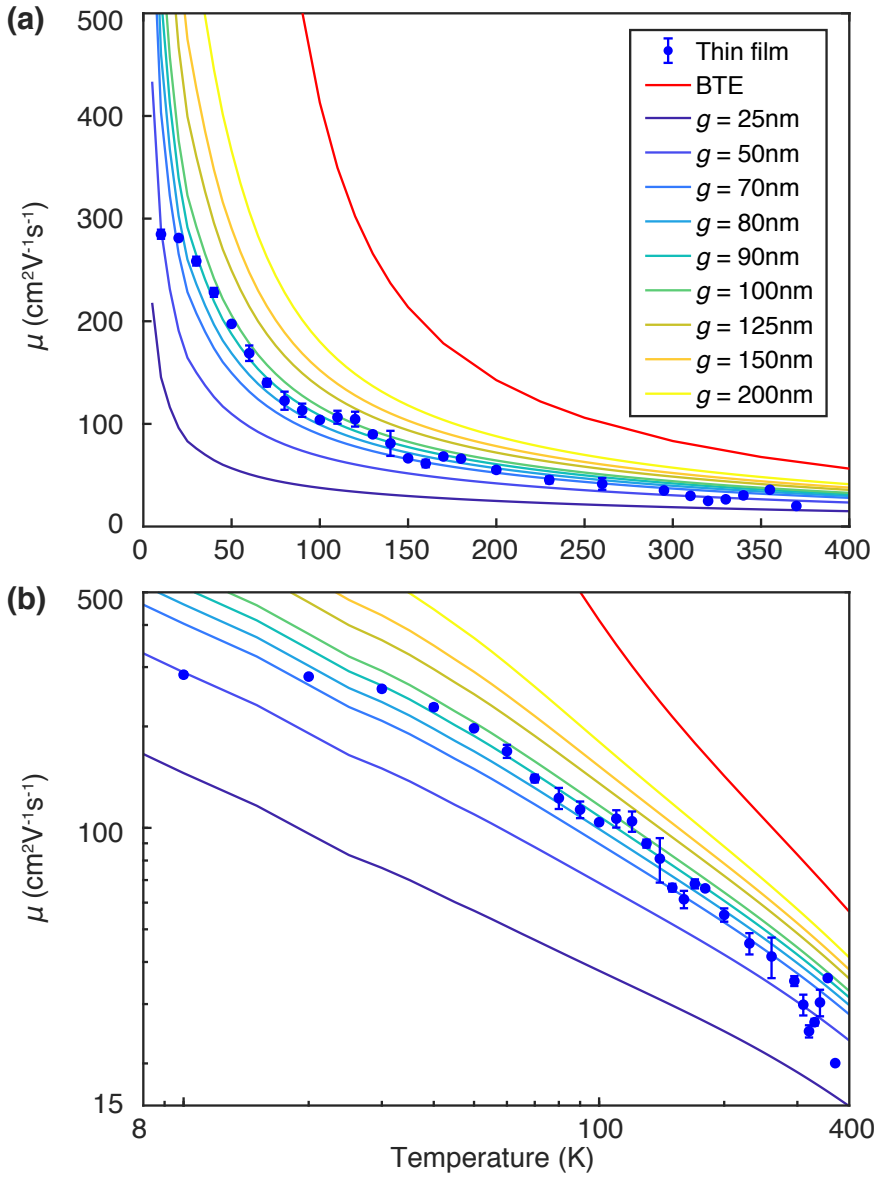

Figure 4.10: (a) Intrinsic carrier mobility of $MAPbI_3$ calculated by the BTE (red) compared with the mobility resulting from the addition of grain-boundary scattering effects using the *ab initio* transport mean free path. The blue dots represent the experimental mobility data of $MAPbI_3$ thin film. (b) Same mobility plot on a log-log scale to illustrate the effect of grain size on the temperature-dependent exponent. The theoretical calculations (colored lines) were performed by Dr. Samuel Poncé.

4.4.4 Significance of Photon Reabsorption and Its Effect on Charge-Carrier Dynamics and Diffusion Length

As mentioned in Section 2.1.1, since the $MAPbI_3$ single crystal is significantly thicker than the $MAPbI_3$ thin film, the effect of photon reabsorption is much more prominent in the single crystal and therefore, in order to analyze the charge-carrier dynamics properly, it is crucial to take into account the effect of photon absorption by using Equation (2.2). Here, the results obtained from the photon-absorption model are compared with those obtained from a simple model governed by Equation (2.1) where photon reabsorption is neglected. It shows that photon reabsorption not only affects the charge-carrier recombination rates but also the carrier diffusion lengths, both of which are extracted from the photoconductivity decay dynamics.

In order to extract the charge-carrier recombination constants, in particular the bimolecular recombination constant k_2, a few parameters in Equation (2.2) need to be determined. Firstly, the Auger recombination constant is approximated as zero, since the photo-excitation fluence applied in the OPTPS experiment is so small that Auger recombination is negligible. Secondly, the monomolecular recombination k_1 is determined from the time-resolved photoluminescence (TRPL) measurement which is shown in Figure 4.11. According to the exponential fit to the TRPL spectrum measured at the lowest fluence, it is found that $k_{1,\mathrm{film}} = 8.3 \times 10^7\,\mathrm{s}^{-1}$ for the thin film and $k_{1,\mathrm{crystal}} = 5.3 \times 10^6\,\mathrm{s}^{-1}$ for the single crystal respectively, suggesting the single crystal has a longer charge-carrier lifetime (190 ns) than the thin film (12 ns).

In addition, as shown in Figure 4.12, at early times (within the first 100 ps), the $MAPbI_3$ thin film shows a faster decay at the lowest photo-excitation fluence, whereas the single crystal shows a clear fluence-dependent carrier decay trend. This suggests the thin film sample has a higher trap density than the single crystal sample. At the lowest fluence, photo-injected electrons decay rapidly to the unoccupied trap states, giving rise to a fast decay rate [190]. As the fluence increases, the trap states are

gradually filled and eventually saturated. Therefore, at higher fluences, the carrier decay rate increases with fluence. In contrast, since the single crystal has a lower trap density, even at the lowest fluence ($1.2\,nJ/cm^2$), the trap states are already saturated and hence the carrier decay rate increases monotonically with fluence.

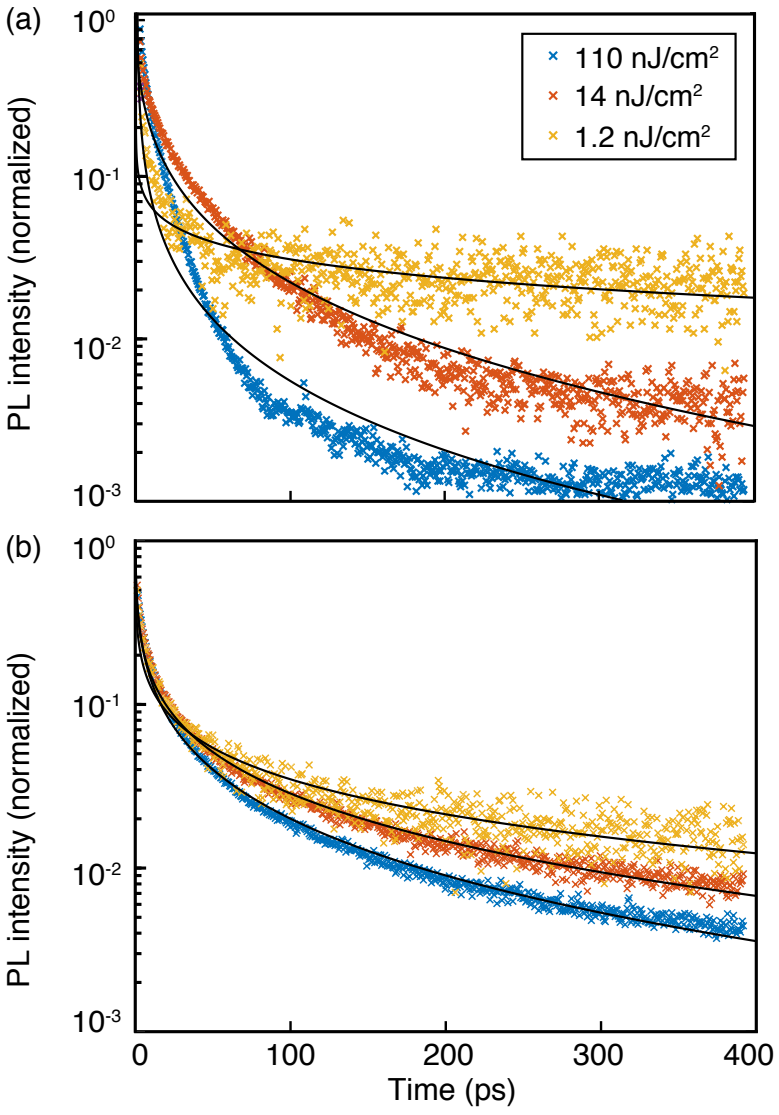

Figure 4.11: Time-resolved photoluminescence (TRPL) spectra of the $MAPbI_3$ (a) thin film and (b) single crystal measured over 400 ps at various fluences. The black lines represent the exponential fits to the experimental data (colored crosses), from which k_1 is extracted. The experimental data were taken and analyzed by Dr. Adam Wright (University of Oxford, UK).

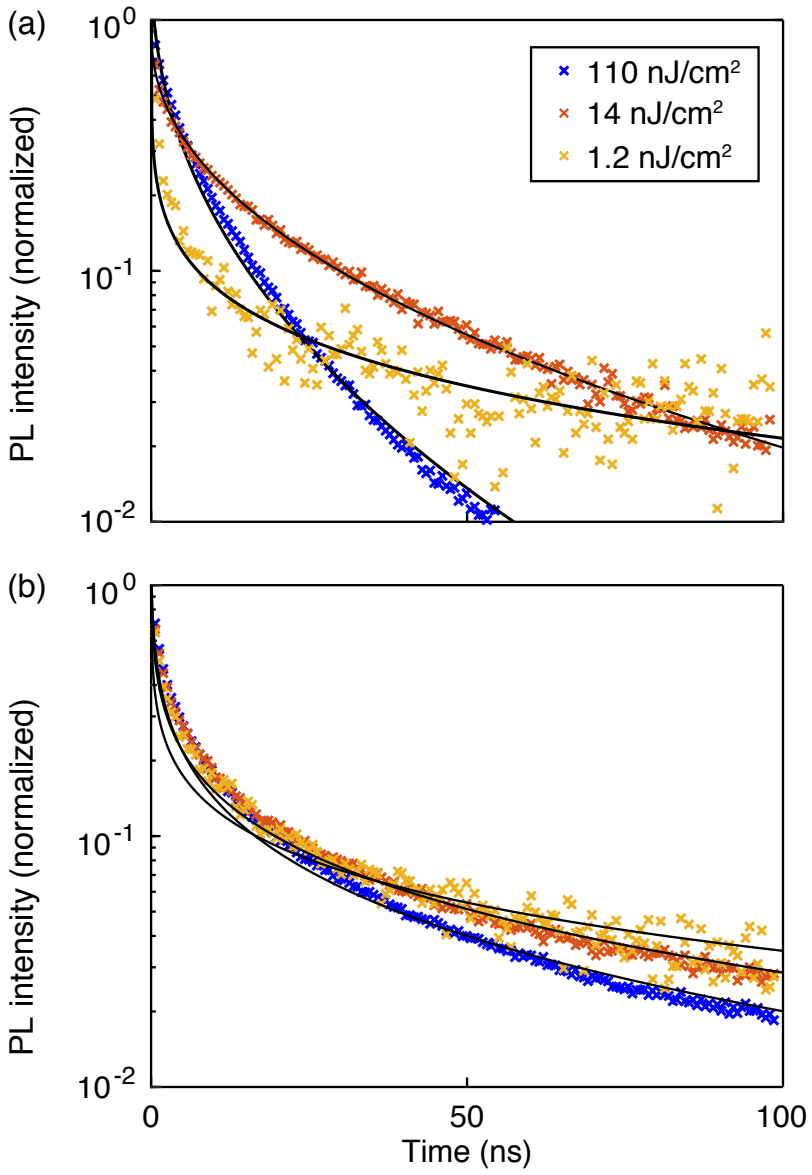

Figure 4.12: TRPL spectra of the $MAPbI_3$ (a) thin film and (b) single crystal within the initial 100 ps. The experimental data were taken and analyzed by Dr. Adam Wright.

The diffusion coefficient is calculated by Equation (2.3) where the electrical mobility is extracted from the peak of the photoconductivity decay dynamics shown in Figure 4.8. Equation (2.2) is then fitted globally to the photoconductivity decay dynamics, from which the bimolecular recombination rate k_2 is found to be $2.6\times10^{-10}\,\mathrm{cm^3s^{-1}}$ for the thin film and $8.7\times10^{-10}\,\mathrm{cm^3s^{-1}}$ for the single crystal.

In contrast, the bimolecular recombination rates extracted from the simple model which is obtained by fitting Equation (2.1) to the photoconductivity decay dynamics instead, show a huge difference between the $MAPbI_3$ thin film and single crystal, as listed in Table 4.1. In addition, it can also be seen from Figure 4.13 that the theoretical fit does not agree well with the experimental data, especially for $MAPbI_3$ single crystal. This is because the single crystal is much thicker than the thin film, which makes the effect of photon reabsorption much more significant and the neglect of photon reabsorption can lead to inaccurate analysis of the charge-carrier dynamics. In particular, as pointed out by Crothers *et al.* [71], photon reabsorption can mask the intrinsic charge-carrier recombination rate significantly, which makes the simple model governed by Equation (2.1) invalid for thick samples such as single crystal.

	Photon reabsorption	No photon reabsorption
k_1 ($\mathrm{s^{-1}}$)	$k_{1,\mathrm{film}} = 8.3\times10^{7}$	
(extracted from TRPL)	$k_{1,\mathrm{crystal}} = 5.3\times10^{6}$	
$k_{2,\mathrm{film}}$ ($\mathrm{cm^3s^{-1}}$)	2.6×10^{-10}	1.17×10^{-9}
$k_{2,\mathrm{crystal}}$ ($\mathrm{cm^3s^{-1}}$)	8.7×10^{-10}	3.65×10^{-11}
k_3 ($\mathrm{cm^6s^{-1}}$)	0	0

Table 4.1: Comparison of charge-carrier recombination parameters extracted from the photoconductivity decay dynamics using the photon-reabsorption model (Equation (2.2)) and the simple model (Equation (2.1)). The photon-reabsorption modelling for extracting k_2 was performed by Dr. Timothy Crothers.

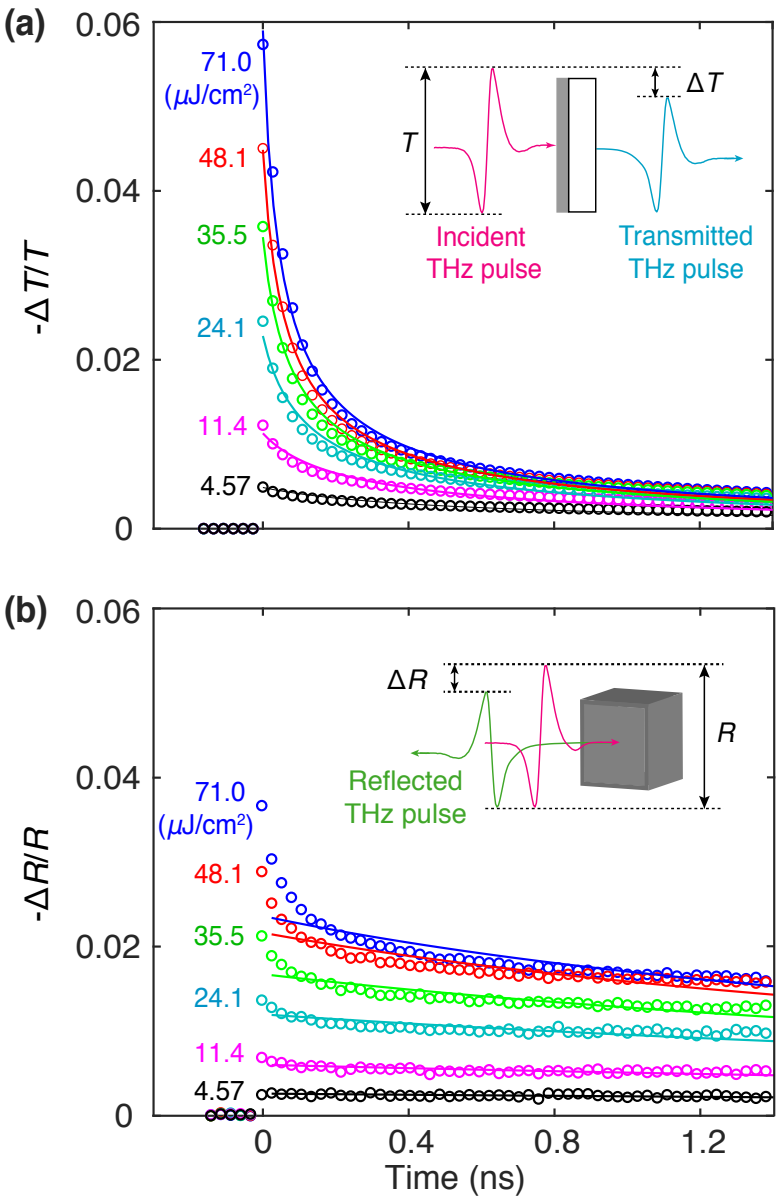

Figure 4.13: Photoconductivity decay dynamics at room temperature of $MAPbI_3$ (a) thin film measured in transmission and (b) single crystal measured in reflection. The circles represent the experimental data identical to what is shown in Figure 4.8. The curves represent the theoretical fits obtained from the simple model governed by Equation (2.1) which agree less well with the experimental data than the fits obtained from the photon-reabsorption model shown in Figure 4.8.

According to Equation (2.4), the charge-carrier diffusion length depends on the total recombination rate $R(n)$ which can change significantly depending which carrier dynamics model is applied. Therefore, the diffusion lengths extracted from the photon-reabsorption model and the simple model are compared to show that the simple model can significantly overestimate the true diffusion length, especially for the single crystal.

Figure 4.14 shows the carrier diffusion length as a function of carrier density n of $MAPbI_3$ thin films and single crystals calculated at a few different values of k_1. Since the radiative bimolecular recombination rate k_2 is intrinsic to the material, it is fixed at the values given in Table 4.1. Auger recombination is again neglected. The electrical mobilities of thin film and single crystal are 33 and $59\,\mathrm{cm^2V^{-1}s^{-1}}$ respectively at room temperature. It is worth noting that at high carrier density ($n > 10^{14}\,\mathrm{cm^{-3}}$), the carrier diffusion length changes significantly with the carrier density especially as k_1 approaches zero. Therefore, it is important to evaluate the carrier diffusion length at a reasonable carrier density especially in the case of low trap-density regime. Here, the diffusion length is calculated under 1 sun illumination ($1\,\mathrm{kW/m^2}$ AM1.5-filtered), which is the usual operating condition for perovskite solar cells. In this case, the carrier density at a certain value of k_1 is indicated by the arrows denoted as $n_{\mathrm{AM1.5}}$ in Figure 4.14. According to Ref. 67, under 1 sun illumination with the assumption of no charge extraction, this specific carrier density $n_{\mathrm{AM1.5}}$ can be estimated by setting $\partial n/\partial t = 0$ in Equation (2.2). The Auger recombination k_3 and the diffusion term $D(\partial^2 n/\partial z^2)$ are neglected for a simplistic approximation. The resultant quadratic equation is then solved with the knowledge of charge-carrier generation rate G' (or G in the simple model) which is determined from

$$G' = \frac{1}{hc}\int f_{\mathrm{solar}}(\lambda)\alpha(\lambda)e^{-\alpha(\lambda)z}\lambda d\lambda, \tag{4.2}$$

where h is the Plank constant, c is the speed of light in vacuum, z is the film depth and $\alpha(\lambda)$ is the absorption coefficient of $MAPbI_3$ at wavelength λ. f_{solar} is the ASTM G173-03 Global Tilt reference spectrum for the solar spectral irradiance distribution, which satisfies $\int f_{\text{solar}}(\lambda)d\lambda = 1\,\text{kW/m}^2$. An average value $\langle G' \rangle = 4 \times 10^{21}\,\text{cm}^{-3}\text{s}^{-1}$ is extracted for a typical $MAPbI_3$ thin film [67]. Using the bimolecular recombination rate k_2 given in Table 4.1, the carrier density under 1 sun illumination ($n_{\text{AM1.5}}$) is plotted as a function of k_1, which is shown in Figure 4.15 for (a) the photon-reabsorption model and (b) the simple model respectively, where a large discrepancy in $n_{\text{AM1.5}}$ can be seen between those two models. Consequently, the carrier diffusion length calculated using the simple model deviates from that calculated from the photon-reabsorption model, as shown in Figure 4.16, where the arrows indicate the different positions of $n_{\text{AM1.5}}$ extracted from the simple model.

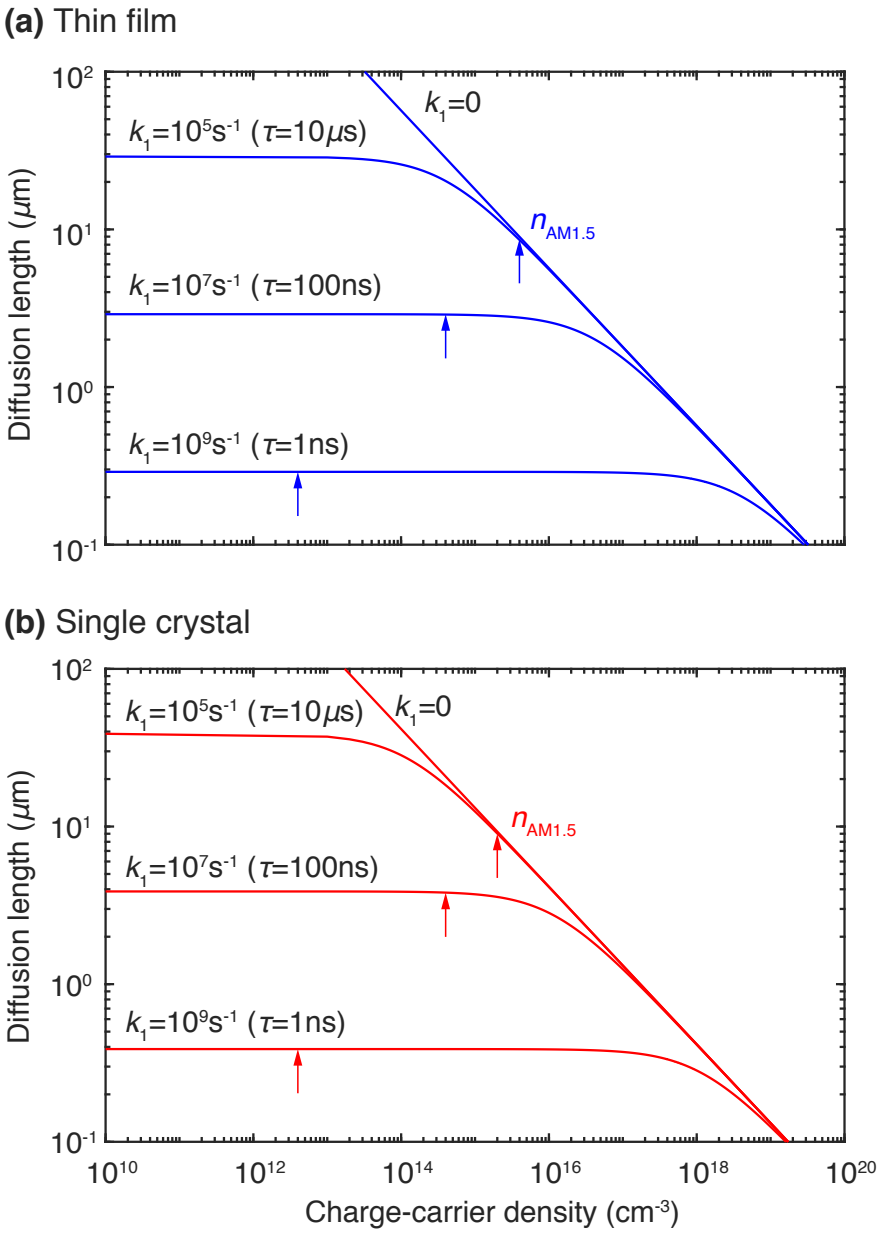

Figure 4.14: Carrier diffusion length calculated using the photon-reabsorption model as a function of carrier density for $MAPbI_3$ (a) thin film and (b) single crystal. The arrows indicate the diffusion length calculated under 1 sun illumination.

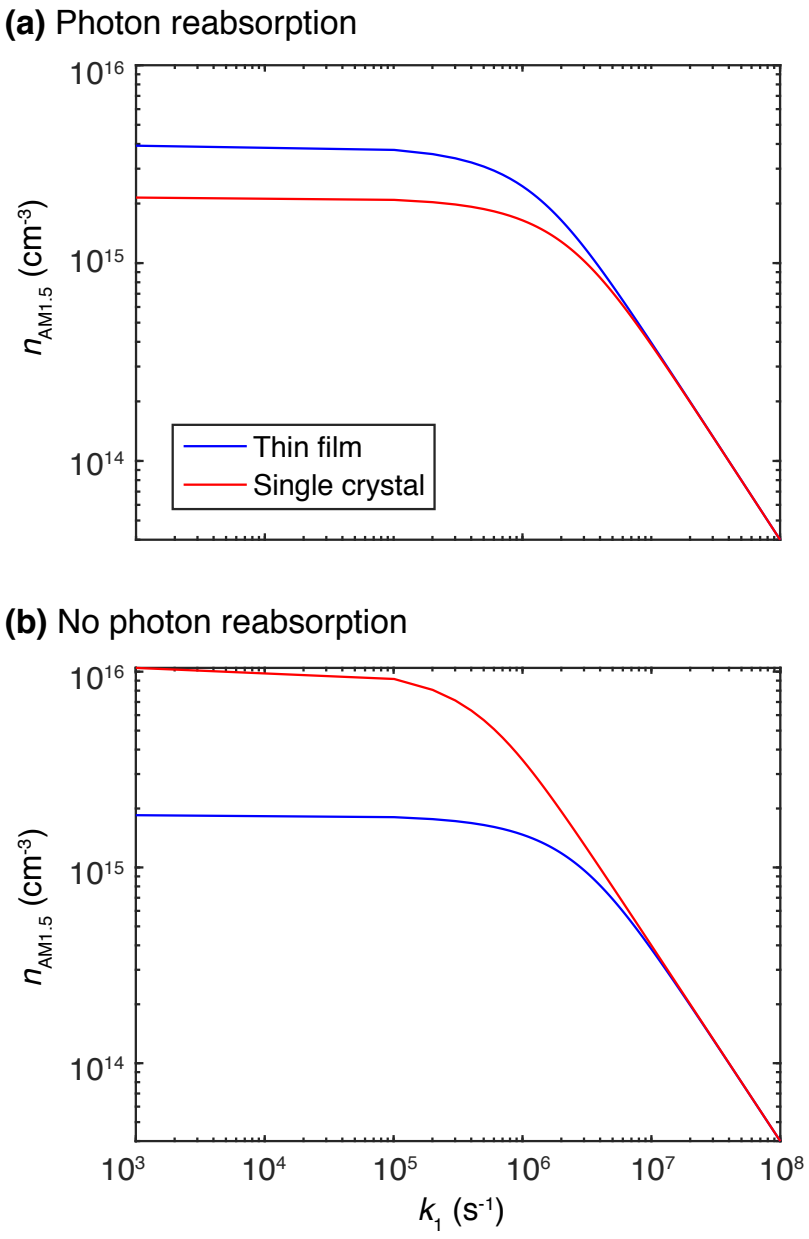

Figure 4.15: Charge-carrier density under 1 sun illumination ($n_{\mathrm{AM1.5}}$) as a function of k_1 calculated from (a) the photon-reabsorption model and (b) the simple model. The blue and red curves represent the results for $MAPbI_3$ thin film and single crystal respectively.

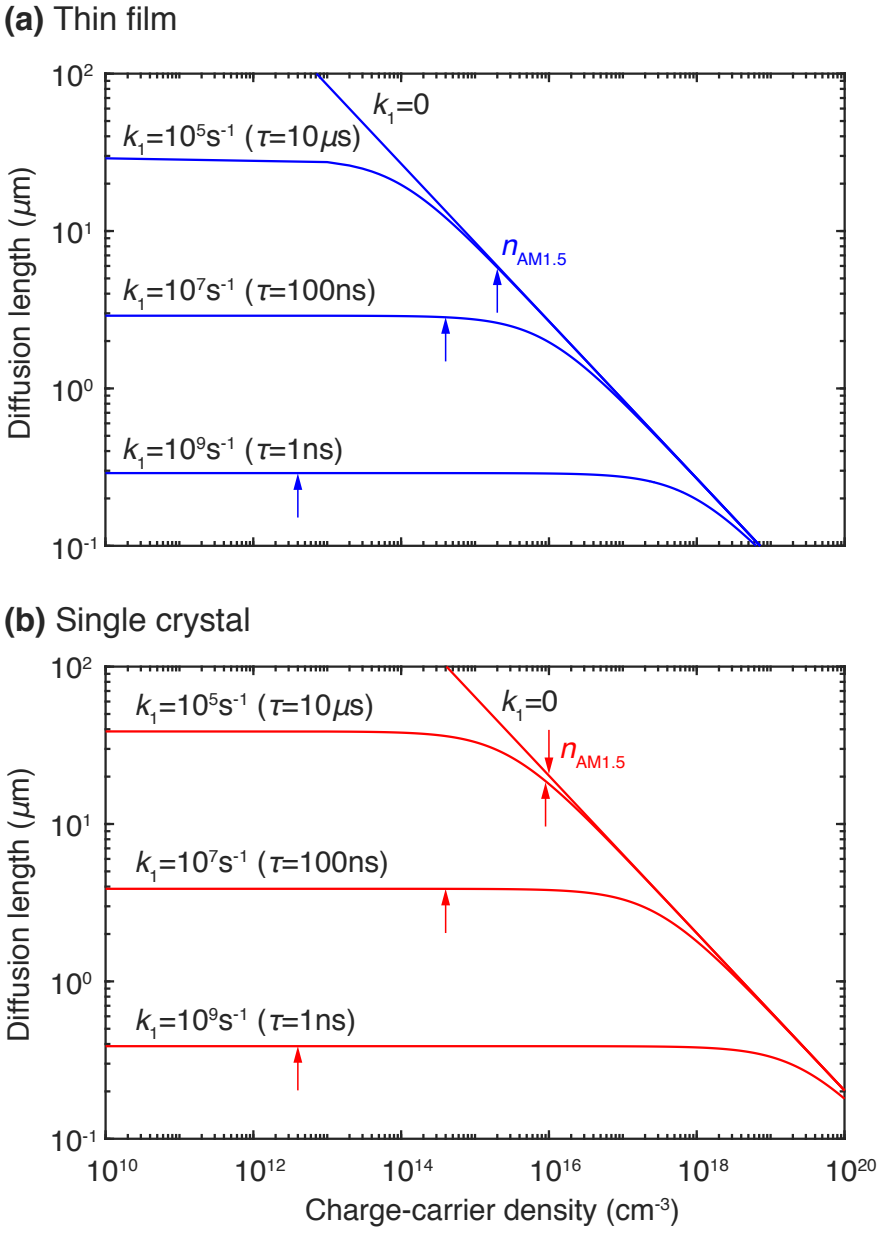

Figure 4.16: Carrier diffusion length calculated by the simple model for $MAPbI_3$ (a) thin film and (b) single crystal. The arrows indicate the diffusion length under 1 sun illumination.

Table 4.2 lists the specific diffusion lengths of $MAPbI_3$ thin film and single crystal calculated from the photon-reabsorption model and the simple model under 1 sun illumination with different values of k_1. When $k_1 = 0$, there is no trap-mediated monomolecular recombination, which is the case for an ideal pure material. The diffusion length obtained from the photon-reabsorption model is the same for $MAPbI_3$ thin film and single crystal, which is consistent with the assumption that the diffusion length is intrinsic to the material when there is no impurity or trap. In contrast, the simple model significantly overestimates the diffusion length of the single crystal. In a more realistic case, the diffusion length is calculated using the values of k_1 extracted from the TRPL measurement, as listed in the second row. Again, the simple model shows an overestimate of the true diffusion length for the $MAPbI_3$ single crystal, although no difference is shown for the thin film, since the effect of photon reabsorption is much less significant.

	Photon reabsorption	No photon reabsorption
	$k_1 = 0$	
$L_{\mathrm{D,film}}$ (μm)	9.1	6.2
$L_{\mathrm{D,crystal}}$ (μm)	9.1	20
TRPL	$k_{1,\mathrm{film}} = 8.3 \times 10^7\,\mathrm{s}^{-1}$ $k_{1,\mathrm{crystal}} = 5.3 \times 10^6\,\mathrm{s}^{-1}$	
$L_{\mathrm{D,film}}$ (μm)	1.0	1.0
$L_{\mathrm{D,crystal}}$ (μm)	5.0	5.3

Table 4.2: Comparison of carrier diffusion length calculated from the photon-reabsorption model and the simple model under 1 sun illumination. In the first row, both $MAPbI_3$ thin film and single crystal are assumed to be pure so that $k_1 = 0$, whereas in the real case (second row), k_1 is extracted from the TRPL measurement, which gives a better indication of the diffusion length.

4.5 Summary

In conclusion, this is a comprehensive experimental and theoretical study of the electrical properties of single-crystal and polycrystalline $MAPbI_3$. The large discrepancy in previously published values of key figures of merit such as mobility, diffusion length and recombination rates is reconciled by including the effects of photon reabsorption. In particular, it is found that neglecting photon reabsorption when modelling thick single crystals leads to a significant overestimate of diffusion lengths.

The experimental data agree extremely well with *ab initio* Boltzmann transport calculations when the Fröhlich interaction of multiple phonon modes are included. This result explains the overestimation of mobility in previous calculations where only one phonon branch was included. The BTE model provided excellent agreement with single-crystal mobility data without any fitting parameters. However, the measured mobility of polycrystalline thin films deviated from the single-crystal data and the BTE model. It is found that grain-boundary scattering accounts for this deviation and is thus included in the BTE model. While the mobility of polycrystalline films is primarily limited by grain-boundary scattering at cryogenic temperatures, the room-temperature mobility is found to be dominated by LO-phonon scattering. As such the mobility only drops from $59\,\mathrm{cm^2V^{-1}s^{-1}}$ in the single crystal to $33\,\mathrm{cm^2V^{-1}s^{-1}}$ for the polycrystalline $MAPbI_3$ indicating the benign nature of these grain boundaries at room temperature.

Overall this study provides a complete picture of the fundamental electrical properties of the model MHP $MAPbI_3$ in both single-crystal and polycrystalline morphologies. Therefore, the apparently contradictory previous experimental and theoretical studies are unified. The results indicate the polycrystalline thin films possess similar performance to single crystals at the usual operating temperature of electronic devices. This is promising for future applications of MHP thin films, and for upscaling of devices such as solar cells and lighting panels.

Chapter 5

Phonon Hardening Observed in $MAPbI_3$ Single-Crystal and Thin-Film Perovskites

5.1 Introduction

As have been discussed in the previous chapter, the temperature-dependent charge-carrier mobility of $MAPbI_3$ single crystals and polycrystalline thin films show that the dominant limiting factor of the carrier mobility in MHPs is the LO-phonon scattering (Fröhlich interaction). To understand the effect of optical phonons on the optoelectronic properties of MHPs in more depth, this chapter will discuss the behaviors of phonon modes in $MAPbI_3$ single crystals and thin films at THz frequencies.

The phonon modes, arising from lattice vibrations, have an intimate relationship with the optoelectronic properties of MHPs. For instance, homogeneous line broadening of the PL spectrum has been observed in lead-halide perovskite thin films, which is attributed to the phonon coupling effect [191]. A temperature-dependent study of the PL on four types of formamidinium and methylammonium perovskites includ-

ing $MAPbI_3$ also demonstrates the LO-phonon scattering as the dominant source for electron-phonon coupling at room temperature, which contributes to the emission line broadening [137]. Moreover, various Raman and infrared spectroscopy studies have been performed on $MAPbI_3$ covering the spectrum range from 30 to 3700 cm^{-1}, from which the phonon absorption peaks are assigned to the internal vibrations of the MA cations, the cation librations or the internal vibrations of the PbI_3 framework [192–196]. Meanwhile, some computational studies based on the first-principles calculations have also been conducted on $MAPbI_3$ in the low-temperature regime (orthorhombic phase), which assign different lattice vibration modes to certain frequency ranges [89, 111].

However, there are few studies investigating the difference between $MAPbI_3$ single crystals and polycrystalline thin films in terms of their phonon modes and the corresponding effect on charge-carrier transport. Due to the significant difference in the temperature-dependent behavior of the mobility in $MAPbI_3$ single crystal and thin film, it is important to compare their phonon modes systematically, so that a deeper understanding about the limiting factors of carrier transport may be gained. Therefore, in this work, THz conductivity measurements were performed on the $MAPbI_3$ thin films to identify their phonon modes at THz frequencies. The spectra were measured at temperatures ranging from 5 to 295 K covering the orthorhombic and tetragonal phases. Meanwhile, the phonon modes of the $MAPbI_3$ single crystal were identified by measuring the THz reflectivity spectra, since the single crystal is too thick for the THz pulse to transmit through. In order to compare the phonon modes between the single crystal and the thin film, the reflectivity and the conductivity spectra were converted to absorption spectra, from which multiple phonon peaks below 2 THz were observed with the prominent ones assigned as Pb–I stretching mode. In addition, to demonstrate the electron-phonon coupling effect in $MAPbI_3$, OPTPS was utilized to measure the photoconductivity spectrum via the introduction of photo-

excitation. While both the $MAPbI_3$ single crystal and thin film showed a Drude-like photoconductivity response, stronger phonon modulation of the Drude response was observed in the single crystal, indicating a stronger electron-phonon coupling effect.

Furthermore, under photo-excitation the phonon modes were found to shift to higher frequencies, which is attributed to the increase in dielectric screening. The first-principles calculations predict similar phonon hardening behavior by applying the combined effect of hole and electron doping to simulate the photo-excitation condition. In the last few years, various studies on MHPs have demonstrated the effect of photon-lattice coupling on the lattice structural change. For example, photostrictive response under visible light illumination has been observed in $MAPbI_3$ and $MAPbBr_3$, which is attributed to the disordered orientation of the organic molecules [197, 198]. Whilst this photostrictive effect happens on a timescale ranging from a few seconds to days, the phonon hardening effect observed in the OPTPS measurement occurs at a much faster timescale (less than 5 ps), which suggests it is an electronic process. Further investigations of this novel phenomenon can lead to better understanding of the optoelectronic properties of $MAPbI_3$ perovskites, which will help to improve the photovoltaic performance of perovskite-based devices.

5.2 Methods

In this study, THz spectroscopy measurements were performed on the same $MAPbI_3$ thin film and single crystal samples which were used in Chapter 4 with sample details given in Section 4.2. THz-TDS and OPTPS were utilized to investigate the characteristics of the phonon modes of $MAPbI_3$ using the data analysis methods described in Sections 3.1.3.2 and 3.1.3.3. DFT calculations were performed by Dr. Samuel Poncé to compute the phonon modes of $CsPbI_3$ as a cubic approximation for $MAPbI_3$ since it is less computationally expensive. The QUANTUM ESPRESSO package [177] was

used for simulating electron and hole doping densities between 10^{17}–$10^{19}\,\mathrm{cm}^{-3}$, which corresponds to the charge-carrier density generated by photo-excitation in the THz spectroscopy measurements. Slightly different from the simulation parameters used in Chapter 4, the phonons were calculated using DFT with a dense $16 \times 16 \times 16$ **k**-point grid and a $8 \times 8 \times 8$ **q**-point grid to achieve better accuracy. A higher plane-wave kinetic energy cutoff of 150 Ry was employed and the exchange self-energy and the polarizability were evaluated using cutoffs of 60 Ry and 15 Ry respectively. The summations over empty states was performed using 500 bands for the calculation of the polarization and 600 bands for the Green's function. The Brillouin zone was sampled via a $8 \times 8 \times 8$ unshifted grid and the termination scheme of Ref. 181 was employed to accelerate the convergence with respect to the number of empty states. The electron-phonon matrix elements were interpolated from coarse $8 \times 8 \times 8$ **k**/**q**-point grids to a dense R-centered Cauchy grid for phonons with 105,000 points using the EPW code [182] of the QUANTUM ESPRESSO distribution in conjunction with the wannier90 library [183]. Spin-orbit coupling was included in all calculations.

5.3 Results and Discussions

5.3.1 Phonon Modes Observed at THz Frequencies

To investigate the behavior of phonon modes of the $MAPbI_3$ single crystal and thin film in different lattice structural phases, the conductivity spectra of the thin film and the reflectivity spectra of the single crystal were measured by THz-TDS in transmission mode and reflection mode respectively. The (dark) conductivity $\sigma_{\mathrm{dark}}(\omega)$ of the thin film can be calculated directly from the THz transmissivity $T(\omega)$ according to Equation (3.31). In contrast, for the single crystal, the reflectivity spectrum $R(\omega)$ is used for investigating the phonon modes, which is converted to an absorption spectrum using the method of VDF described in Section 3.1.3.3. In order to compare the

phonon modes between the $MAPbI_3$ single crystal and thin film more consistently, the conductivity spectrum of the thin film is also converted into a absorption spectrum, which is shown in Figure 5.1(a).

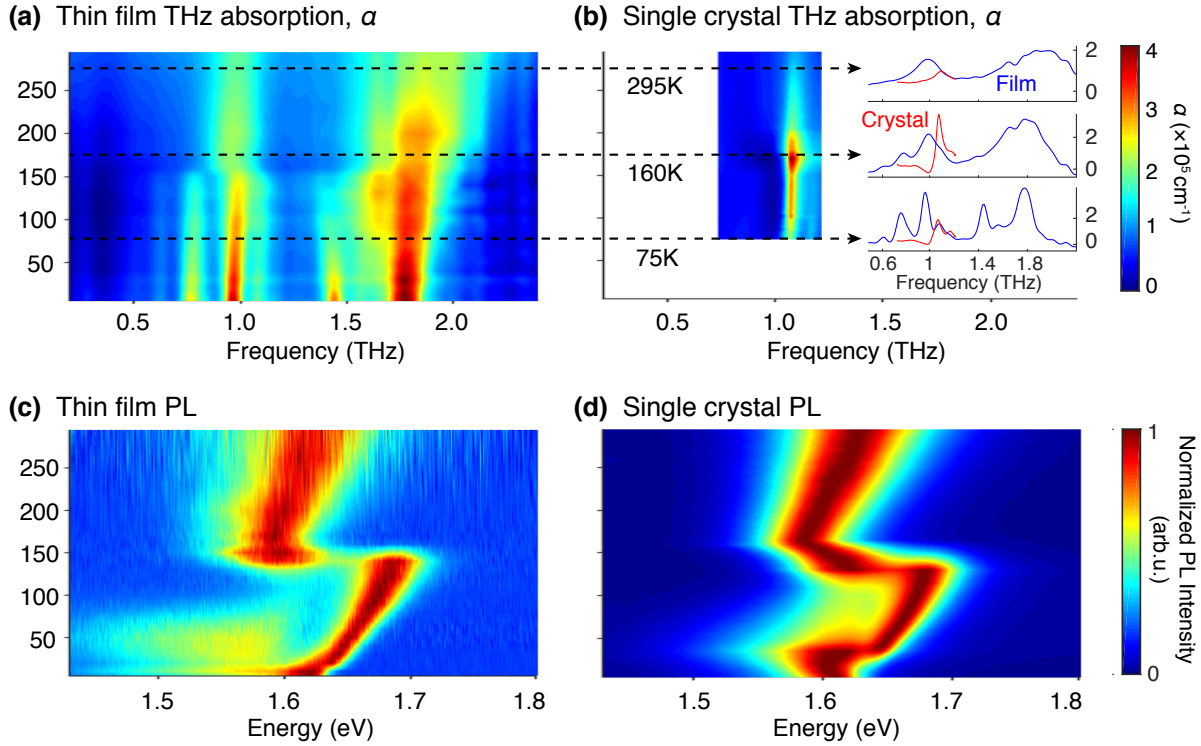

Figure 5.1: Absorption spectra of $MAPbI_3$ (a) thin film and (b) single crystal measured by a cold-finger cryostat in transmission and reflection respectively. The inset demonstrates a comparison in absorption between the thin film and single crystal at 75, 160 and 295 K. PL spectrum of the (c) thin film (d) single crystal which was measured by the cold-finger cryostat and the gas-exchange cryostat respectively.

In the process of measuring the conductivity and reflectivity, the $MAPbI_3$ thin film and single crystal were mounted on a cold-finger cryostat, which could change the temperature in the range between 5–300 K. However, due to the ultralow thermal conductivity of $MAPbI_3$ [173], it is extremely challenging for the single crystal to reach low temperature. Therefore, a sapphire substrate was inserted in front of the single crystal to help dissipate the heat generated from the pump beam, which enabled the single crystal to reach a temperature below 80 K. The PL spectra shown in Figure 5.1(d) were used as a reference for determining the real temperature of the sin-

gle crystal (details of this PL-facilitated thermometry are provided in Section 4.3.2). In contrast, since the $MAPbI_3$ thin film was deposited on a quartz substrate, there was no thermal contact issue so that it could reach the lowest temperature at 5 K. Figure 5.1(a) and the inset in Figure 5.1(b) show that four prominent phonon absorption peaks along with three minor peaks are observed in the thin film at temperature below 75 K, which gradually broadens as the temperature increases. As reported by Weller *et al.* [199] the positional disorder of the MA cation increases with temperature from 100 to 352 K and above the phase transition at 160 K, orientational disorder of the organic cation also comes into play, which enhances the dynamic disorder further. This is considered as the major source for the phonon broadening at higher temperature, which happens at a picosecond timescale [200]. When the thin film has reached room temperature, the phonon modes have broadened so much that they merge into two remaining phonon peaks. Figure 5.1(c) displays the PL spectrum of the thin film measured at temperatures between 5–300 K and an abrupt redshift in the peak wavelength is observed at 160 K, which is consistent with the phase transition reported previously on $MAPbI_3$ thin films [38].

Similar phonon broadening effect is observed in the $MAPbI_3$ single crystal as shown by the red curves in Figure 5.1(b), although the absorption spectra were only measured over a restricted frequency domain owing to the poorer SNR of the reflection measurement. In addition, although the extra sapphire substrate inserted in front of the single crystal can help the single crystal to reach low temperature, the position of the single crystal might move slightly due to the contraction or expansion of the sample holder when the temperature changes. At different temperatures, the THz pulse is not necessarily focused on the exactly same spot of the single crystal. As a result, an abrupt increase of phonon intensity is observed in the single crystal at 160 K, which is attributed to experimental artefacts.

To compare the phonon modes between the single crystal and the thin film more

quantitatively, a Lorentzian oscillator was fitted to each phonon peak, from which the exact phonon wavenumbers $\tilde{\nu}_{\mathrm{TO}}$ and scattering rates γ_{TO} were extracted as listed in Table 5.1. According to the first-principles calculations performed by Pérez-Osorio *et al.* [89] the most prominent phonon peaks observed in the $MAPbI_3$ thin film with $\tilde{\nu}_{\mathrm{TO}} = 31.7$ and $58\,\mathrm{cm}^{-1}$ are assigned to the Pb–I stretching mode of B_u symmetry and liberation/translation mode of the MA cations, respectively. Since in the DFT calculations the MA cation is replaced with a Cs^+ cation, the phonon modes of the MA cation are missing. Hence this study will focus on the Pb–I stretching mode of $MAPbI_3$ only.

		Phonon mode index	1	2	3	4	5	6	7
		Temperature (K)							
Thin film	$\tilde{\nu}_{\mathrm{TO}}$ (cm^{-1})	5	20.7	25.4	31.7	36.0	47.7	52.0	58.0
	$\tilde{\nu}_{\mathrm{LO}}$ (cm^{-1})	5	22.0	27.1	33.8	38.4	50.8	55.4	61.8
	γ_{TO} ($10^{12}\,\mathrm{s}^{-1}$)	5	0.43	0.48	0.30	0.80	0.50	0.50	0.95
	$\tilde{\nu}_{\mathrm{TO}}$	295	-	-	31.7	-	-	-	58.0
	$\tilde{\nu}_{\mathrm{LO}}$	295	-	-	36.2	-	-	-	70.3
	γ_{TO}	295	-	-	1.30	-	-	-	3.50
Single crystal	$\tilde{\nu}_{\mathrm{TO}}$	75	-	27.7	35.3	38.3	-	-	-
	$\tilde{\nu}_{\mathrm{LO}}$	75	-	29.3	40.1	44.3	-	-	-
	γ_{TO}	75	-	0.40	0.20	0.30	-	-	-
	$\tilde{\nu}_{\mathrm{TO}}$	295	-	-	35.3	-	-	-	-
	$\tilde{\nu}_{\mathrm{LO}}$	295	-	-	40.1	-	-	-	-
	γ_{TO}	295	-	-	0.70	-	-	-	-

Table 5.1: Phonon wavenumbers $\tilde{\nu}_{\mathrm{TO}}$ (measured), $\tilde{\nu}_{\mathrm{LO}}$ (calculated from the LST relation) and TO-phonon scattering rates γ_{TO} (extracted from the Lorentzian fit) of the $MAPbI_3$ thin film and single crystal.

Interestingly, as indicated by the inset in Figure 5.1(b) and Table 5.1, the phonon peaks observed in the $MAPbI_3$ single crystal appear to have shifted to higher frequencies. This might be due to some experimental artefacts induced by the reflection measurements, as the reflected THz pulse is much more sensitive to the position

and surface condition of the sample. Even the slightest misalignment may cause the detected THz pulse to be out of focus and lead to some frequency shift in the resultant phonon peaks. Nevertheless, by comparing the relative intensity between those phonon modes observed in the $MAPbI_3$ single crystal to that in the thin film, it is concluded that the dominant phonon in the single crystal ($\tilde{\nu}_{\mathrm{TO}} = 35.3\,\mathrm{cm}^{-1}$) also comes from the Pb–I stretching mode.

Moreover, the TO-phonon scattering rate γ_{TO} was extracted according to the Lorentzian fit to each phonon mode and the increased values of γ_{TO} observed at room temperature is a direct indication of the phonon broadening effect which is attributed to the dynamic disorder of the perovskite lattice structure [125]. The LO-phonon wavenumbers $\tilde{\nu}_{\mathrm{LO}}$ were determined from the LST relation given by Equation (2.15) where the static (low-frequency) dielectric constant $\varepsilon_{\mathrm{stat}}$ and the high-frequency dielectric constant ε_{∞} were extracted from the Lorentzian fit. The small LO-TO splitting of the Pb–I stretching mode is consistent with what was reported previously [89].

5.3.2 Phonon Hardening Arising from Photo-Excitation

In order to investigate the behavior of charge-carrier transport in $MAPbI_3$ single crystal and thin film and its relationship with the phonon modes, the photoconductivity spectrum was measured using OPTPS where an ultrafast (35 fs) optical laser pulse at central wavelength of 400 nm was applied to generate charge carriers. The strength of transmitted/reflected THz electric field decreases due to the presence of photo-induced free charge carriers. Conventionally, the THz photoconductivity measured in transmission is expressed by Equation (3.36),

$$\Delta\sigma(\omega) = -\frac{\varepsilon_0 c(1+\tilde{n_s})}{d}\left(\frac{\Delta T}{T_{\mathrm{off}}}\right),$$

from which some "phonon-modulation" features superimposed on top of the Drude response is attributed to electron-phonon coupling effect [36, 38]. However, a recent study showed that those phonon modulations could be removed by separating the effect of phonon modes observed in the dark conductivity from the measured photoconductivity spectrum [135]. Consequently, a more accurate expression for the photoconductivity is given by Equation (3.35),

$$\Delta\sigma(\omega) = -\frac{\varepsilon_0 c(1+\tilde{n_s})}{d}\left(\frac{\Delta T}{T_{on}}\right)\left(\frac{T_{reference}}{T_{off}}\right).$$

As shown in Figure 5.2(a), the photoconductivity calculated using Equation (3.35) shows a pure Drude response with a flat real part and a negligible imaginary part, which can be described by

$$\Delta\sigma(\omega) = \sigma_{Drude} = \frac{ne\mu}{1 - i\omega\tau}, \tag{5.1}$$

where n is the charge-carrier density determined by the photo-excitation fluence, e is the elementary charge, μ is the electrical mobility and τ is the charge-carrier scattering lifetime. The real and imaginary parts of the Drude response are represented by the blue and red dashed lines respectively as shown in Figures 5.2(a) and 5.2(b).

However, when the photoconductivity of the thin film was measured at low temperature (5 K), the phonon modulations reappeared as demonstrated in Figure 5.2(b). This suggests that although the phonon modulation observed in the photoconductivity spectrum of the $MAPbI_3$ thin film may be removed or suppressed by using Equation (3.35), it does not completely rule out the possibility that electron-phonon coupling may still be present in $MAPbI_3$. Indeed, the electron-phonon coupling effect has been proved by other experimental and theoretical studies using techniques such as temperature-dependent PL measurement [137] and many-body *ab initio* calculations [83]. The significance of using Equation (3.35) to calculate the photocon-

ductivity is that it helps to avoid potential misinterpretation of the carrier-transport behavior due to some experimental artefacts.

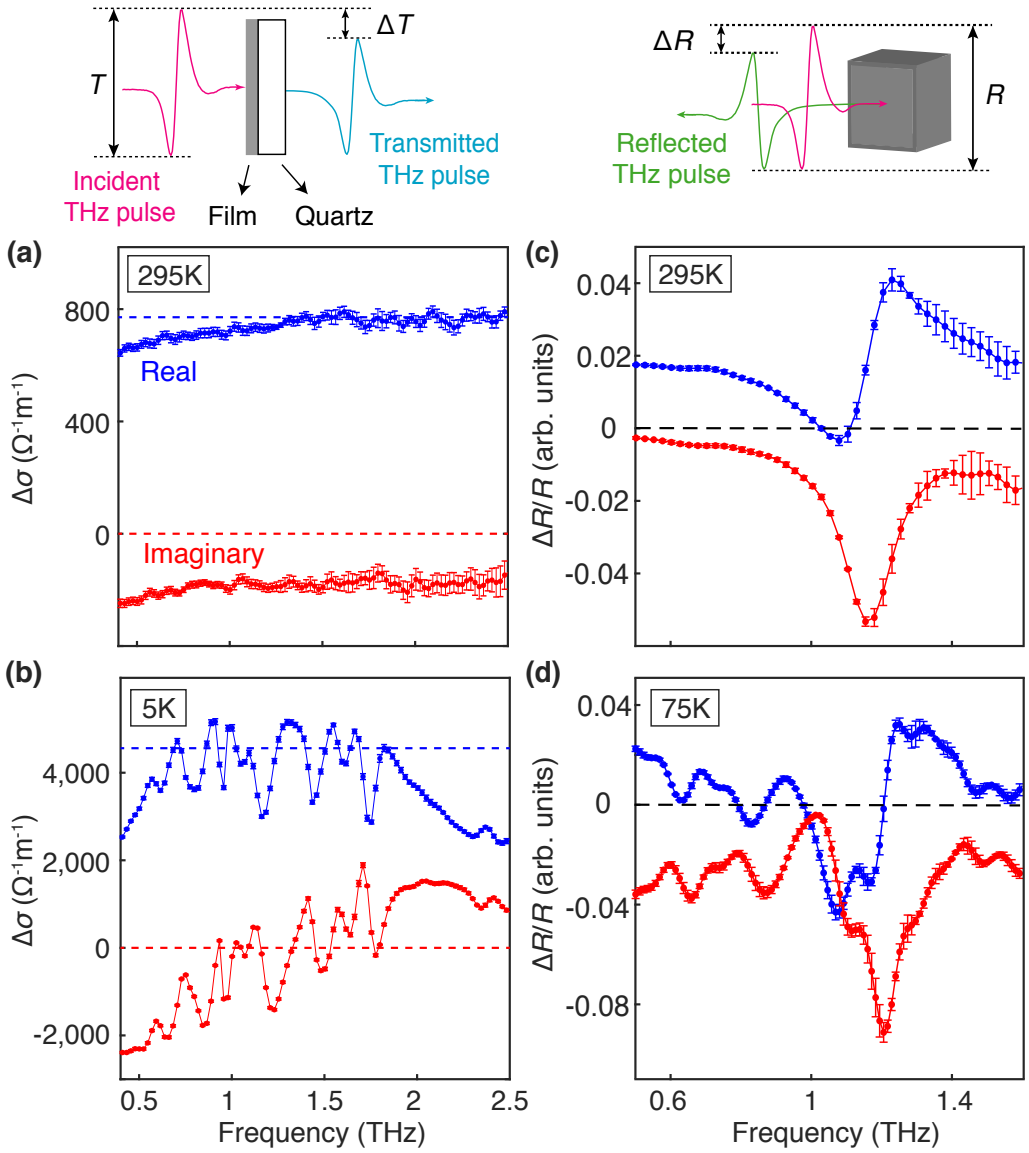

Figure 5.2: Photoconductivity spectra of $MAPbI_3$ thin film measured at (a) 295 K and (b) 5 K in transmission. The blue and red dots represent experimental data of the real and imaginary parts of photoconductivity, whereas the blue and red dashed lines represent the Drude fit. Photoconductivity of $MAPbI_3$ single crystal measured at (c) 295 K and (d) 75 K in reflection. The cartoons demonstrate the geometry of the transmission and reflection setup for the thin film and single crystal measurements respectively. The photoconductivity spectra were taken at 5 ps after photo-excitation under fluence 48 $\mu J/cm^2$.

In the case of $MAPbI_3$ single crystals, since the THz signal was measured in reflection, the photoconductivity is expressed in terms of $\Delta R/R$ instead [129, 131],

$$\Delta\sigma(\omega) = \frac{\varepsilon_0 c\alpha(n_s^2 - 1^2)}{2}\left(1 - i\frac{2\omega n_s}{\alpha c}\right)\left(\frac{\Delta R}{R}\right), \tag{5.2}$$

where α is the absorption coefficient of $MAPbI_3$ at 400 nm and n_s is the refractive index of the $MAPbI_3$ sample at THz frequencies. $\Delta R = R_{on} - R_{off}$ is the difference in reflected THz electric field between photo-excitation and no-photo-excitation scenarios. In contrast to Equation (3.35), this expression is less straightforward to apply due to the complexity arising from the potential phase change of THz pulse upon reflection and the extra sapphire substrate that is inserted in front of the single crystal to improve the thermal contact. Fortunately, according to the TFA which is also valid for the case of $MAPbI_3$ single crystal, the photoconductivity of $MAPbI_3$ single crystal is linearly proportional to $\Delta R/R$ and therefore in Figures 5.2(c) and 5.2(d), $\Delta R/R$ is plotted as a simplified representation of the photoconductivity.

It is worth noting that the photoconductivity of $MAPbI_3$ single crystal shows a derivative-like feature near the dominant phonon peak ($\sim$1.1 THz), which is attributed to a blueshift in phonon frequency superimposed on the Drude response,

$$\begin{aligned}\Delta\sigma(\omega) &= \sigma_{\text{photoexcitation}}(\omega) - \sigma_{\text{dark}}(\omega)\\ &= [\sigma_{\text{dark}}(\omega + \Delta\omega) + \sigma_{\text{Drude}}] - \sigma_{\text{dark}}(\omega)\\ &= \sigma_{\text{Drude}} + \frac{d\sigma_{\text{dark}}}{d\omega}\Delta\omega,\end{aligned} \tag{5.3}$$

where the dark conductivity σ_{dark} characterizes the phonon modes and the frequency-shift term $\frac{d\sigma_{\text{dark}}}{d\omega}\Delta\omega$ resembles the shape of the real part shown in Figure 5.2(c). Similar effects was observed in formamidinium perovskite thin films [201] and $MAPbI_3$ nanocrystals [202], where a combined model of Drude-Smith and peak-shift contributions was applied [201], and the photoconductivity spectrum was found to be sensi-

tive to both the phonon oscillator strength and the resonant frequency. Such change of phonon profile was claimed to come from the ionic displacement under photo-excitation according to the ultrafast electron diffraction measurement of $MAPbI_3$ thin film [93] and the anharmonic electron-phonon coupling predicted by DFPT [203]. In this study, DFT calculations of the phonon modes were performed on $CsPbI_3$. $CsPbI_3$ may be used as a simple representation for $MAPbI_3$ where the photo-excitation condition was simulated via electron and hole doping. Details of the computational results will be discussed in Section 5.3.3.

In order to demonstrate the phonon-shift phenomenon in $MAPbI_3$ more clearly, the conductivity (and reflectivity) spectrum under photo-excitation and no-photo-excitation scenarios are plotted separately, as shown in Figure 5.3. In panel (c), a clear blueshift of phonon frequency is observed in the reflectivity spectrum of $MAPbI_3$ single crystal measured at 75 K, which is indicated by the black arrows. In addition, a slight enhancement of the phonon strength is also observed, which is consistent with the peak-shift model described in Ref. 201. In contrast, the blueshift in $MAPbI_3$ thin film is much less noticeable, which might be due to the weaker electron-phonon coupling effect and the change of phonon frequency induced by dielectric screening is therefore less significant.

Furthermore, the blueshift in the single crystal measured at 295 K (Figure 5.3(d)) becomes less obvious due to the effect of phonon broadening, which makes the shifted phonon peak less well resolved and hence less prominent. Meanwhile, no blueshift was observed in the thin film at 295 K, owing to the weaker electron-phonon coupling effect, whereas the persistent phonon-shift effect observed in the $MAPbI_3$ single crystal suggests that it has a stronger electron-phonon coupling effect than its thin film counterpart. This is attributed to the longer phonon lifetimes observed in the $MAPbI_3$ single crystal as shown in Table 5.1 where $\gamma_{\text{crystal}} < \gamma_{\text{film}}$. Consequently, although the single crystal has the advantage of having no grain boundaries to achieve higher elec-

trical mobility, its stronger electron-phonon coupling on the other hand suppresses the mobility. Therefore, the electrical mobility of the $MAPbI_3$ single crystal is only moderately higher than that of the thin film as demonstrated by Figure 4.9(a) in Chapter 4.

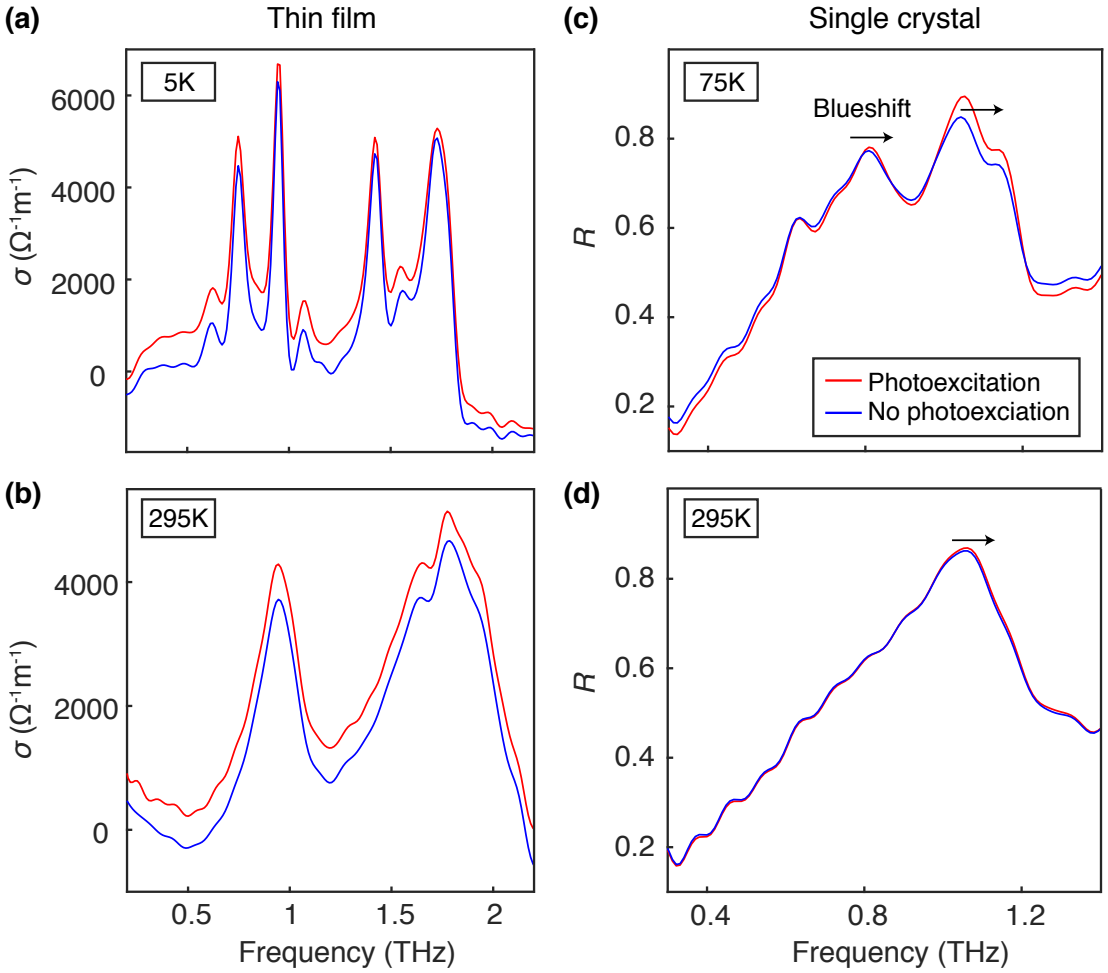

Figure 5.3: Conductivity spectra of $MAPbI_3$ thin film measured at (a) 5 K and (b) 295 K. Reflectivity spectrum of $MAPbI_3$ single crystal measured at (c) 75 K and (d) 295 K. The blue curves represent the measurements taken without photo-excitation and the red curves represent the measurements taken at 5 ps after photo-excitation under fluence 48 $\mu J/cm^2$.

5.3.3 Theoretical Investigations of Phonon Hardening

The blueshift of phonon frequency in $MAPbI_3$ has be investigated by various studies, according to which the common conclusion is that the blueshift arises from a lattice structural change [93, 94]. However, since the THz spectroscopy measurement is performed on an ultrafast timescale (on the order of a few picoseconds), such phonon hardening effect is unlikely to originate from nuclear reorientation/motion/displacement but an electronic process. Here, DFT calculations were performed using pseudopotentials and planewaves to calculate phonons, while including spin-orbit coupling. The MA cation was replaced with a Cs^+ cation to reduce the computational cost and the computed many-body electronic band structure of $CsPbI_3$ is shown in Figure 5.4 with a bandgap of 0.86 eV. To simulate the photo-excitation condition applied in the OPTPS measurements, a rigid band approximation was used to compute the sum of electron and hole doping densities, which neglected the electron-hole interactions. The calculations include the effect of temperature through the non-adiabatic phonon self-energy and spectral function [82], which is exemplified in Figure 5.5 with electron doping density of $10^{17}\,cm^{-3}$.

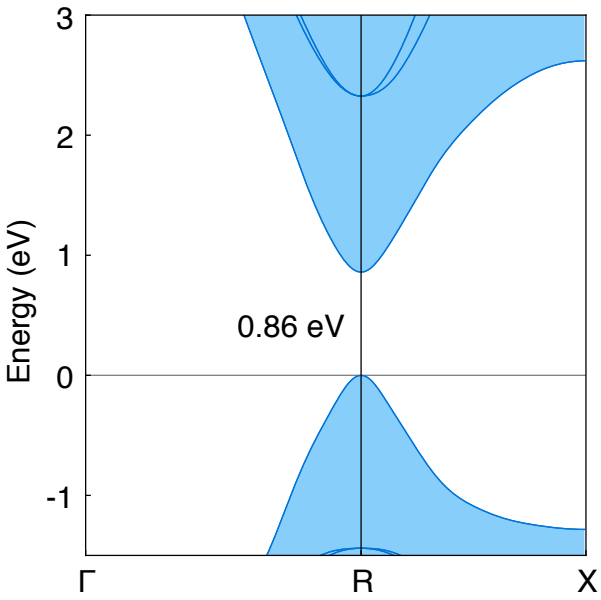

Figure 5.4: Many-body electronic band structure of $CsPbI_3$ using lattice parameter $a = 6.276\,\text{Å}$, calculated by Dr. Samuel Poncé.

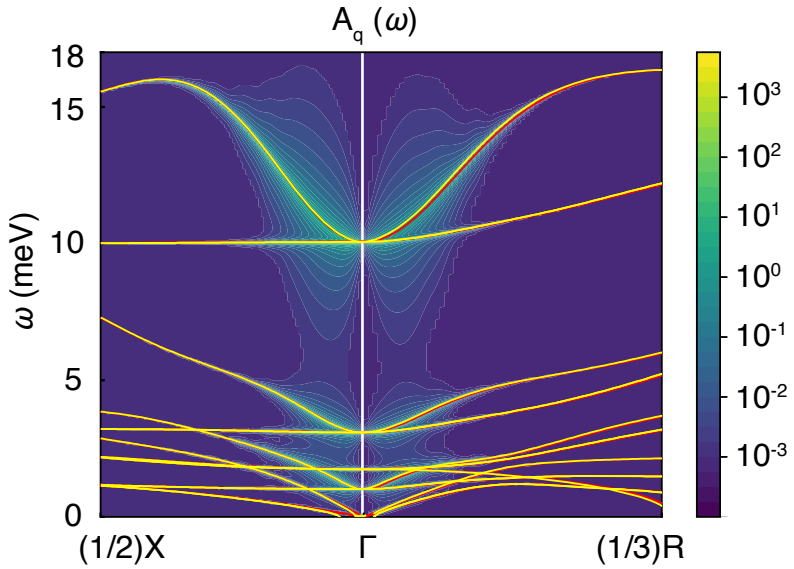

Figure 5.5: Non-adiabatic spectral function with $10^{17}\,\text{cm}^{-3}$ electron doping of $CsPbI_3$ at 300 K using $a = 6.276\,\text{Å}$ lattice parameter, calculated by Dr. Samuel Poncé. The yellow lines are the non-adiabatic renormalized phonon frequencies $\Omega_{\mathbf{q},\nu}$ and the red lines are the DFPT adiabatic phonon frequencies $\tilde{\nu}_{\mathbf{q},\nu}$.

Table 5.2 lists a few representative phonon modes obtained from the DFT calculations of $CsPbI_3$ under conditions of undoped, hole doping density $10^{17}\,cm^{-3}$ and electron doping density $10^{17}\,cm^{-3}$. The highest TO mode with $\tilde{\nu}_{TO} = 81\,cm^{-1}$ corresponds to the Pb–I stretching mode, which exhibits a phonon hardening effect at electron/hole doping density of $10^{17}\,cm^{-3}$.

	Highest TO Pb-I stretching $\tilde{\nu}_{TO}(cm^{-1})$	Mid-TO Pb-I-Pb bending $\tilde{\nu}_{TO}(cm^{-1})$	Mid-TO A-site displacement $\tilde{\nu}_{TO}(cm^{-1})$
Undoped	81.0186	27.4562	13.4219
h^+ doping $10^{17}\,cm^{-3}$	81.1353	24.8777	14.0419
e^- doping $10^{17}\,cm^{-3}$	81.2164	23.8275	13.4742

Table 5.2: Renormalization of the highest TO mode (1st column), mid-TO modes 10–11 (2nd column) and mid-TO modes 7–8 (3rd column) calculated at the zone center at temperature 300 K (unit: cm^{-1}). Calculation performed by Dr. Samuel Poncé.

Since the dominant phonon observed in $MAPbI_3$ is also assigned to Pb–I stretching mode, the highest TO mode calculated for $CsPbI_3$ is regarded as the representative phonon for $MAPbI_3$ at THz frequencies. To simulate the photo-excitation condition in the OPTPS measurement, the experimental photo-excitation is approximated as the sum of electron and hole doping, neglecting electron-hole interactions. As a result, a phonon hardening is computed at 0.3145, 0.5647 and $0.6446\,cm^{-1}$ for the highest TO mode at 10^{17}, 10^{18} and $10^{19}\,cm^{-3}$ doping densities respectively, which is listed in Table 5.3 along with the results obtained for the mid-TO modes. The phonon hardening observed in the Pb–I stretching mode is consistent with the $MAPbI_3$ single crystal measurement where the effect is approximately $0.33\,cm^{-1}$ at photo-excitation fluence $48\,\mu J/cm^2$. Knowing the absorption coefficient of $MAPbI_3$ at 400 nm, the photo-induced charge-carrier density is approximated as $10^{19}\,cm^{-3}$. The small difference in the magnitude of phonon hardening between the experiment and the theory at this specific doping density is likely to come from some experimental error due to the

limited spectral resolution of the OPTPS measurement. On the other hand, although the Pb–I–Pb bending mode ($\tilde{\nu}_{\mathrm{TO}} = 27.5\,\mathrm{cm}^{-1}$) of $CsPbI_3$ shows a phonon-softening effect with doping, the magnitude of phonon-softening decreases with doping density. In other word, higher doping density has made the Pb–I–Pb bending mode less soft, which is actually similar to the phonon-hardening effect observed in the Pb–I stretching mode. Further experimental investigations of this phonon hardening effect as a function of photo-excitation fluence will help to verify the doping-dependent trend predicted by the DFT calculations, which requires higher spectral resolution with precision of at least $0.1\,\mathrm{cm}^{-1}$. Nonetheless, the computational results obtained in this study suggest that the main effect of phonon hardening comes from the massive increase in dielectric screening resulting from the doping which can be induced by photo-excitation. This is an electronic process which can happen on an ultrafast timescale (on the order of a few picoseconds), whereas light-induced lattice structural change tends to happen on a much longer timescale hence less relevant in this investigation.

	Highest TO Pb-I stretching $\tilde{\nu}_{\mathrm{TO}}(\mathrm{cm}^{-1})$	Mid-TO Pb-I-Pb bending $\tilde{\nu}_{\mathrm{TO}}(\mathrm{cm}^{-1})$	Mid-TO A-site displacement $\tilde{\nu}_{\mathrm{TO}}(\mathrm{cm}^{-1})$
Undoped	81.0186	27.4562	13.4219
Doping 10^{17} cm^{-3}	0.3145	-6.2072	0.6723
Doping 10^{18} cm^{-3}	0.5647	-6.0362	0.8177
Doping 10^{19} cm^{-3}	0.6446	-5.8746	1.1404

Table 5.3: Effect of phonon hardening (positive number) or phonon softening (negative number) in cm^{-1} as a function of doping for three TO modes associated with Pb-I stretching, bending and A-site displacement. The effect includes adiabatic and non-adiabatic effects (at 300 K). Calculation performed by Dr. Samuel Poncé.

5.4 Summary

In conclusion, multiple phonon modes are observed in $MAPbI_3$ single crystals and thin films according to their absorption spectra obtained by the THz-TDS technique. Based on the DFT calculations, the dominant phonons in $MAPbI_3$ are assigned to Pb–I stretching modes which broaden at higher temperature, owing to the dynamic disorder of the lattice structure. The photoconductivity measurement via OPTPS suggests stronger electron-phonon coupling effect in the single crystal, which is the major limiting factor of the electrical charge-carrier mobility. Moreover, a blueshift of the phonon frequency is observed under photo-excitation, which is more prominent in the single crystal and gives rise to a derivative-like feature in its photoconductivity spectrum. The DFT calculations with non-adiabatic assumption predict the same phonon-hardening effect in the Pb–I stretching mode and the strength of phonon hardening tends to increase with doping density. The origin of such phonon hardening effect is assigned to the increase in dielectric screening due to photo-induced doping which is an ultrafast electronic process.

Chapter 6

Time-Resolved Cyclotron Resonance in InSb

6.1 Introduction

Hot charge carriers play an important role in semiconductor devices such as Gunn diodes [204,205], avalanche photodiodes [206,207] and hot carrier solar cells [208,209]. However, they can diminish the performance of other devices such as field effect transistors [210]. Therefore, a deep understanding of the temporal evolution and cooling of hot carriers in semiconductors is an important area of research, which is linked closely to the development of a wide range of semiconductor devices.

The term "hot charge carrier" refers to an energy distribution of electrons or holes that obey a Fermi-Dirac distribution, with a characteristic temperature that is higher than the lattice temperature of a semiconductor. Hot carriers in a semiconductor may arise by absorption of photons with energy significantly larger than the bandgap; by charges gaining kinetic energy, for example via application of an electric field; or via electrical injection from high-energy side valleys in the band structure, or a hetero-junction. While electron and hole distributions are initially likely to be non-thermal

(i.e. not able to be characterized by a Fermi-Dirac distribution), thermalization typically occurs on a 10 fs timescale [211–213] after which it is possible to define electron and hole temperatures.

Conduction band minima and valence band maxima can be approximated by a parabolic dispersion for energies very close to the minima/maxima, however this approximation becomes less valid at higher energy. This band non-parabolicity is particularly important for hot-carrier devices. For example, as a charge is accelerated to an energy beyond the parabolic region, it becomes effectively heavier as the band flattens from a parabolic shape, leading to a reduction in the charge mobility. A population of hot carriers therefore have a wide distribution of effective masses.

Hot carrier effects are pronounced in many narrow-bandgap semiconductors. InSb which is a typical direct-gap semiconductor has a bandgap of only 0.17 eV at room temperature and 0.235 eV at 4 K [214]. Its small electron effective mass, large electron mobility and high thermal conductivity make it an ideal candidate for high-speed electronic devices such as ultrafast transistors [54] and photodetectors [55, 215]. Its narrow bandgap also favors it in the field of thermal imaging such as infrared detectors and thermal image detectors [56]. Furthermore, quantum well heterostructures of InSb and AlInSb show a strong quantum Hall effect [216]. Because of the excellent optoelectronic properties, extensive studies have been performed on InSb over the last few decades. For example Dresselhaus *et al.* found that the effective mass of InSb at the bottom of the conduction band is $0.013\,m_{\mathrm{e}}$ by measuring cyclotron resonance at microwave frequencies [101]. The extremely small effective mass implies an ultrahigh charge mobility, which was reported to be $7.8\times10^{4}\,\mathrm{cm^{2}V^{-1}s^{-1}}$ at ambient temperature [7].

The non-parabolicity of the conduction band of InSb has drawn great interest over the past half century. Early cyclotron resonance experiments at infrared frequencies revealed an increase of effective mass with magnetic field [8–10], which implies a

non-parabolic feature of InSb. Since the spacing between adjacent Landau levels increases with the magnetic field, under higher magnetic field, charge carriers can reach the higher and flatter region of the conduction band where they exhibit larger effective mass. This dependence of effective mass on the magnetic field also agrees with Kane's $\mathbf{k}\cdot\mathbf{p}$ perturbation theory model [57]. In the Kane model, the introduction of nonparabolicity gives rise to an extra energy in the dispersion relation of the lowest conduction band, which is expressed as $E(\mathbf{k})(1+E(\mathbf{k})/E_{\mathrm{g}}) = \hbar^2|\mathbf{k}|^2/(2m_0^*)$ where E_{g} is the bandgap energy, $\hbar\mathbf{k}$ is the crystal momentum and m_0^* is the effective mass at the conduction band minimum, which is taken here as the energy reference.

Band non-parabolicity in InSb has also been observed through the observation of "forbidden" Landau transitions [217–219] and the magnetic-field-dependence of acoustic absorption [220]. Another way that band non-parabolicity can be probed is via microwave or infrared cyclotron absorption measurements of doped samples with different chemical potential. This is usually achieved by changing the extrinsic charge-carrier concentration. Since a few samples with doping densities are needed for this method, it is less convenient to probe the conduction band at a specific energy state and the range of measurable states are limited by the available doping densities of the samples [10, 218, 221, 222].

More recently, studies performed on undoped InSb samples utilizing time-resolved cyclotron resonance technique has demonstrated the non-parabolicity of InSb in terms of the hot-carrier cooling process. It was reported that the electron cyclotron mass increases at later photo-excitation times, which is attributed to the renormalization of the bandgap energy [223]. Similar measurements performed on InSb quantum wells, however, showed a decrease in effective mass at later delay time. Moreover a significant initial cyclotron resonance broadening was observed at early times after photo-excitation, due to the fact that more Landau levels are occupied initially and the carrier scattering rate is higher because of the higher carrier density [224]. Since

those experiments were performed using free-electron laser (FEL) at a fixed wavelength and the cyclotron resonance was probed with changing magnetic field which could go up to 9 T, the charge carriers might have reached sufficiently high energy levels in the conduction band where the non-parabolic feature is prominent.

In this study, time-resolved magneto-THz spectroscopy was used for investigating the electronic properties of a nominally undoped InSb sample. Unlike the previous studies [223, 224] where the cyclotron resonance of InSb was investigated by changing the magnetic field at a fixed FEL wavelength, here THz spectroscopy technique was utilized to obtain a cyclotron resonance spectrum of InSb whereas the magnetic field was fixed at a certain value. This technique was utilized to investigate the behavior of excitons in GaAs quantum wells [225], from which enhanced exciton stability was observed under magnetic field. In order to observe cyclotron resonance and hot-carrier cooling in the undoped InSb sample, the sample was photo-excited with photons of 1.55 eV which is greater than the bandgap, and hot-electron cooling was observed on an ultrafast timescale (up to 200 ps after photo-excitation) by varying the time delay between the THz pulse and the optical pump pulse. In addition, to gain deeper understanding of the non-parabolicity of InSb, the experimental results of the effective mass as a function of carrier density are compared with the theoretical results which were obtained using *ab initio* calculations within the GW approximation [226]. A very good agreement between the experimental and theoretical results is obtained, which gives insight into the mechanism of hot-carrier cooling. The time-resolved technique allows the cyclotron effective mass, charge scattering rate and charge density to be measured with picosecond time resolution. Prior experimental works demonstrated that at high magnetic fields (e.g. $B > 3$ T), heavy-hole cyclotron resonance split was observed in germanium quantum wells, which is attributed to the Rashba spin-orbit interaction [227, 228]. A mode softening effect of the polaritons was also reported on germanium and InSb quantum wells in the ultrastrong coupling regime where a

high magnetic field was applied [229]. Here, since the magnetic field was kept below 1 T and the InSb sample under investigation was a 3D bulk material which lacks quantum confinement, the spin-split effect was not observed in the electron cyclotron resonance. Hence a single cyclotron resonance peak was used for probing the electron effective mass in the conduction band of the undoped InSb sample.

6.2 Experimental and Computational Methods

6.2.1 Sample Fabrication and Specifications

The InSb sample was provided by Dr. Mark Ashwin from the University of Warwick. A 6.5 μm-thick undoped layer of InSb was grown by molecular beam epitaxy on a 2-inch wafer of (100)-oriented semi-insulating GaAs. The sample was then cut into a 1 cm$\times$1 cm square to be mounted on the sample holder in the superconducting magnet.

6.2.2 Magneto-THz Spectroscopy

Magneto-THz spectroscopy was used to study the cyclotron resonance phenomenon in InSb. An amplified laser pulse with a central wavelength of 800 nm, repetition rate of 5 kHz and 35-fs pulse duration time was split into a THz beam, a gate beam and a pump beam. The THz beam was generated by a 1 mm-thick (110) ZnTe crystal via optical rectification. The pump beam which was set at 800 nm (photon energy 1.55 eV) was used to photo-excite the InSb sample to generate charge carriers, from which the photoconductivity spectrum was measured. An external magnetic field that could go up to 7 T was generated by a superconducting magnet (Oxford Instruments, Spectromag) with its magnetic field perpendicular to the sample surface. Under the magnetic field, the photo-induced charge carriers inside InSb undergo a cyclotron motion and absorb a certain frequency component of the THz pulse. The transmitted

THz pulse was detected by polarization-resolved EOS using a set of a quarter-wave plate, a half-wave plate, a Wollaston prism, a 1 mm-thick (111) ZnTe crystal and a pair of balanced photodiodes. By changing the delay time between the pump pulse and the THz pulse, cyclotron resonance were measured at different photo-excitation delay times, from which the change in hot electron scattering time could be extracted. A schematic diagram of the magneto-THz spectroscopy setup and a more detailed description of the polarization-resolved technique are given Section 3.1.2.

6.2.3 Computational Setup

Theoretical calculations of the band structure and electron effective mass of InSb were performed by Prof. Marina Filip (University of Oxford, UK). All calculations were performed using the experimental structure of InSb extracted from the Inorganic Crystal Structure Database (database code 162197; Ref. 230). The quasiparticle band structure of InSb was calculated within the *GW* approximation [226], including spin-orbit coupling, as implemented in the Yambo code [231]. The starting point for mean-field eigenvalues was calculated within the generalized gradient approximation to DFT, in the Perdew-Burke-Erzerhof parametrization (DFT/PBE) [232], as implemented in the QUANTUM ESPRESSO code [87]. The ONCVPSP code was used to generate fully-relativistic optimized norm-conserving Vanderbilt pseudopotentials (ONCV) [233], using a similar setup to that reported in the Pseudo-Dojo database [178]. In the pseudopotentials, semicore electrons were included for both In and Sb, in the following valence configuration: $4s^2 4p^6 4d^{10} 5s^2 5p^1$ for In and $4s^2 4p^6 4d^{10} 5s^2 5p^3$ for Sb.

For the calculation of mean-field eigenvalues, a plane wave cutoff of 100 Ry and a Γ-centered **k**-point grid of $20 \times 20 \times 20$ were used. For the calculation of quasiparticle energies plane wave cutoffs of 66 Ry and 20 Ry were used for the exchange and polarizability respectively with 1500 bands and a **k**-point grid of $10 \times 10 \times 10$ centered

at Γ. This setup is similar to the computational setup reported in Ref. 234, and the quasiparticle bandgap of InSb was estimated to converge within 30 meV.

The quasiparticle band structure was calculated using Wannier interpolation, as implemented in the Wannier90 code [235–238]. The maximally localized Wannier functions was calculated by interpolating the single-particle DFT/PBE band structure using a coarse **k**-point grid of $10 \times 10 \times 10$, starting from 16 sp^3 projectors. The calculated Wannier functions were then used to interpolate the quasiparticle band structure from quasiparticle eigenvalues calculated on the same mesh. It is noted that the four highest occupied quasiparticle eigenvalues at the Γ point, which are expected to be degenerate in InSb, differ by up to 50 meV. This is attributed to the numerical inaccuracy of convergence. To correct this behavior for the construction of the quasiparticle band structure, the top four quasiparticle eigenvalues at the top of the valence band were manually modified to the average of the four calculated eigenvalues. This modification has no effect on the shape or position of the conduction band edge.

The electron effective mass was calculated from fitting the conduction band minimum to the Kane model, and through direct computation of the effective mass tensor, $m^*_{ij} = 1/[\hbar^2(\partial^2\epsilon/\partial k_i \partial k_j)^{-1}]$, where i and j index the Cartesian directions. The second derivatives were calculated using the finite-difference method, with an increment of $\delta k = 0.001\,(2\pi/a)$, where a is the lattice parameter of InSb. Both methods yield effective masses within $10^{-4}\,m_\mathrm{e}$.

6.3 Results and Discussions

6.3.1 Cyclotron Resonance in Photo-Excited InSb

OPTPS as an ideal non-contact technique for measuring photoconductivity of semiconductor materials allows charge-carrier cooling [239] and recombination dynamics [36, 38] to be observed on a sub-picosecond timescale. In OPTPS, conductivity is probed using a sub-picosecond single-cycle electromagnetic (THz) pulse which travels in free space, thereby avoiding the need to make physical electrical contacts to the semiconductor. Hence the technique is well suited to nanomaterials and systems where Ohmic contacts are difficult to achieve. Time-resolved measurements are obtained by adjusting the time delay, t_{delay}, between an optical pulse, which photo-injects electron-hole pairs in the semiconductor and the THz probe pulse.

In traditional OPTPS measurements a frequency averaged conductivity can be measured [36, 38] at each time after photo-excitation or the full THz AC conductivity spectrum can be recorded at each point after illumination. In most bulk semiconductors the AC conductivity spectrum fits well to the Drude model,

$$\Delta\sigma(\omega) = \frac{ne^2}{m^*}\frac{i}{\omega + i\gamma}, \tag{6.1}$$

where n is the charge-carrier density determined by the photo-excitation fluence, m^* is the effective mass of the charge carrier and $\gamma = 1/\tau$ is the momentum scattering rate with τ corresponding to the scattering time. Thus it is possible to extract γ and the value of n/m^* as a function of time after photo-excitation. By measuring the absorption coefficient of the semiconductor and the fluence of the laser pulse it is also possible to determine n and hence establish m^* immediately after photo-excitation. However at later times n and m^* cannot be separated as both quantities change as a result of charge recombination and band non-parabolicity respectively. Thus studying

hot charge carrier relaxation with this technique is challenging.

Here the OPTPS is extended to perform time-resolved cyclotron resonance spectroscopy and hence observe m^*, the energy-dependent cyclotron effective mass, on a picosecond timescale. Figure 6.1(a) is a pictorial representation of the time-resolved magneto-THz spectroscopy experiment. A femtosecond laser pulse (optical pump) is first used to photo-excite a semiconductor sample which is held at a low temperature (4 K) in a magnetic field B. A linearly polarized THz probe pulse with **k**-vector parallel to the magnetic field arrives at a set time, t_{delay}, after the optical pump pulse and the amplitude of the electric field of the THz pulse $E(t, t_{\mathrm{delay}})$ is recorded after it has been transmitted through the sample. Meanwhile, the electric field of the THz pulse passed through the photo-excited semiconductor is compared to that of the unilluminated semiconductor to give a change in the THz signal $\Delta E(t, t_{\mathrm{delay}}) = E_{\mathrm{light}}(t, t_{\mathrm{delay}}) - E_{\mathrm{dark}}(t, t_{\mathrm{delay}})$, which can be measured simultaneously with $E(t, t_{\mathrm{delay}})$. Therefore $\Delta E(t, t_{\mathrm{delay}})$ represents the change in the THz pulse associated with the photo-injection of electron-hole pairs. In the case of electron cyclotron resonance with a magnetic field in the same direction as the THz pulse **k**-vector, a right-handed circularly polarized component (σ_+) of the incident THz pulse will be absorbed in the process of promoting electrons to the next available Landau level. Therefore, the recorded $\Delta E(t, t_{\mathrm{delay}}, B) = E_{\mathrm{light}}(t, t_{\mathrm{delay}}, B) - E_{\mathrm{dark}}(t, t_{\mathrm{delay}}, B)$ directly measures cyclotron resonance of photo-injected electrons at the frequency ω_{c} given by Equation (2.25). Both $\Delta E(t, t_{\mathrm{delay}}, B)$ and the cyclotron motion of the electrons are right-handed circularly polarized, as illustrated in Figure 6.1(a).

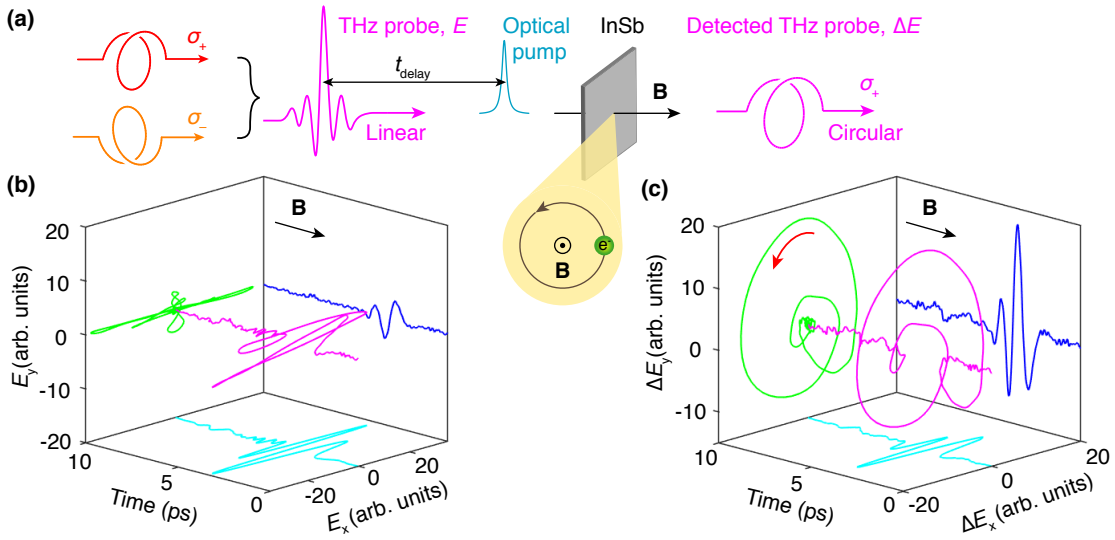

Figure 6.1: (a) A schematic diagram of the time-resolved magneto-THz spectroscopy experiment of an undoped InSb sample. The magnetic field and the **k**-vector of the THz pulse are in the same direction and perpendicular to the sample surface. The incident THz pulse are regarded as a superposition of right-handed circular polarization σ_+ and left-handed circular polarization σ_-. (b) Electric field of the transmitted THz pulse without photo-excitation, $E_{\rm dark}(t, t_{\rm delay}, B)$, measured at a magnetic field $B = 0.6\,\mathrm{T}$. (c) The change of THz transmission $\Delta E(t, t_{\rm delay}, B)$ measured at 200 ps after photo-excitation with a fluence at $5.4\,\mathrm{nJ/cm^2}$ under a magnetic field $B = 0.6\,\mathrm{T}$. The x-component and the y-component of the recorded THz signal (E or ΔE) are represented by the light blue and dark blue lines respectively and the pink line represents the resultant THz signal. The black arrows indicate the direction of the applied magnetic field and the red arrow in panel (c) shows that ΔE is right-handed circularly polarized (σ_+).

An example of $E_{\mathrm{dark}}(t, t_{\mathrm{delay}}, B)$ and $\Delta E(t, t_{\mathrm{delay}}, B)$ for InSb measured at $B = 0.6\,\mathrm{T}$ is shown in Figure 6.1(b) and 6.1(c) respectively, with $t_{\mathrm{delay}} = 200\,\mathrm{ps}$. By taking the Fourier transform of these two data sets, it is possible to obtain the change in photoconductivity associated with the cyclotron resonance,

$$\Delta\sigma(\omega) = -\varepsilon_0 c\alpha(1+\tilde{n})\left[\frac{\Delta E(\omega, B)}{E_{\mathrm{dark}}(\omega, B)}\right], \tag{6.2}$$

where ε_0 is the permittivity of free space, c is the speed of light, α is the absorption coefficient of InSb and $\tilde{n}$ is the refractive index of InSb at THz frequencies. The resultant photoconductivity spectrum of InSb under a magnetic field features a characteristic cyclotron absorption peak at frequency ω_{c}. Alternatively, this cyclotron resonance feature can be illustrated as an absorption dip in the transmission spectrum,

$$E_{\mathrm{transmission}}(\omega, B) = \frac{E_{\mathrm{light}}(\omega, B)}{E_{\mathrm{dark}}(\omega, B)}, \tag{6.3}$$

which will be used in Section 6.3.2 for investigating the electron effective mass of InSb as a function of magnetic field strength.

It is noted here that given the field and polarization-resolved nature of the magneto-THz spectroscopy technique, it is possible to extract and assign electron and hole cyclotron effective masses from the same dataset according to the handedness of cyclotron resonance (if measured at a value of B for which both electron and hole effective masses lie within the spectral bandwidth of the THz pulse). In the figuration presented in this study, the electron cyclotron resonance and hence ΔE are right-handed circularly polarized. In contrast, the hole cyclotron resonance is left-handed circularly polarized, which is not observed in this THz detection range.

6.3.2 Magnetic-Field Dependence of Electron Effective Mass

To investigate the band structure of intrinsic InSb hence to understand its fundamental electronic properties without the effect of extrinsic charge carriers, the magneto-THz spectroscopy was utilized to measure the effective mass of electrons within the conduction band. All measurements were performed with the intrinsic InSb sample held in a helium flow cryostat at at 4 K in the core of a superconducting magnet. Since the InSb sample was nominally undoped there is negligible Burstein-Moss shift, giving a bandgap energy of InSb at 4 K of 0.235 eV. Therefore each absorbed 1.55 eV photon from the laser pulse generated extremely hot electron-hole pairs with 1.32 eV kinetic energy.

Figure 6.2(a), showing the THz transmission spectra through the photo-excited InSb sample calculated by Equation (6.3), was measured under magnetic field ranging from 0.1 to 1 T at photo-excitation fluence of 5.4 nJ/cm^2. The prominent dip in each spectrum arises from the absorption of THz signal due to cyclotron resonance, whereas the additional features around $T = 1$ are due to zero padding of the raw data which amplifies the signal fluctuations. As the magnetic field increases, ω_c shifts to higher frequencies, which is expected from Equation (2.25).

Moreover, as illustrated by Figure 6.2(b), the cyclotron effective mass increases with magnetic field, which is attributed to the larger Landau level spacing under higher magnetic field. Hence the electrons are photo-excited to higher energy in the non-parabolic conduction band, and exhibit larger effective mass [240]. By extrapolating the effective mass to $B = 0$, a value of $0.0144\, m_e$ was obtained, which is higher than the previously reported effective mass measured at the bottom of the conduction band ($0.013\, m_e$ [101]), suggesting that the electron population was at an energy above the conduction band minimum. At $B = 0.1, 0.2$ and 0.3 T, since ω_c is closer to the edge of THz detection range, the experimental values of ω_c have larger uncertainties, resulting in larger error bars of the extracted effective mass.

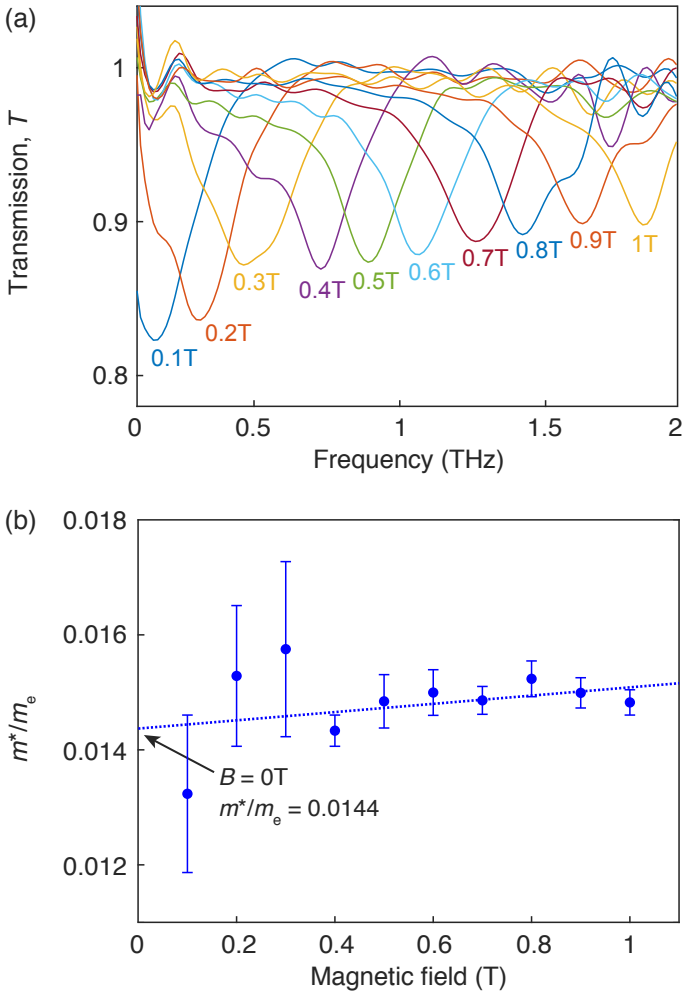

Figure 6.2: Electron cyclotron resonance measurements of an undoped InSb sample performed at 200 ps after photo-excitation at fluence 5.4 nJ/cm^2. (a) THz transmission spectra of InSb measured at magnetic field ranging from 0.1 to 1 T. (b) Electron effective mass of InSb as a function of magnetic field. The blue dots represent the experimental data and the blue line represents the extrapolation of the experimental data from which the electron effective mass at $B = 0$ was extracted to be $0.0144\, m_e$.

6.3.3 Hot Electron Cooling in InSb

Now the cooling of hot photo-excited electrons in InSb is to be examined. Generally, the hot-carrier dynamics can be investigated via OPTPS by measuring the THz photoconductivity of the material at various pump-probe delay times, t_{delay}, and by fitting a Drude-Lorentz model to each photoconductivity spectrum, the carrier scattering lifetime can be extracted as a function of t_{delay}, which is used as a key parameter for analysing hot-carrier cooling process in narrow-gap semiconductors such as GaAs and InAs [241]. This technique has also been applied to MHPs such as tin iodide perovskite thin films whose dominant hot-carrier relaxation mechanism is found to be electron-phonon interaction [242].

In this section, time-resolved magneto-THz spectroscopy is utilized to probe the cyclotron effective mass of InSb as a function of photo-excitation delay time, which also serves as an indicator of the hot-electron cooling process. In addition, the time-dependent effective mass gives insight to the non-parabolicity of the conduction band. Figure 6.3(a) shows the frequency-averaged THz photoconductivity dynamics of InSb which is photo-excited by 1.55 eV photons in the absence of magnetic field. While absorption occurs on the 35 fs timescale, photoconductivity can be seen to rise on a timescale of tens of picosecond. The time-resolved effective mass measurements presented as red stars in Figure 6.3(b) conclusively show that this slow rise in $\Delta\sigma$ is a direct result of electron cooling. That is, the effective mass can be seen to reduce on the same timescale as the photoconductivity rises, in close agreement with Equation (6.1). As demonstrated by the band structure of InSb shown in Figure 6.3(c), the energy of the photo-injected electrons E_{photon} is much larger than the bandgap E_{g}, which causes the hot electrons to reach the non-parabolic region of the conduction band. Hence, the change in effective mass is a result of hot electrons gradually cooling from this non-parabolic region towards the Γ minimum, which is represented by the black arrows. Near the conduction band minimum which is approximately

parabolic (represented by the pink dashed line), the electron effective mass is around $0.013\,m_e$ [101]. Within the picosecond timescale, it is observed that at 200 ps after photo-excitation, although the hot electrons have cooled down to a much lower energy than the initially photo-excited energy state, they have an energy distribution that is still above the Γ minimum, which leads to a larger effective mass of $0.0166\,m_e$. The inset of Figure 6.3(a) shows the measured photoconductivity spectrum at 200 ps after photo-excitation in the absence of a magnetic field. The data agree closely with the Drude model, with the solid lines in the inset being a fit to Equation (6.1). The electron scattering time is extracted as $\tau = 0.22$ ps with electron density $n = 1.4 \times 10^{17}\,\mathrm{cm}^{-3}$. This type of measurement is possible at any time after photo-excitation, and combined with the cyclotron data provides a complete picture of charge-carrier dynamics in a photo-excited semiconductor.

The product of charge-carrier density and relaxation time, $n\tau$, is shown in Figure 6.3(b) as blue triangles. It reduces rapidly over the initial 50 ps primarily as a result of n decaying via bimolecular and Auger recombinations. This should act to reduce the $\Delta\sigma$, however the competing strong reduction in m^* from 0.0324 to $0.0168\,m_e$ has a much larger impact thus causing the observed $\Delta\sigma$ to increase.

Figure 6.4 shows the cyclotron resonance data taken at 13, 20, 27, 47 and 200 ps after photo-excitation fitted with a Lorentzian lineshape,

$$\Delta\sigma(\omega) = \frac{1}{\pi}\frac{\gamma/2}{(\omega-\omega_c)^2 + (\gamma/2)^2}, \tag{6.4}$$

from which the electron relaxation time is extracted ($\tau = 2/\gamma$). Compared to the photoconductivity measurement shown in the inset of Figure 6.3(a), τ extracted from the cyclotron resonance data increases by 1.5 times to 0.32 ps, which is consistent with a restriction of phase space due to Landau quantization induced by magnetic field reducing the probability of electron scattering.

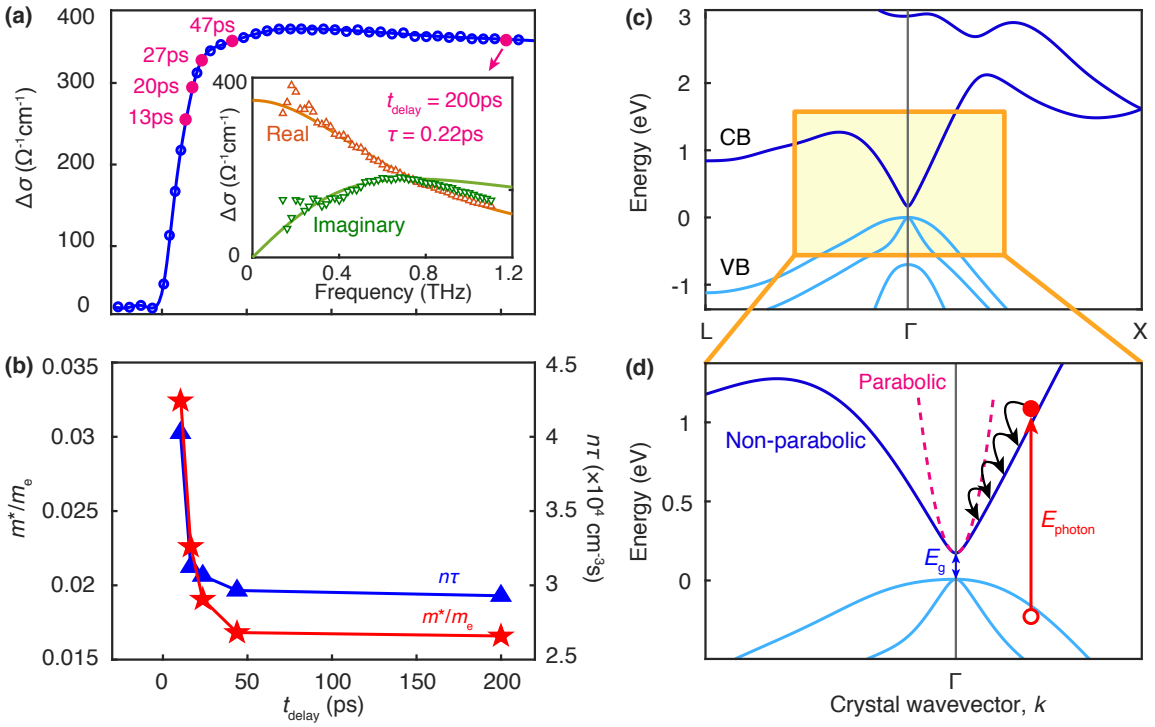

Figure 6.3: (a) Transient absorption spectrum of the photo-excited InSb sample measured at fluence 335 nJ/cm^2. The blue circles represent the experimental data and the pink circles specify a few values of t_{delay} at 13, 20, 27, 47 and 200 ps where the cyclotron resonance spectra of InSb were taken. The inset shows the photoconductivity spectrum measured at 200 ps after photo-excitation with a Drude fit when no magnetic field was applied. (b) Electron effective masses (red stars) extracted from the cyclotron resonance measurements which were performed at 13, 20, 27, 47 and 200 ps after photo-excitation under a magnetic field $B = 0.4$ T. The blue triangles represent the product of charge-carrier density and relaxation time, $n\tau$. (c) Quasiparticle band structure of InSb calculated by Prof. Marina Filip. The dark blue lines represent the conduction band (CB) and the light blue lines represent the valence band (VB). (d) A zoom-in of the area near the Γ valley. The pink dashed line represents a parabolic CB for comparison which overlaps with the non-parabolic CB near the Γ minimum. The solid and open red circles represent an electron-hole pair generated by photo-excitation. The black arrows represent the hot electron cooling process on the picosecond timescale.

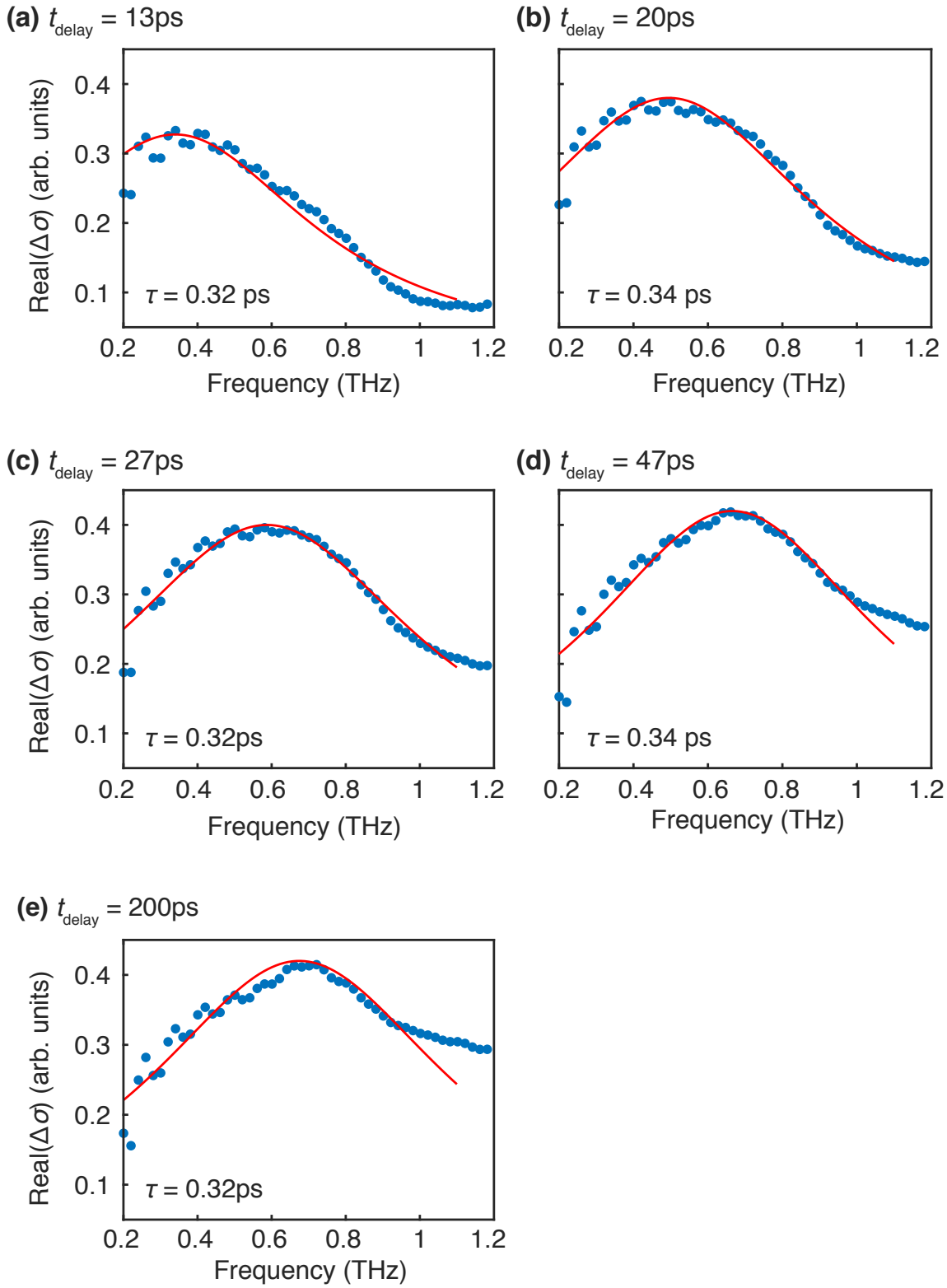

Figure 6.4: Cyclotron resonance spectra of InSb measured at $B = 0.4\,\mathrm{T}$ at (a) 13 ps, (b) 20 ps, (c) 27 ps, (d) 47 ps and (e) 200 ps after photo-excitation under fluence of $335\,\mathrm{nJ/cm^2}$. The blue solid circles represent the experimental data, whereas the red curves are the Lorentzian lineshape fit to each spectrum.

6.3.4 Quasiparticle Band Structure Calculation

To gain further insight into the electronic structure of InSb, the quasiparticle band structure, $E_{n\mathbf{k}}$, was calculated from first-principles within the GW approximation as [226, 243]

$$E_{n\mathbf{k}} = \epsilon_{n\mathbf{k}} + Z_{n\mathbf{k}}\langle n\mathbf{k}|\Sigma - V_{\mathrm{xc}}|n\mathbf{k}\rangle, \tag{6.5}$$

where $\epsilon_{n\mathbf{k}}$ and $|n\mathbf{k}\rangle$ are mean-field energies and wave functions corresponding to the electronic band n and wave vector $\mathbf{k}$, calculated within DFT [244]. V_{xc} is the exchange-correlation potential, $Z(\omega) = \left[1 - \mathrm{Re}(\partial\Sigma/\partial\omega)\right]^{-1}$ is the quasiparticle renormalization factor, and Σ is the electron self energy, calculated in the GW approximation as the convolution of the single-particle Green's function, G, and the screened Coulomb interaction, W.

A quasiparticle bandgap of 0.17 eV was calculated, which is in agreement with prior GW calculations starting from DFT/LDA (0.28 eV [234]), and HSE06 hybrid functional [245] (0.36 eV [246]). The small difference between this calculation and prior works can be attributed to the dependence of GW quasiparticle bandgaps on the mean-field starting point, as well as the different implementations of spin-orbit coupling effects. Figures 6.3(c) and 6.3(d) depict the quasiparticle band structure of InSb obtained from the interpolation of quasiparticle eigenvalues using Wannier functions [235–238]. As expected, it is found that the conduction band is highly isotropic and can be described by the Kane model, for up to 400 meV above the conduction band minimum, within numerical accuracy. Using this model, the effective mass at the conduction band bottom is calculated as $0.013\,m_{\mathrm{e}}$, a value confirmed by direct numerical calculations of the effective mass tensor. In addition, the calculated electron effective masses are in good agreement with the experiment ($0.013\,m_{\mathrm{e}}$ [101]) and with prior first-principles calculations ($0.017\,m_{\mathrm{e}}$ [246]).

Having directly verified that the Kane model accurately describes the conduction

band of InSb, the analytic expression of the conduction band dispersion is used to derive the density of states (including spin degeneracy),

$$g(E) = \frac{1}{2\pi^2}\left(\frac{2m_0^*}{\hbar^2}\right)^{3/2}[1 + 2E/E_\mathrm{g}]\sqrt{E(1 + E/E_\mathrm{g})}, \tag{6.6}$$

where the non-parabolicity constant α shown in Equation (2.20) is approximated as $1/E_\mathrm{g}$. Similarly, starting from the definition of the cyclotron effective mass corresponding to an isotropic energy band, $m^* = (1/\hbar^2)(\partial^2 E/\partial k^2)$ [247], and substituting the Kane model expression, $m^*(E) = m_0^*(1 + 2E/E_\mathrm{g})$ is obtained.

The distribution of electrons for a given concentration n can be computed as

$$N_e(E; n, T) = [g(E) f_T(E; \mu_{n,T})] * L_\delta(E), \tag{6.7}$$

where the Fermi-Dirac distribution function $f_T(E; \mu_{n,T})$ and the lifetime broadening of electronic states were approximately accounted for through the convolution with a uniformly broadened Lorenzian distribution L_δ. It is noted that in this theoretical investigation the quasiparticle lifetimes were not calculated explicitly. Instead, a uniform broadening, $\delta = 2\,\mathrm{meV}$, of the electronic states was chosen, which represents the average FWHM measured across different carrier concentrations. The chemical potential $\mu_{n,T}$ was determined by equating the calculated electron concentration $n = \int_0^\infty g(E) f_T(E; \mu_{n,T}) dE$ with the value measured experimentally, while keeping the electronic temperature T as a free parameter. This is in line with the BTE which can be used for describing the charge-carrier transport in a thermodynamic system. Here, the electron distribution as a function of electronic temperature reflects the hot-electron cooling process which is a key mechanism of charge-carrier dynamics in InSb when above-bandgap photo-excitation is applied.

6.3.5 Non-Parabolic Conduction Band Probed by Quasi-Fermi Level

Now the non-parabolic feature of the conduction band of intrinsic InSb can be investigated in more depth. Firstly, the cyclotron resonance spectrum was measured at various energy levels above the bottom of the conduction band by changing the photo-excitation fluence. This is equivalent to the conventional method of tuning the Fermi energy level by implementing different doping density in n-type InSb but with better flexibility and consistency since only one intrinsic InSb sample was used. Here, the photo-excitation fluence ranges from 5.4 to 936 $\mathrm{nJ/cm^2}$, which can be converted to electron density according to the following equation,

$$n = \frac{\text{Fluence} \cdot \alpha}{E_{\text{photon}}}, \tag{6.8}$$

where $\alpha \approx 10^5\,\mathrm{cm^{-1}}$ is the absorption coefficient of InSb at 800 nm [248] and E_{photon} is the energy of a single photon at 800 nm. This is a rough estimation of the electron density generated via photo-excitation assuming a uniform distribution of electrons within the absorption depth of InSb. It should be noted that the electron density calculated by this equation represents the initial electron density, i.e. at the instant of photo-excitation. At later times when charge-carrier recombination and diffusion come into play [71], the charge-carrier density will decrease. Therefore, Equation (6.8) gives an upper limit of the electron density at 200 ps after photo-excitation when the cyclotron resonance spectra of InSb were taken. As shown in Figure 6.5(a), the experimentally measured cyclotron resonance spectra of InSb with initial electron density estimated as 2×10^{15}, 2×10^{16}, 2×10^{17} and $4 \times 10^{17}\,\mathrm{cm^{-3}}$ are represented by the solid circles. The solid lines represent the corresponding Lorentzian lineshape fit given by Equation (6.4), from which the cyclotron resonance frequency ω_c and FWHM were extracted.

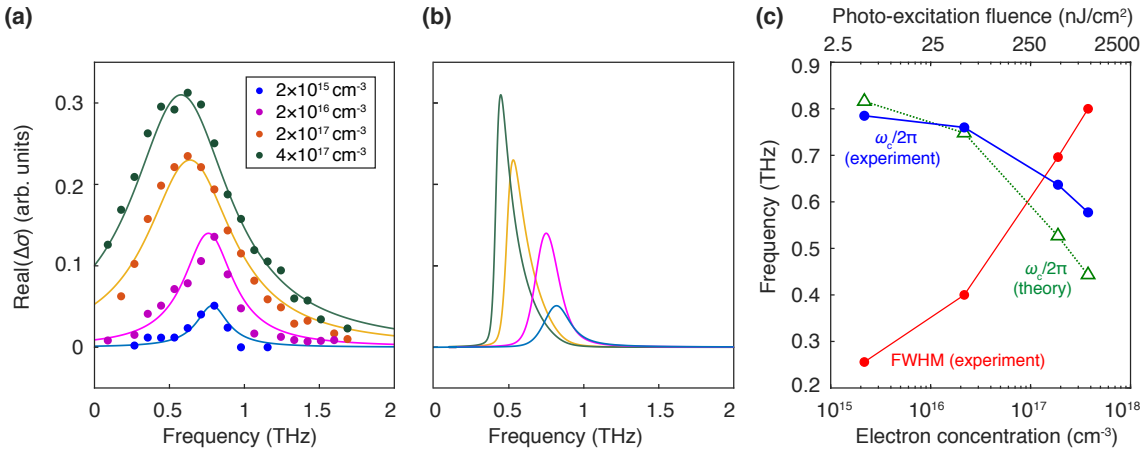

Figure 6.5: (a) Cyclotron resonance spectra of InSb measured at 200 ps after photo-excitation at initial electron densities 2×10^{15}, 2×10^{16}, 2×10^{17} and $4 \times 10^{17}\,\mathrm{cm}^{-3}$. The experimental data (solid circles) were fitted with Lorentzian lineshape (solid lines) to extract ω_c and FWHM. (b) Cyclotron resonance spectra calculated by Prof. Marina Filip for an electron temperature $T = 59\,\mathrm{K}$. (c) ω_c and FWHM extracted from the experimental data are represented by the blue and red circles respectively. The theoretical values of ω_c are represented by the green triangles.

In the theoretical calculation, the cyclotron resonance spectra were calculated using the expression for the photo-excited charge carrier distribution given in Section 6.3.4,

$$N_e(\omega_c; n, T) = N_e(E; n, T)/(d\omega_c/dE), \tag{6.9}$$

where $d\omega_c/dE = -\frac{eB}{M^{*2}(E)}(dM^*/dE)$, with $M^*(E)$ calculated as the convolution $M^*(E) = m^*(E) * L_\delta(E)$. Figure 6.5(b) shows the calculated cyclotron resonance spectra at the same electron densities as the experimental measurements shown in Figure 6.5(a), with magnitudes normalized to those of the experimental data. Both of the experimental and theoretical results illustrate a redshift of the cyclotron resonance frequency ω_c at higher electron density, which confirms the initial hypothesis that the increase of effective mass is due to the non-parabolicity of the conduction bands.

It should be noted that the real part of the conductivity plotted in Figure 6.5 (and also Figure 6.4) is the horizontal (x-direction) polarization component which is in the same direction as the electric field of the incident THz pulse. It is expressed by the σ_{xx} component of the conductivity tensor given by [249],

$$\sigma_{ij}(\omega) = \begin{bmatrix} \sigma_{xx} & \sigma_{xy} \\ \sigma_{yx} & \sigma_{yy} \end{bmatrix} = \frac{\sigma_0}{(1 - i\omega\tau)^2 + \omega_c^2\tau^2} \begin{bmatrix} 1 - i\omega\tau & -\omega_c\tau \\ \omega_c\tau & 1 - i\omega\tau \end{bmatrix}, \tag{6.10}$$

where σ_0 is the DC conductivity and ω_c is determined by Equation (2.25). τ is the electron scattering lifetime. The off-diagonal components σ_{xy} and σ_{yx} represent the conductivity components which are orthogonal to the THz electric field. Figure 6.6(a) and Figure 6.6(b) show the experimentally measured $\Delta\sigma$ measured at high and low fluencess respectively, with the blue and red solid circles representing the real and imaginary parts respectively. According to the theoretical fits (solid lines), the electron scattering lifetimes for the high and low fluences are 0.33 and 0.9 ps respectively. This is consistent with the fact that at higher electron density, electron-electron scattering is more frequent and hence the electrons have shorter lifetime.

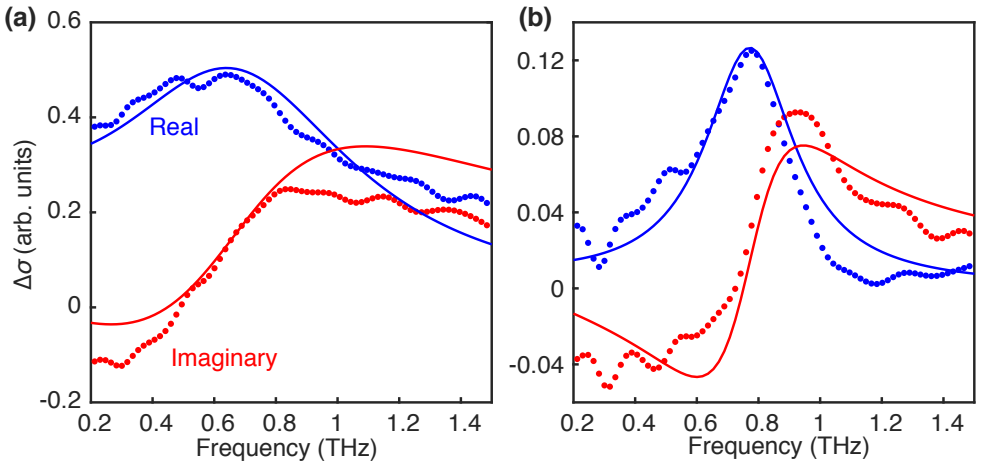

Figure 6.6: Photoconductivity of InSb under a magnetic field $B = 0.4\,\mathrm{T}$ at 200 ps after photo-excitation at fluences (a) $468\,\mathrm{nJ/cm^2}$ and (b) $54\,\mathrm{nJ/cm^2}$. The blue and red solid circles represent the real and imaginary parts of the experimental data respectively. The solid lines represent the theoretical fits obtained from σ_{xx}.

Equivalent to the scattering lifetime, the FWHM of the experimentally measured cyclotron resonance spectra shown in Figure 6.5(a) increases significantly with increasing electron density, which is represented by the red solid circles in Figure 6.5(c). There are two factors which jointly contribute to this broadening. Firstly carrier-carrier scattering increases with charge density and secondly as the quasi-Fermi level is raised, a larger range of effective mass values are spanned by the electron population, owing to increasing conduction band non-parabolicity. As for the theoretically calculated cyclotron resonance spectra shown in Figure 6.5(b), however, since a uniform broadening was assumed (as mentioned in Section 6.3.4), the FWHM is less informative and hence not shown in Figure 6.5(c).

To investigate conduction band non-parabolicity and electron cooling in InSb more quantitatively, a comparison between theory and experiment is made. The band averaged effective masses corresponding to a given carrier concentration n and electronic temperature T can be calculated as

$$\langle m^* \rangle_{n,T} = \frac{\int_0^\infty m^*(E) g(E) f_T(E;\mu_{n,T}) dE}{\int_0^\infty g(E) f_T(E;\mu_{n,T}) dE}. \tag{6.11}$$

In Figure 6.7, the calculated effective masses are represented by the solid colored circles, covering a wide electron temperature range 1–580 K. It can be seen that the calculated effective masses are in good agreement with experimental data (represented by red solid circles). The small differences between the calculated range of effective masses and experiment is attributed to the sensitivity of the Kane model conduction band dispersion on the calculated bandgap. This is explicitly demonstrated in Figure 6.8 where the effective masses are calculated in the same way as in Figure 6.7, but using the experimental bandgap of 0.24 eV. It is noted that a larger bandgap leads to a narrowing of the conduction band width, and in turn to a narrowing of the range of effective masses calculated as a function of electronic temperature. While

absolute values of the calculated effective masses are slightly sensitive to the calculated bandgap, the trend is unaffected and is in good agreement with experimental measurements both from this and prior works.

Another factor that may cause the slight discrepancy between the experimental data and the theoretical calculations is the electron density estimated for each electron cyclotron measurement. As mentioned at the beginning of this section, the electron density calculated using Equation (6.8) only gives an upper limit of the electron density, whereas at 200 ps after photo-excitation, the electron density is expected to reduce due to charge-carrier recombinations and electron diffusion. Here, the lower bound of the electron density at 200 ps after photo-excitation is estimated as 73 % of the initial electron density based on the decrease in $n\tau$ with t_{delay} as shown in Figure 6.3(b) and the approximately constant τ extracted from Figure 6.4. However, it should be noted that the electron density estimated using this method may be subjected to some experimental uncertainties due to its dependence on the experimentally measured effective mass and scattering rate according to Equation (6.1). A more proper analysis of the change of electron density as a function of t_{delay} by taking into account the effects of electron diffusion will give a more accurate determination of the electron density at a certain time after photo-excitation, and a better agreement between the experimental and theoretical results may be achieved.

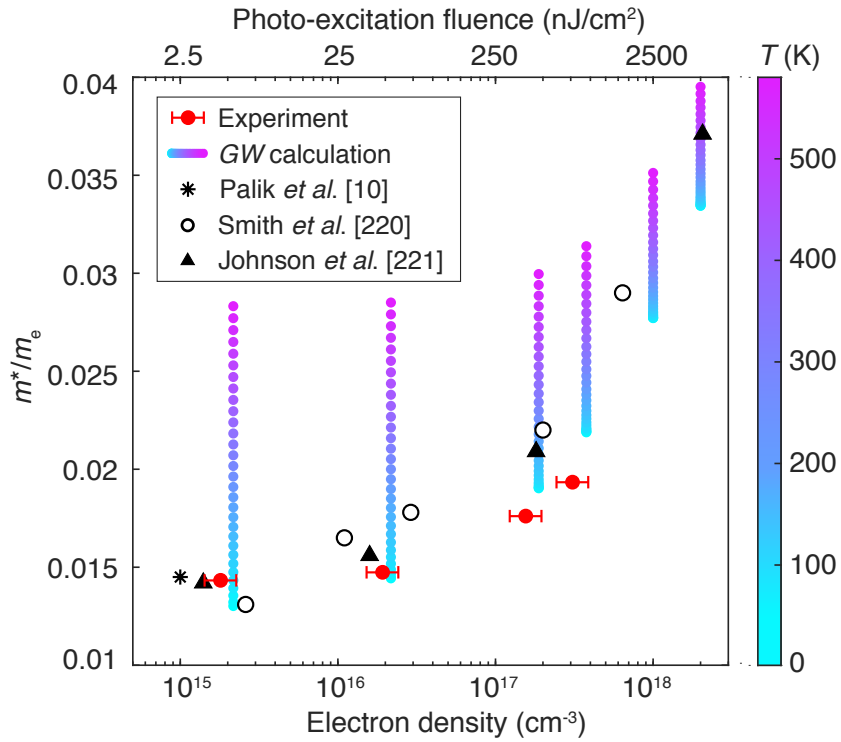

Figure 6.7: Effective mass as a function of electron density. The red solid circles represent the experimental data of electron effective mass measured at initial electron densities 2×10^{15}, 2×10^{16}, 2×10^{17} and $4 \times 10^{17}\,\mathrm{cm}^{-3}$. The solid colored circles represent the calculated effective masses by Prof. Marina Filip using the calculated GW bandgap in the Kane model expression for the conduction band dispersion. The black asterisk, the open circles and the solid triangles represent previously reported effective masses measured in n-type InSb with various doping densities [10, 221, 222].

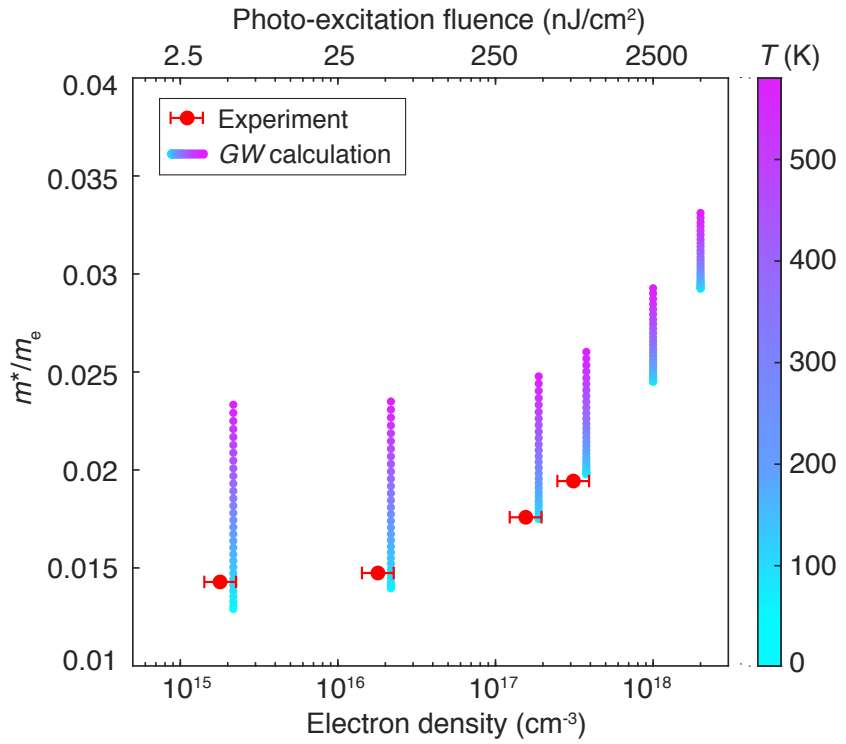

Figure 6.8: Effective mass calculated by Prof. Marina Filip using the experimental bandgap of 0.24 eV in the Kane model expression for the conduction band dispersion. The experimental and theoretical results are represented by the red solid circles and colored circles respectively.

6.4 Summary

In summary, this study shows that time-resolved magneto-THz spectroscopy is a versatile technique for probing the dynamics of hot charge carriers in semiconductors. It allows electronic properties including charge-carrier density, scattering rate, mobility and cyclotron effective mass to be measured on a picosecond timescale. *GW* band structure calculation was performed on the technologically significant narrow-bandgap semiconductor InSb and excellent agreement between the calculations and the THz experiments is found. Conduction band non-parabolicity was experimentally observed by photo-doping InSb in close agreement with the *GW* results. Hot electrons were injected into InSb by photo-excitation, and hot-carrier cooling was observed over a period of 200 ps. The ability to measure simultaneously effective mass and conductivity on this timescale is particularly significant. Furthermore the technique can be extended to observe sub-picosecond carrier dynamics and is applicable to a wide range of semiconductors and semiconductor heterostructures. Recent achievements in polarization-sensitive THz detectors [123] will make this technique more accessible.

Chapter 7

Conclusions and Outlook

In the last few decades, researchers have been devoted to exploring and understanding the electronic properties of MHPs and narrow-gap semiconductors, with the hope of realizing high-performance optoelectronic devices. Charge-carrier transport as the key property in assessing the optoelectronic performance of MHPs and narrow-gap semiconductors is investigated in this thesis. Utilizing the time-resolved THz spectroscopy along with a range of complementary techniques including temperature-dependent PL spectroscopy and first-principles calculations, deeper understanding of the optoelectronic properties of $MAPbI_3$ perovskites and intrinsic InSb is gained.

In Chapter 4, the temperature dependence of electrical mobility of $MAPbI_3$ single crystals and thin films was investigated to elucidate the fundamental limiting factor of the optoelectronic performance of perovskite-based photovoltaic devices, especially those made with polycrystalline thin films. The decrease of mobility with increasing temperature is consistent with the increasing occupancies of phonon modes in $MAPbI_3$ at higher temperature, suggesting that LO-phonon scattering (Frölich interaction) is the dominant mechanism which places an upper bound of the electrical mobility. Theoretical calculations based on first-principles and BTE show a good agreement with the temperature-dependence of mobility of $MAPbI_3$ single crystal, although the

impurities and defects present in the real single crystal have reduced the mobility to a small extent compared with the theoretical results. As for $MAPbI_3$ thin films, further deviation from the theoretical prediction of the temperature-dependent mobility is attributed to the effect of grain-boundary scattering. By implementing grain-boundary scattering into the BTE model, a better agreement in the temperature-dependent trend of mobility between the experiment and theory was achieved and the grain size of the polycrystalline thin films was determined. Under the usual device operating conditions, $MAPbI_3$ polycrystalline thin films were found to show similar charge-carrier diffusion length to single crystals, which suggests that the thin films have relatively benign grain boundaries. This makes the thermal co-evaporated $MAPbI_3$ thin films promising for future photovoltaic applications such as upscaled solar panels.

In Chapter 5, the lattice vibrations (optical phonons) of $MAPbI_3$ were explored in more depth to understand their fundamental relationship with the charge carriers. According to the absorption spectra obtained from the dark conductivity/reflectivity measurements, the primary LO-phonon peaks observed in $MAPbI_3$ single crystals and polycrystalline thin films are assigned to Pb–I stretching mode. Under photo-excitation where free charge carriers (electrons) are generated in the conduction band, the phonon modes of $MAPbI_3$ single crystal were found to undergo a blueshift, giving rise to a derivative-like feature in the photoconductivity spectrum. Based on the DFT calculations, the origin for such phonon hardening effect was found to be the increase in dielectric screening due to electron doping, which confirms the electron-phonon coupling in MHPs from a different perspective.

In Chapter 6, the non-parabolicity of the conduction band of intrinsic InSb, a narrow-gap semiconductor with extremely high electrical mobility, was probed using the technique of time-resolved magneto-THz spectroscopy. The electron effective mass was measured via cyclotron resonance which is polarization-sensitive. Fast hot-electron cooling was observed within the initial 50 ps after photo-excitation, which

agrees well with the rapid increase in photoconductivity obtained by the OPTPS measurement. The ability to measure cyclotron resonance on a sub-picosecond timescale is significant, since the hot-carrier cooling process usually happens on a similarly ultrafast timescale. By photo-exciting the electrons at different fluences, the conduction band non-parabolicity of InSb was proved by the increase of electron effective mass as a function of electron density, which is in good agreement with the *ab inito* quasiparticle band structure calculations. This time-resolved magneto-THz technique can be extended to investigate hot-carrier dynamics in other semiconductors and semiconductor heterostructures, which will contribute to the development of future ultrafast electronic devices.

The fundamental optoelectronic properties, in particular the charge-carrier dynamics and the carrier-lattice interaction, in the prototypical perovskite $MAPbI_3$ have been explored extensively in this thesis. The comparative study between $MAPbI_3$ single crystals and polycrystalline thin films provides a more thorough understanding of the underlying mechanism that determines the photovoltaic performance of perovskite-based solar cells. Although the effect of grain boundaries observed in polycrystalline thin films is usually believed to inhibit the charge-carrier transport and hence undermines the optoelectronic performance, studies performed in this thesis suggest that such effect is actually moderate in the $MAPbI_3$ thin films made by the thermal co-evaporation method [33] and the charge-carrier diffusion length of such films is found to be comparable to that of $MAPbI_3$ single crystals under normal solar cell operating conditions. This benign nature of the grain boundaries makes the $MAPbI_3$ polycrystalline thin film a promising candidate for developing large-scale photovoltaic devices, thanks to its ease of fabrication in contrast to the single crystal counterpart. Meanwhile, investigations of single crystals will continue to contribute to developing knowledge of the optoelectronic properties of MHPs, since their simpler morphology is more compatible with most theoretical studies such as *GW* and

Boltzmann transport calculations.

Examinations of the conduction band non-parabolicity of InSb have been shown to be a valuable endeavor. The time-resolved magneto-THz spectroscopy is a useful technique for probing the carrier effective mass as well as hot-carrier cooling process on an ultrafast timescale. The theoretical investigation of the non-parabolic band structure based on *GW* calculations provides further insight of the optoelectronic properties of narrow-gap semiconductors.

Looking to the future, it will be interesting to combine the temperature-dependent study on MHPs with the magneto-THz spectroscopy. While LO-phonon scattering has been shown to be the dominant electron scattering mechanism in MHPs, the effect of magnetic field and Landau quantization on the charge-carrier transport is yet to be understood. One crucial step is to perform cyclotron resonance measurements on MHPs, from which the knowledge of the electronic properties of MHPs including the band structure and hot-carrier cooling mechanism will be expanded. However, since the electrical mobility of MHPs is much smaller than that of narrow-gap semiconductors, it is more challenging to perform such experiment especially at THz frequencies. The much larger effective mass of MHPs compared to that of the narrow-gap semiconductors also requires significantly higher magnetic field for the cyclotron resonance measurements. Nevertheless, it is possible that with more advanced technique in making better-quality single-crystal perovskites, the charge carriers generated in the conduction band of MHPs may be able to complete at least one cyclotron orbit before getting scattered, so that the dependence of effective mass on the energy states and the magnetic field can be explored in more depth.

On the other hand, a comparative study on narrow-gap semiconductors with various structures such as nanowires (1D), nanomembranes (2D) and single crystals (3D) will be helpful to achieve a more complete picture of the charge-carrier dynamics in those materials under the effect of quantum confinement. Moreover, due to the

extremely high mobility, THz emission has been observed widely in narrow-gap semiconductors such as InAs and InSb [250]. The introduction of magnetic field which induces cyclotron resonance may facilitate the generation of circularly polarized THz pulse as opposed to the linearly polarized THz radiation generated by STE. Therefore, a better polarization control of the THz emission may be achieved, which will help to expand the applicability of THz spectroscopy.

Overall, THz spectroscopy is a powerful tool that helps to continuously gain more knowledge about the optoelectronic properties of those novel semiconductors, thanks to which the development of electronic devices with better performance is foreseeable in the near future.

Bibliography

[1] M. Faraday, "V. Experimental researches in electricity," *Philos. Trans. R. Soc. Lond.*, no. 122, pp. 125–162, 1832.

[2] W. Smith, "Effect of light on selenium during the passage of an electric current," *Nature*, vol. 7, p. 303, 1873.

[3] C. E. Fritts, "On a new form of selenium cell, and some electrical discoveries made by its use," *Am. J. Sci.*, no. 156, pp. 465–472, 1883.

[4] F. Braun, "Via the power line through sulfur metals," *Ann. Phys.*, vol. 229, no. 12, pp. 556–563, 1875.

[5] J. D. Cressler and G. Niu, *Silicon-germanium heterojunction bipolar transistors*. Artech House, 2003.

[6] A. H. Wilson, "The theory of electronic semi-conductors," *Proc. R. Soc. Lond.*, vol. 133, no. 822, pp. 458–491, 1931.

[7] D. L. Rode, "Electron transport in InSb, InAs, and InP," *Phys. Rev. B*, vol. 3, no. 10, p. 3287, 1971.

[8] E. Burstein, G. S. Picus, and H. A. Gebbie, "Cyclotron resonance at infrared frequencies in InSb at room temperature," *Phys. Rev.*, vol. 103, no. 3, p. 825, 1956.

[9] R. J. Keyes, S. Zwerdling, S. Foner, H. H. Kolm, and B. Lax, "Infrared cyclotron resonance in Bi, InSb, and InAs with high pulsed magnetic fields," *Phys. Rev.*, vol. 104, no. 6, p. 1804, 1956.

[10] E. D. Palik, G. S. Picus, S. Teitler, and R. F. Wallis, "Infrared cyclotron resonance in InSb," *Phys. Rev.*, vol. 122, no. 2, p. 475, 1961.

[11] J. Even, L. Pedesseau, J.-M. Jancu, and C. Katan, "Importance of spin–orbit coupling in hybrid organic/inorganic perovskites for photovoltaic applications," *J. Phys. Chem. Lett.*, vol. 4, no. 17, pp. 2999–3005, 2013.

[12] J. Even, L. Pedesseau, C. Katan, M. Kepenekian, J.-S. Lauret, D. Sapori, and E. Deleporte, "Solid-state physics perspective on hybrid perovskite semiconductors," *J. Phys. Chem. C*, vol. 119, no. 19, pp. 10161–10177, 2015.

[13] "Perovskite mineral data." http://webmineral.com/data/Perovskite.shtml#.XuDcn2pKjOQ. Accessed: 2020-06-10.

[14] H. L. Wells, "On the caesium- and the potassium-lead halides," *Am. J. Sci.*, no. 266, pp. 121–134, 1893.

[15] C. K. Møller, "Crystal structure and photoconductivity of caesium plumbohalides," *Nature*, vol. 182, no. 4647, pp. 1436–1436, 1958.

[16] D. Weber, "$CH_3NH_3PbX_3$, a Pb(II)-system with cubic perovskite structure," *Z. Naturforsch. B*, vol. 33, no. 12, pp. 1443–1445, 1978.

[17] "NREL best research-cell efficiencies." https://www.nrel.gov/pv/assets/pdfs/best-research-cell-efficiencies.20200311.pdf, 2020.

[18] P. S. Whitfield, N. Herron, W. E. Guise, K. Page, Y. Q. Cheng, I. Milas, and M. K. Crawford, "Structures, phase transitions and tricritical behavior of the

hybrid perovskite methylammonium lead iodide," *Sci. Rep.*, vol. 6, no. 1, pp. 1–16, 2016.

[19] K. S. Aleksandrov, "The sequences of structural phase transitions in perovskites," *Ferroelectrics*, vol. 14, no. 1, pp. 801–805, 1976.

[20] P. M. Woodward, "Octahedral tilting in perovskites. i. geometrical considerations," *Acta Crystallogr. B*, vol. 53, no. 1, pp. 32–43, 1997.

[21] C. J. Howard and H. T. Stokes, "Group-theoretical analysis of octahedral tilting in perovskites," *Acta Crystallogr. B*, vol. 54, no. 6, pp. 782–789, 1998.

[22] Z. Shi and A. H. Jayatissa, "Perovskites-based solar cells: a review of recent progress, materials and processing methods," *Materials*, vol. 11, no. 5, p. 729, 2018.

[23] M. I. Saidaminov, A. L. Abdelhady, B. Murali, E. Alarousu, V. M. Burlakov, W. Peng, I. Dursun, L. Wang, Y. He, G. Maculan, A. Goriely, T. Wu, O. F. Mohammed, and O. M. Bakr, "High-quality bulk hybrid perovskite single crystals within minutes by inverse temperature crystallization," *Nat. Commun.*, vol. 6, pp. 1–6, 2015.

[24] J. Peng, L. Cui, R. Li, Y. Xu, L. Jiang, Y. Li, W. Li, X. Tian, and Q. Lin, "Thick junction photodiodes based on crushed perovskite crystal/polymer composite films," *J. Mater. Chem. C*, vol. 7, no. 7, pp. 1859–1863, 2019.

[25] J. Ding, Q. Han, Q.-Q. Ge, D.-J. Xue, J.-Y. Ma, B.-Y. Zhao, Y.-X. Chen, J. Liu, D. B. Mitzi, and J.-S. Hu, "Fully air-bladed high-efficiency perovskite photovoltaics," *Joule*, vol. 3, no. 2, pp. 402–416, 2019.

[26] H. Chen, Z. Wei, X. Zheng, and S. Yang, "A scalable electrodeposition route to the low-cost, versatile and controllable fabrication of perovskite solar cells," *Nano Energy*, vol. 15, pp. 216–226, 2015.

[27] S.-G. Li, K.-J. Jiang, M.-J. Su, X.-P. Cui, J.-H. Huang, Q.-Q. Zhang, X.-Q. Zhou, L.-M. Yang, and Y.-L. Song, "Inkjet printing of $CH_3NH_3PbI_3$ on a mesoscopic TiO_2 film for highly efficient perovskite solar cells," *J. Mater. Chem. A*, vol. 3, no. 17, pp. 9092–9097, 2015.

[28] Q. Wang, Y. Shao, H. Xie, L. Lyu, X. Liu, Y. Gao, and J. Huang, "Qualifying composition dependent p and n self-doping in $CH_3NH_3PbI_3$," *Appl. Phys. Lett.*, vol. 105, no. 16, p. 163508, 2014.

[29] B. J. Kim, D. H. Kim, S. L. Kwon, S. Y. Park, Z. Li, K. Zhu, and H. S. Jung, "Selective dissolution of halide perovskites as a step towards recycling solar cells," *Nat. Commun.*, vol. 7, no. 1, pp. 1–9, 2016.

[30] J. Chen, J. Xu, L. Xiao, B. Zhang, S. Dai, and J. Yao, "Mixed-organic-cation $(FA)_x(MA)_{1-x}PbI_3$ planar perovskite solar cells with 16.48% efficiency via a low-pressure vapor-assisted solution process," *ACS Appl. Mater. Interfaces*, vol. 9, no. 3, pp. 2449–2458, 2017.

[31] L. Gil-Escrig, C. Momblona, M.-G. La-Placa, P. P. Boix, M. Sessolo, and H. J. Bolink, "Vacuum deposited triple-cation mixed-halide perovskite solar cells," *Adv. Energy Mater.*, vol. 8, no. 14, p. 1703506, 2018.

[32] A. M. Igual-Muñoz, J. Ávila, P. P. Boix, and H. J. Bolink, "$FAPb_0.5Sn_0.5I_3$: a narrow bandgap perovskite synthesized through evaporation methods for solar cell applications," *Solar RRL*, vol. 4, no. 2, p. 1900283, 2020.

[33] J. B. Patel, A. D. Wright, K. B. Lohmann, K. Peng, C. Q. Xia, J. M. Ball, N. K. Noel, T. W. Crothers, J. Wong-Leung, H. J. Snaith, L. M. Herz, and M. B.

Johnston, "Light absorption and recycling in hybrid metal halide perovskite photovoltaic devices," *Adv. Energy Mater.*, vol. 10, no. 10, p. 1903653, 2020.

[34] S. D. Stranks, G. E. Eperon, G. Grancini, C. Menelaou, M. J. P. Alcocer, T. Leijtens, L. M. Herz, A. Petrozza, and H. J. Snaith, "Electron-hole diffusion lengths exceeding 1 micrometer in an organometal trihalide perovskite absorber," *Science*, vol. 342, no. 6156, pp. 341–344, 2013.

[35] Q. Dong, Y. Fang, Y. Shao, P. Mulligan, J. Qiu, L. Cao, and J. Huang, "Electron-hole diffusion lengths $> 175\,\mu$m in solution-grown $CH_3NH_3PbI_3$ single crystals," *Science*, vol. 347, no. 6225, pp. 967–970, 2015.

[36] C. Wehrenfennig, M. Liu, H. J. Snaith, M. B. Johnston, and L. M. Herz, "Charge-carrier dynamics in vapour-deposited films of the organolead halide perovskite $CH_3NH_3PbI_{3-x}Cl_x$," *Energy Environ. Sci.*, vol. 7, no. 7, pp. 2269–2275, 2014.

[37] C. Wehrenfennig, G. E. Eperon, M. B. Johnston, H. J. Snaith, and L. M. Herz, "High charge carrier mobilities and lifetimes in organolead trihalide perovskites," *Adv. Mater.*, vol. 26, no. 10, pp. 1584–1589, 2014.

[38] R. L. Milot, G. E. Eperon, H. J. Snaith, M. B. Johnston, and L. M. Herz, "Temperature-dependent charge-carrier dynamics in $CH_3NH_3PbI_3$ perovskite thin films," *Adv. Funct. Mater.*, vol. 25, no. 39, pp. 6218–6227, 2015.

[39] H. Zhou, Q. Chen, G. Li, S. Luo, T.-b. Song, H.-S. Duan, Z. Hong, J. You, Y. Liu, and Y. Yang, "Interface engineering of highly efficient perovskite solar cells," *Science*, vol. 345, no. 6196, pp. 542–546, 2014.

[40] T.-B. Song, Q. Chen, H. Zhou, C. Jiang, H.-H. Wang, Y. M. Yang, Y. Liu, J. You, and Y. Yang, "Perovskite solar cells: film formation and properties," *J. Mater. Chem. A*, vol. 3, no. 17, pp. 9032–9050, 2015.

[41] C. L. Davies, M. R. Filip, J. B. Patel, T. W. Crothers, C. Verdi, A. D. Wright, R. L. Milot, F. Giustino, M. B. Johnston, and L. M. Herz, "Bimolecular recombination in methylammonium lead triiodide perovskite is an inverse absorption process," *Nat. Commun.*, vol. 9, pp. 1–9, 2018.

[42] Z.-K. Tan, R. S. Moghaddam, M. L. Lai, P. Docampo, R. Higler, F. Deschler, M. Price, A. Sadhanala, L. M. Pazos, D. Credgington, F. Hanusch, T. Bein, H. J. Snaith, and R. H. Friend, "Bright light-emitting diodes based on organometal halide perovskite," *Nat. Nanotechnol.*, vol. 9, no. 9, pp. 687–692, 2014.

[43] H. Zhu, Y. Fu, F. Meng, X. Wu, Z. Gong, Q. Ding, M. V. Gustafsson, M. T. Trinh, S. Jin, and X. Y. Zhu, "Lead halide perovskite nanowire lasers with low lasing thresholds and high quality factors," *Nat. Mater.*, vol. 14, no. 6, pp. 636–642, 2015.

[44] T. Leijtens, G. E. Eperon, N. K. Noel, S. N. Habisreutinger, A. Petrozza, and H. J. Snaith, "Stability of metal halide perovskite solar cells," *Adv. Energy Mater.*, vol. 5, no. 20, p. 1500963, 2015.

[45] H.-S. Kim, C.-R. Lee, J.-H. Im, K.-B. Lee, T. Moehl, A. Marchioro, S.-J. Moon, R. Humphry-Baker, J.-H. Yum, J. E. Moser, M. Grätzel, and N.-G. Park, "Lead iodide perovskite sensitized all-solid-state submicron thin film mesoscopic solar cell with efficiency exceeding 9%," *Sci. Rep.*, vol. 2, p. 591, 2012.

[46] S. N. Habisreutinger, T. Leijtens, G. E. Eperon, S. D. Stranks, R. J. Nicholas, and H. J. Snaith, "Carbon nanotube/polymer composites as a highly stable hole collection layer in perovskite solar cells," *Nano Lett.*, vol. 14, no. 10, pp. 5561–5568, 2014.

[47] J. Liu, S. Pathak, T. Stergiopoulos, T. Leijtens, K. Wojciechowski, S. Schumann, N. Kausch-Busies, and H. J. Snaith, "Employing PEDOT as the p-type

charge collection layer in regular organic–inorganic perovskite solar cells," *J. Phys. Chem. Lett.*, vol. 6, no. 9, pp. 1666–1673, 2015.

[48] M. Jørgensen, K. Norrman, S. A. Gevorgyan, T. Tromholt, B. Andreasen, and F. C. Krebs, "Stability of polymer solar cells," *Adv. Mater.*, vol. 24, no. 5, pp. 580–612, 2012.

[49] E. A. Katz, S. Gevorgyan, M. S. Orynbayev, and F. C. Krebs, "Out-door testing and long-term stability of plastic solar cells," *EPJ Appl. Phys.*, vol. 36, no. 3, pp. 307–311, 2006.

[50] C. H. Peters, I. T. Sachs-Quintana, W. R. Mateker, T. Heumueller, J. Rivnay, R. Noriega, Z. M. Beiley, E. T. Hoke, A. Salleo, and M. D. McGehee, "The mechanism of burn-in loss in a high efficiency polymer solar cell," *Adv. Mater.*, vol. 24, no. 5, pp. 663–668, 2012.

[51] N. K. Noel, S. D. Stranks, A. Abate, C. Wehrenfennig, S. Guarnera, A.-A. Haghighirad, A. Sadhanala, G. E. Eperon, S. K. Pathak, M. B. Johnston, A. Petrozza, L. M. Herz, and H. J. Snaith, "Lead-free organic–inorganic tin halide perovskites for photovoltaic applications," *Energy Environ. Sci.*, vol. 7, no. 9, pp. 3061–3068, 2014.

[52] F. Hao, C. C. Stoumpos, D. H. Cao, R. P. H. Chang, and M. G. Kanatzidis, "Lead-free solid-state organic–inorganic halide perovskite solar cells," *Nat. Photonics*, vol. 8, no. 6, p. 489, 2014.

[53] G. Nimtz, "Recombination in narrow-gap semiconductors," *Phys. Rep.*, vol. 63, no. 5, pp. 265–300, 1980.

[54] T. Ashley, A. R. Barnes, L. Buckle, S. Datta, A. B. Dean, M. T. Emery, M. Fearn, D. G. Hayes, K. P. Hilton, R. Jefferies, J. O. Maclean, S. J. Smith,

A. W.-H. Tang, D. J. Wallis, and P. J. Webber, "Novel InSb-based quantum well transistors for ultra-high speed, low power logic applications," in *Proceedings. 7th International Conference on Solid-State and Integrated Circuits Technology, 2004*, vol. 3, pp. 2253–2256, IEEE, 2004.

[55] I. Kimukin, N. Biyikli, T. Kartaloglu, O. Aytur, and E. Ozbay, "High-speed InSb photodetectors on GaAs for mid-IR applications," *IEEE J. Sel. Top. Quantum Electron.*, vol. 10, no. 4, pp. 766–770, 2004.

[56] S. Yamaguchi, T. Matsumoto, J. Yamazaki, N. Kaiwa, and A. Yamamoto, "Thermoelectric properties and figure of merit of a Te-doped InSb bulk single crystal," *Appl. Phys. Lett.*, vol. 87, no. 20, p. 201902, 2005.

[57] E. O. Kane, "Band structure of indium antimonide," *J. Phys. Chem. Solids*, vol. 1, no. 4, pp. 249–261, 1957.

[58] H. Kala, G. A. Umana-Membreno, G. Jolley, N. D. Akhavan, M. A. Patrashin, K. Akahane, J. Antoszewski, and L. Faraone, "Heavy and light hole transport in nominally undoped GaSb substrates," *Appl. Phys. Lett.*, vol. 106, no. 3, p. 032103, 2015.

[59] J. Buckeridge, T. D. Veal, C. R. A. Catlow, and D. O. Scanlon, "Intrinsic point defects and the n-and p-type dopability of the narrow gap semiconductors GaSb and InSb," *Phys. Rev. B*, vol. 100, no. 3, p. 035207, 2019.

[60] S. D. Mahanti and D. Bilc, "Electronic structure of defects and defect clusters in narrow band-gap semiconductor PbTe," *J. Phys. Condens. Matter*, vol. 16, no. 44, p. S5277, 2004.

[61] K. Ueno, E. G. Camargo, T. Katsumata, H. Goto, N. Kuze, Y. Kangawa, and K. Kakimoto, "InSb mid-infrared photon detector for room-temperature operation," *Jpn. J. Appl. Phys.*, vol. 52, no. 9R, p. 092202, 2013.

[62] T. Ashley, M. J. Buckle, M. T. Emeny, M. Fearn, D. G. Hayes, K. P. Hilton, R. Jefferies, T. Martin, K. J. Nash, T. J. Phillips, J. Powell, W. H. A. Tang, M. J. Uren, D. J. Wallis, P. J. Wilding, S. Datta, and R. Chau, "Indium antimonide based quantum well FETs for ultra-high speed electronics," in *2006 64th Device Research Conference*, pp. 201–202, IEEE, 2006.

[63] T. G. Tenev, A. Palyi, B. I. Mirza, G. R. Nash, M. Fearn, S. J. Smith, L. Buckle, M. T. Emeny, T. Ashley, J. H. Jefferson, and C. J. Lambert, "Energy level spectroscopy of InSb quantum wells using quantum-well LED emission," *Phys. Rev. B*, vol. 79, no. 8, p. 085301, 2009.

[64] B. I. Mirza, L. Buckle, and G. R. Nash, "Modification of the emission from InSb/AlInSb quantum-well light-emitting diodes using a small permanent magnet," *Semicond. Sci. Technol.*, vol. 25, no. 3, p. 035009, 2010.

[65] S. J. Smith, G. R. Nash, M. Fearn, L. Buckle, M. T. Emeny, and T. Ashley, "Photoluminescence from single InSb quantum wells," *Appl. Phys. Lett.*, vol. 88, no. 8, p. 081909, 2006.

[66] R. L. Kallaher, J. J. Heremans, N. Goel, S. J. Chung, and M. B. Santos, "Spin-orbit interaction determined by antilocalization in an InSb quantum well," *Phys. Rev. B*, vol. 81, no. 7, p. 075303, 2010.

[67] M. B. Johnston and L. M. Herz, "Hybrid perovskites for photovoltaics: charge-carrier recombination, diffusion, and radiative efficiencies," *Acc. Chem. Res.*, vol. 49, no. 1, pp. 146–154, 2016.

[68] S. M. Sze and K. K. Ng, *Physics of semiconductor devices*. John Wiley & Sons, 2006.

[69] M. C. Hoffmann, J. Hebling, H. Y. Hwang, K.-L. Yeh, and K. A. Nelson, "Impact ionization in InSb probed by terahertz pumpterahertz probe spectroscopy," *Phys. Rev. B*, vol. 79, no. 16, p. 161201, 2009.

[70] A. R. J. Marshall, J. P. R. David, and C. H. Tan, "Impact ionization in InAs electron avalanche photodiodes," *IEEE Trans. Electron Devices*, vol. 57, no. 10, pp. 2631–2638, 2010.

[71] T. W. Crothers, R. L. Milot, J. B. Patel, E. S. Parrott, J. Schlipf, P. Muller-Buschbaum, M. B. Johnston, and L. M. Herz, "Photon reabsorption masks intrinsic bimolecular charge-carrier recombination in $CH_3NH_3PbI_3$ perovskite," *Nano Lett.*, vol. 17, no. 9, pp. 5782–5789, 2017.

[72] F. Bloch, "Quantum mechanics of electrons in crystal lattices," *Z. Phys.*, vol. 52, pp. 555–600, 1928.

[73] J. Bardeen and W. Shockley, "Deformation potentials and mobilities in non-polar crystals," *Phys. Rev.*, vol. 80, no. 1, p. 72, 1950.

[74] C. Herring and E. Vogt, "Transport and deformation-potential theory for many-valley semiconductors with anisotropic scattering," *Phys. Rev.*, vol. 101, no. 3, p. 944, 1956.

[75] H. Fröhlich, "Electrons in lattice fields," *Adv. Phys.*, vol. 3, no. 11, pp. 325–361, 1954.

[76] W. A. Harrison, "Scattering of electrons by lattice vibrations in nonpolar crystals," *Phys. Rev.*, vol. 104, no. 5, p. 1281, 1956.

[77] H. J. G. Meijer and D. Polder, "Note on polar scattering of conduction electrons in regular crystals," *Physica*, vol. 19, no. 1-12, pp. 255–264, 1953.

[78] S. Baroni, P. Giannozzi, and A. Testa, "Greens-function approach to linear response in solids," *Phys. Rev. Lett.*, vol. 58, no. 18, p. 1861, 1987.

[79] S. Baroni, S. De Gironcoli, A. Dal Corso, and P. Giannozzi, "Phonons and related crystal properties from density-functional perturbation theory," *Rev. Mod. Phys.*, vol. 73, no. 2, p. 515, 2001.

[80] L. P. Kadanoff, *Quantum statistical mechanics*. CRC Press, 2018.

[81] S. Poncé, W. Li, S. Reichardt, and F. Giustino, "First-principles calculations of charge carrier mobility and conductivity in bulk semiconductors and two-dimensional materials," *Rep. Prog. Phys.*, vol. 83, no. 3, p. 036501, 2020.

[82] F. Giustino, "Electron-phonon interactions from first principles," *Rev. Mod. Phys.*, vol. 89, no. 1, p. 015003, 2017.

[83] S. Poncé, M. Schlipf, and F. Giustino, "Origin of low carrier mobilities in halide perovskites," *ACS Energy Lett.*, vol. 4, no. 2, pp. 456–463, 2019.

[84] A. F. Mayadas and M. Shatzkes, "Electrical-resistivity model for polycrystalline films: the case of arbitrary reflection at external surfaces," *Phys. Rev. B*, vol. 1, no. 4, p. 1382, 1970.

[85] T. Sun, B. Yao, A. P. Warren, K. Barmak, M. F. Toney, R. E. Peale, and K. R. Coffey, "Surface and grain-boundary scattering in nanometric Cu films," *Phys. Rev. B*, vol. 81, no. 15, p. 155454, 2010.

[86] W. Steinhögl, G. Schindler, G. Steinlesberger, and M. Engelhardt, "Size-dependent resistivity of metallic wires in the mesoscopic range," *Phys. Rev. B*, vol. 66, no. 7, p. 075414, 2002.

[87] P. Giannozzi, S. Baroni, N. Bonini, M. Calandra, R. Car, C. Cavazzoni, D. Ceresoli, G. L. Chiarotti, M. Cococcioni, I. Dabo, *et al.*, "QUANTUM

ESPRESSO: a modular and open-source software project for quantum simulations of materials," *J. Phys. Condens. Matter*, vol. 21, no. 39, p. 395502, 2009.

[88] T. Baikie, Y. Fang, J. M. Kadro, M. Schreyer, F. Wei, S. G. Mhaisalkar, M. Graetzel, and T. J. White, "Synthesis and crystal chemistry of the hybrid perovskite $CH_3NH_3PbI_3$ for solid-state sensitised solar cell applications," *J. Mater. Chem. A*, vol. 1, no. 18, pp. 5628–5641, 2013.

[89] M. A. Pérez-Osorio, R. L. Milot, M. R. Filip, J. B. Patel, L. M. Herz, M. B. Johnston, and F. Giustino, "Vibrational properties of the organic–inorganic halide perovskite $CH_3NH_3PbI_3$ from theory and experiment: factor group analysis, first-principles calculations, and low-temperature infrared spectra," *J. Phys. Chem. C*, vol. 119, no. 46, pp. 25703–25718, 2015.

[90] X. Gonze and C. Lee, "Dynamical matrices, Born effective charges, dielectric permittivity tensors, and interatomic force constants from density-functional perturbation theory," *Phys. Rev. B*, vol. 55, no. 16, p. 10355, 1997.

[91] R. H. Lyddane, R. G. Sachs, and E. Teller, "On the polar vibrations of alkali halides," *Phys. Rev.*, vol. 59, no. 8, p. 673, 1941.

[92] C. Motta, F. El-Mellouhi, S. Kais, N. Tabet, F. Alharbi, and S. Sanvito, "Revealing the role of organic cations in hybrid halide perovskite $CH_3NH_3PbI_3$," *Nat. Commun.*, vol. 6, p. 7026, 2015.

[93] X. Wu, L. Z. Tan, X. Shen, T. Hu, K. Miyata, M. T. Trinh, R. Li, R. Coffee, S. Liu, D. A. Egger, *et al.*, "Light-induced picosecond rotational disordering of the inorganic sublattice in hybrid perovskites," *Sci. Adv.*, vol. 3, no. 7, p. e1602388, 2017.

[94] S. Liu, F. Zheng, I. Grinberg, and A. M. Rappe, "Photoferroelectric and photopiezoelectric properties of organometal halide perovskites," *J. Phys. Chem. Lett.*, vol. 7, no. 8, pp. 1460–1465, 2016.

[95] M. Coll, A. Gomez, E. Mas-Marza, O. Almora, G. Garcia-Belmonte, M. Campoy-Quiles, and J. Bisquert, "Polarization switching and light-enhanced piezoelectricity in lead halide perovskites," *J. Phys. Chem. Lett.*, vol. 6, no. 8, pp. 1408–1413, 2015.

[96] C.-C. Wu, "Free-carrier absorption in n-type InSb at low temperatures and quantizing magnetic fields," *Physica B: Condensed Matter*, vol. 165, pp. 851–852, 1990.

[97] C.-C. Wu, J. Tsai, and C.-J. Lin, "Effect of nonparabolicity on free-carrier absorption in degenerate n-type indium antimonide in quantizing magnetic fields," *Physica B: Condensed Matter*, vol. 176, no. 1-2, pp. 159–164, 1992.

[98] E. O. Kane, "Band structure of indium antimonide," *J. Phys. Chem. Solids*, vol. 1, no. 4, pp. 249–261, 1957.

[99] P. Y. Yu and M. Cardona, *Fundamentals of semiconductors: physics and materials properties*. Springer, 1996.

[100] J. D. Fan, Y. M. Malozovsky, and D. Bagayoko, "Band structures of narrow gap semiconductors in terms of Coulombic polaron effect," *J. Supercond. Nov. Magn.*, vol. 23, no. 5, pp. 665–674, 2010.

[101] G. Dresselhaus, A. Kip, C. Kittel, and G. Wagoner, "Cyclotron and spin resonance in indium antimonide," *Phys. Rev.*, vol. 98, no. 2, p. 556, 1955.

[102] G. Landwehr and E. I. Rashba, *Landau level spectroscopy*. Elsevier, 2012.

[103] A. Lobad and L. A. Schlie, "Carrier thermalization, cooling and diffusion in InSb through a nonlinear pump-probe technique," *J. Appl. Phys.*, vol. 95, no. 1, pp. 97–101, 2004.

[104] R. A. Stradling and R. A. Wood, "The application of the magnetophonon effect to a study of hot electron phenomena in InSb," *J. Phys. C*, vol. 3, no. 12, p. 2425, 1970.

[105] J. P. Martin and J. B. Mead, "Two-phonon scattering processes in the energy relaxation time of hot electrons in InSb," *Appl. Phys. Lett.*, vol. 17, no. 8, pp. 320–322, 1970.

[106] K. Shimomae, Y. Hirose, and C. Hamaguchi, "Energy-loss mechanisms of hot electrons in n-InSb," *J. Phys. C*, vol. 14, no. 33, p. 5151, 1981.

[107] A. K. Ghorai and D. P. Bhattacharya, "Effect of non-parabolic band on the scattering rates of free electrons in high purity semiconductors at low lattice temperatures," *Phys. Status Solidi*, vol. 163, no. 1, pp. 247–258, 1991.

[108] D. Matz, "Hot-carrier distribution function in nonparabolic energy bands," *J. Phys. Chem. Solids*, vol. 28, no. 3, pp. 373–382, 1967.

[109] G. Shkerdin, J. Stiens, and R. Vounckx, "Hot free-electron absorption in non-parabolic III-V semiconductors at mid-infrared wavelengths," *J. Appl. Phys.*, vol. 85, no. 7, pp. 3792–3806, 1999.

[110] H. Kahlert and G. Bauer, "Hot-electron-phonon interaction in the nonparabolic conduction band of degenerate InSb at 4.2 K," *Phys. Rev. B*, vol. 7, no. 6, p. 2670, 1973.

[111] M. A. Perez-Osorio, Q. Lin, R. T. Phillips, R. L. Milot, L. M. Herz, M. B. Johnston, and F. Giustino, "Raman spectrum of the organic–inorganic halide per-

ovskite $CH_3NH_3PbI_3$ from first principles and high-resolution low-temperature Raman measurements," *J. Phys. Chem. C*, vol. 122, no. 38, pp. 21703–21717, 2018.

[112] B. F. Miao, S. Y. Huang, D. Qu, and C. L. Chien, "Inverse spin Hall effect in a ferromagnetic metal," *Phys. Rev. Lett.*, vol. 111, no. 6, p. 066602, 2013.

[113] T. Seifert, S. Jaiswal, M. Sajadi, G. Jakob, S. Winnerl, M. Wolf, M. Kläui, and T. Kampfrath, "Ultrabroadband single-cycle terahertz pulses with peak fields of 300 $kVcm^{-1}$ from a metallic spintronic emitter," *Appl. Phys. Lett.*, vol. 110, no. 25, p. 252402, 2017.

[114] I. Wilke and S. Sengupta, "Nonlinear optical techniques for terahertz pulse generation and detection — optical rectification and electrooptic sampling," in *Terahertz Spectroscopy*, pp. 59–90, CRC Press, 2017.

[115] S. S. Dhillon, M. S. Vitiello, E. H. Linfield, A. G. Davies, M. C. Hoffmann, J. Booske, C. Paoloni, M. Gensch, P. Weightman, G. P. Williams, *et al.*, "The 2017 terahertz science and technology roadmap," *J. Phys. D: Appl. Phys.*, vol. 50, no. 4, p. 043001, 2017.

[116] A. Yariv and P. Yeh, *Optical waves in crystals*, vol. 5. Wiley New York, 1984.

[117] P. C. M. Planken, H.-K. Nienhuys, H. J. Bakker, and T. Wenckebach, "Measurement and calculation of the orientation dependence of terahertz pulse detection in ZnTe," *Josa B*, vol. 18, no. 3, pp. 313–317, 2001.

[118] N. C. J. van der Valk, T. Wenckebach, and P. C. M. Planken, "Full mathematical description of electro-optic detection in optically isotropic crystals," *Josa B*, vol. 21, no. 3, pp. 622–631, 2004.

[119] N. C. J. Van der Valk, W. A. M. van der Marel, and P. C. M. Planken, "Terahertz polarization imaging," *Opt. Lett.*, vol. 30, no. 20, pp. 2802–2804, 2005.

[120] P. S. Pershan, "Magneto-optical effects," *J. Appl. Phys.*, vol. 38, no. 3, pp. 1482–1490, 1967.

[121] J. Kerr, "XLIII. On rotation of the plane of polarization by reflection from the pole of a magnet," *London Edinburgh Dublin Philos. Mag. J. Sci.*, vol. 3, no. 19, pp. 321–343, 1877.

[122] J. Kerr, "Xxiv. On reflection of polarized light from the equatorial surface of a magnet," *London Edinburgh Dublin Philos. Mag. J. Sci.*, vol. 5, no. 30, pp. 161–177, 1878.

[123] K. Peng, D. Jevtics, F. Zhang, S. Sterzl, D. A. Damry, M. U. Rothmann, B. Guilhabert, M. J. Strain, H. H. Tan, L. M. Herz, *et al.*, "Three-dimensional cross-nanowire networks recover full terahertz state," *Science*, vol. 368, no. 6490, pp. 510–513, 2020.

[124] L. M. Herz, "How lattice dynamics moderate the electronic properties of metal-halide perovskites," *J. Phys. Chem. Lett.*, vol. 9, no. 23, pp. 6853–6863, 2018.

[125] M. Sendner, P. K. Nayak, D. A. Egger, S. Beck, C. Müller, B. Epding, W. Kowalsky, L. Kronik, H. J. Snaith, A. Pucci, and R. Lovrinčić, "Optical phonons in methylammonium lead halide perovskites and implications for charge transport," *Mater. Horiz.*, vol. 3, pp. 613–620, 2016.

[126] A. Poglitsch and D. Weber, "Dynamic disorder in methylammoniumtrihalogenoplumbates (ii) observed by millimeter-wave spectroscopy," *J. Chem. Phys.*, vol. 87, no. 11, pp. 6373–6378, 1987.

[127] P. Kužel and H. Němec, "Terahertz conductivity in nanoscaled systems: effective medium theory aspects," *J. Phys. D: Appl. Phys.*, vol. 47, no. 37, p. 374005, 2014.

[128] C. L. Davies, J. B. Patel, C. Q. Xia, L. M. Herz, and M. B. Johnston, "Temperature-dependent refractive index of quartz at terahertz frequencies," *J. Infrared Millim. Terahertz Waves*, vol. 39, no. 12, pp. 1236–1248, 2018.

[129] H. Hempel, T. Unold, and R. Eichberger, "Measurement of charge carrier mobilities in thin films on metal substrates by reflection time resolved terahertz spectroscopy," *Opt. Express*, vol. 25, no. 15, pp. 17227–17236, 2017.

[130] A. M. Ulatowski, L. M. Herz, and M. B. Johnston, "Terahertz conductivity analysis for highly doped thin-film semiconductors." http://dx.doi.org/10.1007/s10762-020-00739-6, 2020.

[131] F. D'Angelo, H. Němec, S. H. Parekh, P. Kužel, M. Bonn, and D. Turchinovich, "Self-referenced ultra-broadband transient terahertz spectroscopy using air-photonics," *Opt. Express*, vol. 24, no. 9, pp. 10157–10171, 2016.

[132] H.-K. Nienhuys and V. Sundström, "Intrinsic complications in the analysis of optical-pump, terahertz probe experiments," *Phys. Rev. B*, vol. 71, no. 23, p. 235110, 2005.

[133] J. Lloyd-Hughes and T.-I. Jeon, "A review of the terahertz conductivity of bulk and nano-materials," *J. Infrared Millim. Terahertz Waves*, vol. 33, no. 9, pp. 871–925, 2012.

[134] H. J. Joyce, J. L. Boland, C. L. Davies, S. A. Baig, and M. B. Johnston, "A review of the electrical properties of semiconductor nanowires: insights gained from terahertz conductivity spectroscopy," *Semicond. Sci. Technol.*, vol. 31, no. 10, p. 103003, 2016.

[135] C. La-o-vorakiat, L. Cheng, T. Salim, R. A. Marcus, M.-E. Michel-Beyerle, Y. M. Lam, and E. E. M. Chia, "Phonon features in terahertz photoconductivity spectra due to data analysis artifact: a case study on organometallic halide perovskites," *Appl. Phys. Lett.*, vol. 110, no. 12, p. 123901, 2017.

[136] H. J. Joyce, C. J. Docherty, Q. Gao, H. H. Tan, C. Jagadish, J. Lloyd-Hughes, L. M. Herz, and M. B. Johnston, "Electronic properties of GaAs, InAs and InP nanowires studied by terahertz spectroscopy," *Nanotechnology*, vol. 24, no. 21, p. 214006, 2013.

[137] A. D. Wright, C. Verdi, R. L. Milot, G. E. Eperon, M. A. Pérez-Osorio, H. J. Snaith, F. Giustino, M. B. Johnston, and L. M. Herz, "Electron–phonon coupling in hybrid lead halide perovskites," *Nat. Commun.*, vol. 7, no. 11755, pp. 1–9, 2016.

[138] H. A. Kramers, "Some remarks on the theory of absorption and refraction of X-rays," *Nature*, vol. 117, no. 2952, pp. 774–775, 1926.

[139] R. d. L. Kronig, "On the theory of dispersion of X-rays," *Josa*, vol. 12, no. 6, pp. 547–557, 1926.

[140] A. B. Kuzmenko, "Kramers-kronig constrained variational analysis of optical spectra," *Rev. Sci. Instrum.*, vol. 76, no. 8, p. 083108, 2005.

[141] A. B. Kuzmenko, "Guide to RefFIT: software to fit optical spectra." https://optics.unige.ch/alexey/reffit.html, 2004.

[142] A. Goetzberger, J. Knobloch, and B. Voss, *Crystalline silicon solar cells*. Chichester: John Wiley & Sons Ltd., 1998.

[143] A. Kojima, K. Teshima, Y. Shirai, and T. Miyasaka, "Organometal halide perovskites as visible-light sensitizers for photovoltaic cells," *J. Am. Chem. Soc.*, vol. 131, no. 17, pp. 6050–6051, 2009.

[144] M. A. Loi and J. C. Hummelen, "Hybrid solar cells: perovskites under the sun," *Nat. Mater.*, vol. 12, no. 12, p. 1087, 2013.

[145] H. J. Snaith, "Perovskites: the emergence of a new era for low-cost, high-efficiency solar cells," *J. Phys. Chem. Lett.*, vol. 4, no. 21, pp. 3623–3630, 2013.

[146] H.-S. Kim, S. H. Im, and N.-G. Park, "Organolead halide perovskite: new horizons in solar cell research," *J. Phys. Chem. C*, vol. 118, no. 11, pp. 5615–5625, 2014.

[147] D. Shi, V. Adinolfi, R. Comin, M. Yuan, E. Alarousu, A. Buin, Y. Chen, S. Hoogland, A. Rothenberger, K. Katsiev, Y. Losovyj, X. Zhang, P. A. Dowben, O. F. Mohammed, E. H. Sargent, and O. M. Bakr, "Low trap-state density and long carrier diffusion in organolead trihalide perovskite single crystals," *Science*, vol. 347, no. 6221, pp. 519–522, 2015.

[148] N. J. Jeon, J. H. Noh, Y. C. Kim, W. S. Yang, S. Ryu, and S. I. Seok, "Solvent engineering for high-performance inorganic-organic hybrid perovskite solar cells," *Nat. Mater.*, vol. 13, no. 9, pp. 897–903, 2014.

[149] M. Xiao, F. Huang, W. Huang, Y. Dkhissi, Y. Zhu, J. Etheridge, A. Gray-Weale, U. Bach, Y.-B. Cheng, and L. Spiccia, "A fast deposition-crystallization procedure for highly efficient lead iodide perovskite thin-film solar cells," *Angew. Chem. Int. Ed.*, vol. 53, no. 37, pp. 9898–9903, 2014.

[150] W. Nie, H. Tsai, R. Asadpour, J.-C. Blancon, A. J. Neukirch, G. Gupta, J. J. Crochet, M. Chhowalla, S. Tretiak, M. A. Alam, H.-L. Wang, and A. Mohite,

"High-efficiency solution-processed perovskite solar cells with millimeter-scale grains," *Science*, vol. 347, no. 6221, pp. 522–525, 2015.

[151] J. Burschka, N. Pellet, S.-J. Moon, R. Humphry-Baker, P. Gao, M. K. Nazeeruddin, and M. Grätzel, "Sequential deposition as a route to high-performance perovskite-sensitized solar cells," *Nature*, vol. 499, no. 7458, pp. 316–319, 2013.

[152] J. Yin, H. Qu, J. Cao, H. Tai, J. Li, and N. Zheng, "Vapor-assisted crystallization control toward high performance perovskite photovoltaics with over 18% efficiency in the ambient atmosphere," *J. Mater. Chem. A*, vol. 4, no. 34, pp. 13203–13210, 2016.

[153] P. Fan, D. Gu, G.-X. Liang, J.-T. Luo, J.-L. Chen, Z.-H. Zheng, and D.-P. Zhang, "High-performance perovskite $CH_3NH_3PbI_3$ thin films for solar cells prepared by single-source physical vapour deposition," *Sci. Rep.*, vol. 6, p. 29910, 2016.

[154] S.-Y. Hsiao, H.-L. Lin, W.-H. Lee, W.-L. Tsai, K.-M. Chiang, W.-Y. Liao, C.-Z. Ren-Wu, C.-Y. Chen, and H.-W. Lin, "Efficient all-vacuum deposited perovskite solar cells by controlling reagent partial pressure in high vacuum," *Adv. Mater.*, vol. 28, no. 32, pp. 7013–7019, 2016.

[155] C. Momblona, L. Gil-Escrig, E. Bandiello, E. M. Hutter, M. Sessolo, K. Lederer, J. Blochwitz-Nimoth, and H. J. Bolink, "Efficient vacuum deposited p-i-n and n-i-p perovskite solar cells employing doped charge transport layers," *Energy Environ. Sci.*, vol. 9, no. 11, pp. 3456–3463, 2016.

[156] L. M. Herz, "Charge-carrier mobilities in metal halide perovskites: fundamental mechanisms and limits," *ACS Energy Lett.*, vol. 2, no. 7, pp. 1539–1548, 2017.

[157] C. C. Stoumpos, C. D. Malliakas, and M. G. Kanatzidis, "Semiconducting tin and lead iodide perovskites with organic cations: phase transitions, high mo-

bilities, and near-infrared photoluminescent properties," *Inorg. Chem.*, vol. 52, no. 15, pp. 9019–9038, 2013.

[158] S. M. H. Rizvi and B. Mazhari, "An improved method for extraction of mobility from space charge limited current in organic semiconductor films," *J. Appl. Phys.*, vol. 121, no. 15, p. 155501, 2017.

[159] X. Y. Chin, D. Cortecchia, J. Yin, A. Bruno, and C. Soci, "Lead iodide perovskite light-emitting field-effect transistor," *Nat. Commun.*, vol. 6, pp. 1–9, 2015.

[160] M.-J. Zhang, N. Wang, S.-P. Pang, Q. Lv, C.-S. Huang, Z.-M. Zhou, and F.-X. Ji, "Carrier transport improvement of $CH_3NH_3PbI_3$ film by methylamine gas treatment," *ACS Appl. Mater. Interfaces*, vol. 8, no. 45, pp. 31413–31418, 2016.

[161] E. L. Unger, E. T. Hoke, C. D. Bailie, W. H. Nguyen, A. R. Bowring, T. Heumüller, M. G. Christoforo, and M. D. McGehee, "Hysteresis and transient behavior in current–voltage measurements of hybrid-perovskite absorber solar cells," *Energy Environ. Sci.*, vol. 7, no. 11, pp. 3690–3698, 2014.

[162] S. Meloni, T. Moehl, W. Tress, M. Franckevičius, M. Saliba, Y. H. Lee, P. Gao, M. K. Nazeeruddin, S. M. Zakeeruddin, U. Rothlisberger, and M. Graetzel, "Ionic polarization-induced current–voltage hysteresis in $CH_3NH_3PbX_3$ perovskite solar cells," *Nat. Commun.*, vol. 7, no. 1, pp. 1–9, 2016.

[163] D. Lan, "The physics of ion migration in perovskite solar cells: insights into hysteresis, device performance, and characterization," *Prog. Photovolt.*, vol. 28, pp. 533–537, 2020.

[164] E. M. Hutter, G. E. Eperon, S. D. Stranks, and T. J. Savenije, "Charge carriers in planar and meso-structured organic–inorganic perovskites: mobilities, life-

times, and concentrations of trap states," *J. Phys. Chem. Lett.*, vol. 6, no. 15, pp. 3082–3090, 2015.

[165] O. G. Reid, M. Yang, N. Kopidakis, K. Zhu, and G. Rumbles, "Grain-size-limited mobility in methylammonium lead iodide perovskite thin films," *ACS Energy Lett.*, vol. 1, no. 3, pp. 561–565, 2016.

[166] D. H. Kim, J. Park, Z. Li, M. Yang, J.-S. Park, I. J. Park, J. Y. Kim, J. J. Berry, G. Rumbles, and K. Zhu, "300% enhancement of carrier mobility in uniaxial-oriented perovskite films formed by topotactic-oriented attachment," *Adv. Mater.*, vol. 29, no. 23, p. 1606831, 2017.

[167] O. E. Semonin, G. A. Elbaz, D. B. Straus, T. D. Hull, D. W. Paley, A. M. Van der Zande, J. C. Hone, I. Kymissis, C. R. Kagan, X. Roy, and J. S. Owen, "Limits of carrier diffusion in n-type and p-type $CH_3NH_3PbI_3$ perovskite single crystals," *J. Phys. Chem. Lett.*, vol. 7, no. 17, pp. 3510–3518, 2016.

[168] D. A. Valverde-Chávez, C. S. Ponseca, C. C. Stoumpos, A. Yartsev, M. G. Kanatzidis, V. Sundström, and D. G. Cooke, "Intrinsic femtosecond charge generation dynamics in single crystal $CH_3NH_3PbI_3$," *Energy Environ. Sci.*, vol. 8, no. 12, pp. 3700–3707, 2015.

[169] C. A. Schneider, W. S. Rasband, and K. W. Eliceiri, "NIH Image to ImageJ: 25 years of image analysis," *Nat. Methods*, vol. 9, no. 7, pp. 671–675, 2012.

[170] S. Jariwala, H. Sun, G. W. Adhyaksa, A. Lof, L. A. Muscarella, B. Ehrler, E. C. Garnett, and D. S. Ginger, "Local crystal misorientation influences non-radiative recombination in halide perovskites," *Joule*, vol. 3, no. 12, pp. 3048–3060, 2019.

[171] P. Scherrer, "Determination of the internal structure and the size of colloidal particles by means of X-rays," in *Colloid Chemistry A Textbook*, pp. 387–409, Springer, 1912.

[172] A. L. Patterson, "The Scherrer formula for X-ray particle size determination," *Phys. Rev.*, vol. 56, no. 10, p. 978, 1939.

[173] A. Pisoni, J. Jacimovic, O. S. Barisic, M. Spina, R. Gaál, L. Forró, and E. Horváth, "Ultra-low thermal conductivity in organic–inorganic hybrid perovskite $CH_3NH_3PbI_3$," *J. Phys. Chem. Lett.*, vol. 5, no. 14, pp. 2488–2492, 2014.

[174] R. Heiderhoff, T. Haeger, N. Pourdavoud, T. Hu, M. Al-Khafaji, A. Mayer, Y. Chen, H.-C. Scheer, and T. Riedl, "Thermal conductivity of methylammonium lead halide perovskite single crystals and thin films: a comparative study," *J. Phys. Chem. C*, vol. 121, no. 51, pp. 28306–28311, 2017.

[175] A. Gold-Parker, P. M. Gehring, J. M. Skelton, I. C. Smith, D. Parshall, J. M. Frost, H. I. Karunadasa, A. Walsh, and M. F. Toney, "Acoustic phonon lifetimes limit thermal transport in methylammonium lead iodide," *Proc. Natl. Acad. Sci.*, vol. 115, no. 47, pp. 11905–11910, 2018.

[176] G. S. Nolas and H. J. Goldsmid, "Thermal conductivity of semiconductors," in *Thermal Conductivity*, pp. 105–121, Springer, 2004.

[177] P. Giannozzi, O. Andreussi, T. Brumme, O. Bunau, M. B. Nardelli, M. Calandra, R. Car, C. Cavazzoni, D. Ceresoli, M. Cococcioni, *et al.*, "Advanced capabilities for materials modelling with QUANTUM ESPRESSO," *J. Phys. Condens. Matter*, vol. 29, no. 46, p. 465901, 2017.

[178] M. J. Van Setten, M. Giantomassi, E. Bousquet, M. J. Verstraete, D. R. Hamann, X. Gonze, and G.-M. Rignanese, "The PseudoDojo: training and

grading a 85 element optimized norm-conserving pseudopotential table," *Comput. Phys. Commun.*, vol. 226, pp. 39–54, 2018.

[179] D. Sangalli, A. Ferretti, H. Miranda, C. Attaccalite, I. Marri, E. Cannuccia, P. Melo, M. Marsili, F. Paleari, A. Marrazzo, *et al.*, "Many-body perturbation theory calculations using the yambo code," *J. Phys. Condens. Matter*, vol. 31, no. 32, p. 325902, 2019.

[180] R. W. Godby and R. J. Needs, "Metal-insulator transition in Kohn-Sham theory and quasiparticle theory," *Phys. Rev. Lett.*, vol. 62, pp. 1169–1172, Mar 1989.

[181] F. Bruneval and X. Gonze, "Accurate *GW* self-energies in a plane-wave basis using only a few empty states: Towards large systems," *Phys. Rev. B*, vol. 78, p. 085125, 2008.

[182] S. Poncé, E. R. Margine, C. Verdi, and F. Giustino, "EPW: Electron-phonon coupling, transport and superconducting properties using maximally localized Wannier functions," *Comput. Phys. Commun.*, vol. 209, pp. 116–133, 2016.

[183] G. Pizzi, V. Vitale, R. Arita, S. Blügel, F. Freimuth, G. Géranton, M. Gibertini, D. Gresch, C. Johnson, T. Koretsune, *et al.*, "Wannier90 as a community code: new features and applications," *J. Phys. Condens. Matter*, vol. 32, no. 16, p. 165902, 2020.

[184] J. S. J. Hargreaves, "Some considerations related to the use of the Scherrer equation in powder X-ray diffraction as applied to heterogeneous catalysts," *Catal. Struct. React.*, vol. 2, no. 1-4, pp. 33–37, 2016.

[185] J. J. J. Yang, P. D. Dapkus, R. D. Dupuis, and R. D. Yingling, "Electrical properties of polycrystalline GaAs films," *J. Appl. Phys.*, vol. 51, no. 7, pp. 3794–3800, 1980.

[186] C. M. Wolfe, G. E. Stillman, and W. T. Lindley, "Electron mobility in high-purity GaAs," *J. Appl. Phys.*, vol. 41, no. 7, pp. 3088–3091, 1970.

[187] K. Wu, A. Bera, C. Ma, Y. Du, Y. Yang, L. Li, and T. Wu, "Temperature-dependent excitonic photoluminescence of hybrid organometal halide perovskite films," *Phys. Chem. Chem. Phys.*, vol. 16, no. 41, pp. 22476–22481, 2014.

[188] J. M. Frost, "Calculating polaron mobility in halide perovskites," *Phys. Rev. B*, vol. 96, no. 19, p. 195202, 2017.

[189] M. Schlipf, S. Poncé, and F. Giustino, "Carrier lifetimes and polaronic mass enhancement in the hybrid halide perovskite $CH_3NH_3PbI_3$ from multiphonon Fröhlich coupling," *Phys. Rev. Lett.*, vol. 121, p. 086402, Aug 2018.

[190] M. J. Trimpl, A. D. Wright, K. Schutt, L. R. V. Buizza, Z. Wang, M. B. Johnston, H. J. Snaith, P. Müller-Buschbaum, and L. M. Herz, "Charge-carrier trapping and radiative recombination in metal halide perovskite semiconductors," *Adv. Funct. Mater.*, vol. 30, p. 2004312, 2020.

[191] C. Wehrenfennig, M. Liu, H. J. Snaith, M. B. Johnston, and L. M. Herz, "Homogeneous emission line broadening in the organo lead halide perovskite $CH_3NH_3PbI_{3-x}Cl_x$," *J. Phys. Chem. Lett.*, vol. 5, no. 8, pp. 1300–1306, 2014.

[192] C. Quarti, G. Grancini, E. Mosconi, P. Bruno, J. M. Ball, M. M. Lee, H. J. Snaith, A. Petrozza, and F. De Angelis, "The Raman spectrum of the $CH_3NH_3PbI_3$ hybrid perovskite: interplay of theory and experiment," *J. Phys. Chem. Lett.*, vol. 5, no. 2, pp. 279–284, 2013.

[193] M. Ledinsky, P. Loper, B. Niesen, J. Holovsky, S.-J. Moon, J.-H. Yum, S. De Wolf, A. Fejfar, and C. Ballif, "Raman spectroscopy of organic–inorganic halide perovskites," *J. Phys. Chem. Lett.*, vol. 6, no. 3, pp. 401–406, 2015.

[194] N. Onoda-Yamamuro, T. Matsuo, and H. Suga, "Calorimetric and IR spectroscopic studies of phase transitions in methylammonium trihalogenoplumbates (II)," *J. Phys. Chem. Solids*, vol. 51, no. 12, pp. 1383–1395, 1990.

[195] E. Mosconi, C. Quarti, T. Ivanovska, G. Ruani, and F. De Angelis, "Structural and electronic properties of organo-halide lead perovskites: a combined ir-spectroscopy and ab initio molecular dynamics investigation," *Phys. Chem. Chem. Phys.*, vol. 16, no. 30, pp. 16137–16144, 2014.

[196] T. Glaser, C. Muller, M. Sendner, C. Krekeler, O. E. Semonin, T. D. Hull, O. Yaffe, J. S. Owen, W. Kowalsky, A. Pucci, *et al.*, "Infrared spectroscopic study of vibrational modes in methylammonium lead halide perovskites," *J. Phys. Chem. Lett.*, vol. 6, no. 15, pp. 2913–2918, 2015.

[197] Y. Zhou, L. You, S. Wang, Z. Ku, H. Fan, D. Schmidt, A. Rusydi, L. Chang, L. Wang, P. Ren, *et al.*, "Giant photostriction in organic–inorganic lead halide perovskites," *Nat. Commun.*, vol. 7, no. 1, pp. 1–8, 2016.

[198] T.-C. Wei, H.-P. Wang, T.-Y. Li, C.-H. Lin, Y.-H. Hsieh, Y.-H. Chu, and J.-H. He, "Photostriction of $CH_3NH_3PbBr_3$ perovskite crystals," *Adv. Mater.*, vol. 29, no. 35, p. 1701789, 2017.

[199] M. T. Weller, O. J. Weber, P. F. Henry, A. M. Di Pumpo, and T. C. Hansen, "Complete structure and cation orientation in the perovskite photovoltaic methylammonium lead iodide between 100 and 352K," *Chem. Commun.*, vol. 51, no. 20, pp. 4180–4183, 2015.

[200] A. A. Bakulin, O. Selig, H. J. Bakker, Y. L. Rezus, C. Muller, T. Glaser, R. Lovrincic, Z. Sun, Z. Chen, A. Walsh, *et al.*, "Real-time observation of organic cation reorientation in methylammonium lead iodide perovskites," *J. Phys. Chem. Lett.*, vol. 6, no. 18, pp. 3663–3669, 2015.

[201] D. Zhao, H. Hu, R. Haselsberger, R. A. Marcus, M.-E. Michel-Beyerle, Y. M. Lam, J.-X. Zhu, C. La-o vorakiat, M. C. Beard, and E. E. M. Chia, "Monitoring electron–phonon interactions in lead halide perovskites using time-resolved THz spectroscopy," *ACS Nano*, vol. 13, no. 8, pp. 8826–8835, 2019.

[202] T. Salim, J. Kadro, M.-T. Khuc, R. Haselsberger, L. Cheng, H. Xia, G. G. Gurzadyan, H. Su, Y. M. Lam, R. A. Marcus, *et al.*, "Elucidating the role of disorder and free-carrier recombination kinetics in $CH_3NH_3PbI_3$ perovskite films," *Nat. Commun.*, vol. 6, no. 1, pp. 1–8, 2015.

[203] L. D. Whalley, J. M. Skelton, J. M. Frost, and A. Walsh, "Phonon anharmonicity, lifetimes, and thermal transport in $CH_3NH_3PbI_3$ from many-body perturbation theory," *Phys. Rev. B*, vol. 94, no. 22, p. 220301, 2016.

[204] N. R. Couch, M. J. Kelly, H. Spooner, and T. M. Kerr, "Hot electron injection in millimetre wave Gunn diodes," *Solid State Electron.*, vol. 32, no. 12, pp. 1685–1688, 1989.

[205] A. Förster, M. I. Lepsa, D. Freundt, J. Stock, and S. Montanari, "Hot electron injector Gunn diode for advanced driver assistance systems," *Appl. Phys. A*, vol. 87, no. 3, pp. 545–558, 2007.

[206] F. Capasso, "Physics of avalanche photodiodes," in *Semiconductors and Semimetals*, vol. 22, pp. 1–172, Elsevier, 1985.

[207] J. Abautret, J. P. Perez, A. Evirgen, J. Rothman, A. Cordat, and P. Christol, "Characterization of midwave infrared InSb avalanche photodiode," *J. Appl. Phys.*, vol. 117, no. 24, p. 244502, 2015.

[208] R. T. Ross and A. J. Nozik, "Efficiency of hot-carrier solar energy converters," *J. Appl. Phys.*, vol. 53, no. 5, pp. 3813–3818, 1982.

[209] D. König, K. Casalenuovo, Y. Takeda, G. Conibeer, J. F. Guillemoles, R. Patterson, L. M. Huang, and M. A. Green, "Hot carrier solar cells: principles, materials and design," *Physica E Low Dimens. Syst. Nanostruct.*, vol. 42, no. 10, pp. 2862–2866, 2010.

[210] F. M. Klaassen, "On the influence of hot carrier effects on the thermal noise of field-effect transistors," *IEEE Trans. Electron Devices*, vol. 17, no. 10, pp. 858–862, 1970.

[211] D. J. Erskine, A. J. Taylor, and C. L. Tang, "Femtosecond studies of intraband relaxation in GaAs, AlGaAs, and GaAs/AlGaAs multiple quantum well structures," *Appl. Phys. Lett.*, vol. 45, no. 1, pp. 54–56, 1984.

[212] A. J. Taylor, D. J. Erskine, and C. L. Tang, "Ultrafast relaxation dynamics of photoexcited carriers in GaAs and related compounds," *JOSA B*, vol. 2, no. 4, pp. 663–673, 1985.

[213] L. Rota, P. Lugli, T. Elsaesser, and J. Shah, "Ultrafast thermalization of photoexcited carriers in polar semiconductors," *Phys. Rev. B*, vol. 47, no. 8, p. 4226, 1993.

[214] C. L. Littler and D. G. Seiler, "Temperature dependence of the energy gap of InSb using nonlinear optical techniques," *Appl. Phys. Lett.*, vol. 46, no. 10, pp. 986–988, 1985.

[215] C.-H. Kuo, J.-M. Wu, S.-J. Lin, and W.-C. Chang, "High sensitivity of middle-wavelength infrared photodetectors based on an individual InSb nanowire," *Nanoscale Res. Lett.*, vol. 8, no. 1, p. 327, 2013.

[216] J. A. Alexander-Webber, A. M. R. Baker, P. D. Buckle, T. Ashley, and R. J. Nicholas, "High-current breakdown of the quantum Hall effect and electron heating in InSb/AlInSb," *Phys. Rev. B*, vol. 86, no. 4, p. 045404, 2012.

[217] B. D. McCombe, S. G. Bishop, and R. Kaplan, "Combined resonance and electron g values in InSb," *Phys. Rev. Lett.*, vol. 18, no. 18, p. 748, 1967.

[218] B. D. McCombe, "Infrared studies of combined resonance in n-type InSb," *Phys. Rev.*, vol. 181, no. 3, p. 1206, 1969.

[219] R. C. Enck, A. S. Saleh, and H. Y. Fan, "Phonon cyclotron resonance in the infrared absorption in n-type InSb," *Phys. Rev.*, vol. 182, no. 3, p. 790, 1969.

[220] C.-C. Wu and H. N. Spector, "Effect of nonparabolic band structure on longitudinal magnetoacoustic phenomena," *Phys. Rev. B*, vol. 3, no. 12, p. 3979, 1971.

[221] S. D. Smith, T. S. Moss, and K. W. Taylor, "The energy-dependence of electron mass in indium antimonide determined from measurements of the infrared Faraday effect," *J. Phys. Chem. Solids*, vol. 11, no. 1-2, pp. 131–139, 1959.

[222] E. J. Johnson and D. H. Dickey, "Infrared cyclotron resonance and related experiments in the conduction band of InSb," *Phys. Rev. B*, vol. 1, no. 6, p. 2676, 1970.

[223] J. Kono, A. H. Chin, A. P. Mitchell, T. Takahashi, and H. Akiyama, "Picosecond time-resolved cyclotron resonance in semiconductors," *Appl. Phys. Lett.*, vol. 75, no. 8, pp. 1119–1121, 1999.

[224] G. A. Khodaparast, D. C. Larrabee, J. Kono, D. S. King, S. J. Chung, and M. B. Santos, "Relaxation of quasi-two-dimensional electrons in a quantizing magnetic field probed by time-resolved cyclotron resonance," *Phys. Rev. B*, vol. 67, no. 3, p. 035307, 2003.

[225] Q. Zhang, Y. Wang, W. Gao, Z. Long, J. D. Watson, M. J. Manfra, A. Belyanin, and J. Kono, "Stability of high-density two-dimensional excitons against a Mott

transition in high magnetic fields probed by coherent terahertz spectroscopy," *Phys. Rev. Lett.*, vol. 117, no. 20, p. 207402, 2016.

[226] M. S. Hybertsen and S. G. Louie, "Electron correlation in semiconductors and insulators: band gaps and quasiparticle energies," *Phys. Rev. B*, vol. 34, no. 8, p. 5390, 1986.

[227] M. Failla, M. Myronov, C. Morrison, D. R. Leadley, and J. Lloyd-Hughes, "Narrow heavy-hole cyclotron resonances split by the cubic Rashba spin-orbit interaction in strained germanium quantum wells," *Phys. Rev. B*, vol. 92, no. 4, p. 045303, 2015.

[228] M. Failla, J. Keller, G. Scalari, C. Maissen, J. Faist, C. Reichl, W. Wegscheider, O. J. Newell, D. Leadley, M. Myronov, *et al.*, "Terahertz quantum Hall effect for spin-split heavy-hole gases in strained Ge quantum wells," *New J. Phys.*, vol. 18, no. 11, p. 113036, 2016.

[229] J. Keller, G. Scalari, F. Appugliese, S. Rajabali, M. Beck, J. Haase, C. A. Lehner, W. Wegscheider, M. Failla, M. Myronov, *et al.*, "Landau polaritons in highly nonparabolic two-dimensional gases in the ultrastrong coupling regime," *Phys. Rev. B*, vol. 101, no. 7, p. 075301, 2020.

[230] K. Ersching, C. E. M. Campos, J. C. de Lima, and T. A. Grandi, "Structural and thermal studies of mechanical alloyed InSb nanocrystals," *Mater. Chem. Phys.*, vol. 112, no. 3, pp. 745–748, 2008.

[231] A. Marini, C. Hogan, M. Grüning, and D. Varsano, "Yambo: an ab initio tool for excited state calculations," *Comput. Phys. Commun.*, vol. 180, no. 8, pp. 1392–1403, 2009.

[232] J. P. Perdew, K. Burke, and M. Ernzerhof, "Generalized gradient approximation made simple," *Phys. Rev. Lett.*, vol. 77, no. 18, p. 3865, 1996.

[233] D. R. Hamann, "Optimized norm-conserving Vanderbilt pseudopotentials," *Phys. Rev. B*, vol. 88, no. 8, p. 085117, 2013.

[234] B. D. Malone and M. L. Cohen, "Quasiparticle semiconductor band structures including spin–orbit interactions," *J. Phys. Condens. Matter*, vol. 25, no. 10, p. 105503, 2013.

[235] N. Marzari and D. Vanderbilt, "Maximally localized generalized Wannier functions for composite energy bands," *Phys. Rev. B*, vol. 56, no. 20, p. 12847, 1997.

[236] I. Souza, N. Marzari, and D. Vanderbilt, "Maximally localized Wannier functions for entangled energy bands," *Phys. Rev. B*, vol. 65, no. 3, p. 035109, 2001.

[237] J. R. Yates, X. Wang, D. Vanderbilt, and I. Souza, "Spectral and Fermi surface properties from Wannier interpolation," *Phys. Rev. B*, vol. 75, no. 19, p. 195121, 2007.

[238] A. A. Mostofi, J. R. Yates, Y.-S. Lee, I. Souza, D. Vanderbilt, and N. Marzari, "wannier90: a tool for obtaining maximally-localised Wannier functions," *Comput. Phys. Commun.*, vol. 178, no. 9, pp. 685–699, 2008.

[239] S. A. Bretschneider, I. Ivanov, H. I. Wang, K. Miyata, X. Zhu, and M. Bonn, "Quantifying polaron formation and charge carrier cooling in lead-iodide perovskites," *Adv. Mater.*, vol. 30, no. 29, p. 1707312, 2018.

[240] E. D. Palik, S. Teitler, and R. F. Wallis, "Free carrier cyclotron resonance, Faraday rotation, and Voigt double refraction in compound semiconductors," *J. Appl. Phys.*, vol. 32, no. 10, pp. 2132–2136, 1961.

[241] J. Lloyd-Hughes, "Generalized conductivity model for polar semiconductors at terahertz frequencies," *Appl. Phys. Lett.*, vol. 100, no. 12, p. 122103, 2012.

[242] M. Monti, S. X. Tao, M. Staniforth, A. Crocker, E. Griffin, A. Wijesekara, R. A. Hatton, and J. Lloyd-Hughes, "Efficient intraband hot carrier relaxation in the perovskite semiconductor $cs_{1-x}\mathrm{rb}_x\mathrm{sni}_3$ mediated by strong electron–phonon coupling," *J. Phys. Chem. C*, vol. 122, no. 36, pp. 20669–20675, 2018.

[243] L. Hedin, "New method for calculating the one-particle Green's function with application to the electron-gas problem," *Phys. Rev.*, vol. 139, no. 3A, p. A796, 1965.

[244] P. Hohenberg and W. Kohn, "Inhomogeneous electron gas," *Phys. Rev.*, vol. 136, p. B864, 1964.

[245] J. Heyd, G. E. Scuseria, and M. Ernzerhof, "Hybrid functionals based on a screened Coulomb potential," *J. Chem. Phys.*, vol. 118, no. 18, pp. 8207–8215, 2003.

[246] Y.-S. Kim, K. Hummer, and G. Kresse, "Accurate band structures and effective masses for InP, InAs, and InSb using hybrid functionals," *Phys. Rev. B*, vol. 80, no. 3, p. 035203, 2009.

[247] J. M. Ziman, *Electrons and phonons: the theory of transport phenomena in solids*. Oxford University Press, 2001.

[248] D. E. Aspnes and A. Studna, "Dielectric functions and optical parameters of Si, Ge, GaP, GaAs, GaSb, InP, InAs, and InSb from 1.5 to 6.0 eV," *Phys. Rev. B*, vol. 27, no. 2, p. 985, 1983.

[249] J. Lloyd-Hughes, "Terahertz spectroscopy of quantum 2D electron systems," *J. Phys. D: Appl. Phys.*, vol. 47, no. 37, p. 374006, 2014.

[250] P. Gu, M. Tani, S. Kono, K. Sakai, and X.-C. Zhang, "Study of terahertz radiation from InAs and InSb," *J. Appl. Phys.*, vol. 91, no. 9, pp. 5533–5537, 2002.